# Microstructure and Micromechanics of the Sea Urchin, *Colobocentrotus atratus*

by

Ting-Ting Chen

B.S. Mechanical Engineering and Material Science Engineering
University of California – Berkeley, 2009

SUBMITTED TO THE DEPARTMENT OF MECHANICAL ENGINEERING IN PARTIAL FULFILLMENT OF THE REQUIREMENTS FOR THE DEGREE OF

MASTER OF SCIENCE IN MECHANICAL ENGINEERING
AT THE
MASSACHSETTS INSTITUTE OF TECHNOLOGY

June 2011



Signature of Author: ……
Department of Mechanical Engineering
May 20, 2011

Certified by: .....
Mary C. Boyce
Gail E. Kendall Professor of Mechanical Engineering
Thesis Supervisor

Certified by: .....
Christine Ortiz
Professor of Material Science Engineering
Thesis Supervisor

Accepted by: .....
David Hardt
Chairman, Department Committee on Graduate Students

# Microstructure and Micromechanics of the Sea Urchin, *Colobocentrotus atratus*

by

Ting-Ting Chen

Submitted to the Department of Mechanical Engineering
on May 20, 2011, in partial fulfillment of the
requirements for the degree of
Master of Science in Mechanical Engineering

## Abstract

The purpose of this research is to study the porous microstructure and the micromechanics of the exoskeletal armor of the helmet urchin, *Colobocentrotus atratus.* Its unusual reduction in spines forms a smooth tiling of millimeter-sized, flattened polygonal protective aboral spines. Each aboral spine articulates with the underlying test via a ball-and-socket joint and the microstructure of each aboral spine is a porous network of single-crystal magnesium-doped calcite with a few percent of intercalated organic. Methods of microstructural characterization and simulation were developed through the investigation of the urchin's microstructure and the finite element model. With the high resolution scans from X-ray microcomputed tomography at the Advanced Photon Source at Argonne National Laboratory, Beamline 2BM, visualization and characterization of a complex porous network in three-dimensions was possible, providing a more quantitative insight into the geometry of the microstructure not characterized before in urchin biology literature. The galleried stereom of the individual spines were found to possess a gradient in volume fraction with distance from the socket ranging from 90% at the ball-and-socket joint to 50% at the outer surface. The axial direction of the galleried structure radiates outwardly from the socket and terminated perpendicular to the outer surface of the aboral spine.

Additionally, with the microcomputed tomography results, an efficient and more accurate finite element model of an entire aboral spine along with the microstructural properties was created. The galleried mesh (average pore size ~ 15 microns) was modeled using three-dimensional elastic finite element analysis that consisted of a microstructurally-based parametric representative volume element with periodic boundary conditions. Various loading configurations were simulated to obtain anisotropic stiffness tensors and resulted in an orthotropic effective mechanical behavior with the stiffness in the plane transverse to the long axis of the galleried microstructure (E1, E2) approximately half the stiffness in the axial direction (E3). With parametric simulations, E3 was found to decrease linearly from 0.87 of the solid elastic modulus ($E_s$) to 0.34 of $E_s$ as the volume fraction decreases from 0.88 to 0.46. In the transverse direction, E1 and E2 also decrease linearly from 0.49 of $E_s$ to 0.18 of $E_s$ within the same range of volume fraction. Spatial gradients in density were also modeled, corresponding to the gradient in porosity in the aboral spine. From simulation of blunt indentation by both a conical indenter and flat plate indenter, the graded porosity of the

microstructure exhibits an expected lower overall stiffness and lower stress state than the solid material, but also serves to increase the strains near the exterior surface of the aboral spine while reducing the strains near the joint. This open-pore structure and trabeculae alignment results in a directional strengthening due to inhomogeneous deformations in the porous structure and provides resistance against blunt impacts and containment of penetration into the surface of the aboral spine.

Thesis Supervisor: Mary Boyce
Title: Gail E. Kendall Professor of Mechanical Engineering

Thesis Supervisor: Christine Ortiz
Title: Professor of Material Science Engineering

# Acknowledgements

I would like to first thank both, Prof. Mary Boyce and Prof. Christine Ortiz, of which I am fortunate to have as my co-advisors and mentors at MIT. With their abundance of enthusiasm, thoughts and input, I could not help but be excited as well about the work I am doing and the possibilities it will lead me to.

Thanks to Dr. Ara Nazarian for his help at Beth Israel Deaconess Medical Center (BIDMC) Orthopedics Biomechanics Lab and the research scientists at 2BM at the APS Argonne National Laboratory: Dr. Francesco De Carlo and Dr. Xianghui Xiao, for their guidance and support. And to William DiNatale at the MIT ISN facilities and the staff at the CMSE facilities in building 13 for their patience and teaching.

I would also like to thank all the members from the Ortiz lab and the Boyce lab who have helped me get started as a graduate student working in a lab, are my companions during my time here and are always willing to lend me their kind suggestions and support.

Lastly, I would like to thank my dear friends and family for their unwavering support and limitless encouragement.

This work has been funded by National NSSEFF (N00244-09-1-0064) and supported by the National Science Foundation Graduate Research Fellowship.

# Table of Contents

# List of Tables and Figures

## Tables



## Figures

Fig. 5-6 Comparing the Mises stress distribution of isotropic solid aboral spine under flat plate loading to a depth 0.1mm with the Mises stress distribution of several cases of anisotropic aboral spines, with material orientation specified, under flat plate loading to a depth 0.1mm. (a) isotropic solid calcite, (b) anisotropic low uniform porosity 10% (c) anisotropic average uniform porosity 30% (d) anisotropic high uniform porosity 50% (e) anisotropic graded porosity 10% to 50% (f) anisotropic graded porosity interpolated RVEs.

Fig. 5-7 Comparing specifically the axial stress, $\sigma_{3'3'}$, distribution of isotropic solid aboral spine under flat plate loading to a depth 0.1mm with the axial stress distribution of several cases of anisotropic aboral spines, with material orientation specified, under flat plate loading to a depth 0.1mm. Labels **a-f** refers to the same loading cases as Figure 5-6.

Fig. 5-8 The shear stress, $\sigma_{1'3'}$, distribution of isotropic solid aboral spine under flat plate loading to a depth 0.1mm with the shear stress distribution of several cases of anisotropic aboral spines, with material orientation specified, under flat plate loading to a depth 0.1mm. Labels **a-f** refers to the same loading cases as Figure 5-6.

Fig. 5-9 Comparing the maximum principal strain distribution of isotropic solid aboral spine under flat plate loading to a depth 0.1mm with the maximum principal strain distribution of several cases of anisotropic aboral spines, with material orientation specified, under flat plate loading to a depth 0.1mm. Labels **a-f** refers to the same loading cases as Figure 5-6.

Fig. 5-10 The axial strain, $\varepsilon_{3'3'}$, distribution of isotropic solid aboral spine under flat plate loading to a depth 0.1mm with the axial strain distribution of several cases of anisotropic aboral spines, with material orientation specified, under flat plate loading to a depth 0.1mm. Labels **a-f** refers to the same loading cases as Figure 5-6.

Fig. 5-11 Comparing the shear strain, $\varepsilon_{1'3'}$, distribution of isotropic solid aboral spine under flat plate loading to a depth 0.1mm with the shear strain distribution of several cases of anisotropic aboral spines, with material orientation specified, under flat plate loading to a depth 0.1mm. Labels **a-f** refers to the same loading cases as Figure 5-6.

Fig. 5-12 Force-Depth curves for indentation with a rigid conical indenter on the same set of material gradients as Figure 5-5. Similar to the flat plate case, the two vertical lines indicate the equivalent depth of indentation for each case, a* (for the isotropic solid calcite case) and b* (for the anisotropic lowest uniform porosity case), where the energy absorbed is the same as the energy absorbed in the anisotropic interpolated gradient case at the final depth of indentation, 0.096 mm. The indentation depth at a* is 0.068 mm and at b* is 0.084 mm.

Fig. 5-13 Comparing the Mises stress distribution of isotropic solid aboral spine under conical indenter loading to a depth 0.1mm with the Mises stress distribution of several cases of anisotropic aboral spines, with material orientation specified, under conical indenter loading to a depth 0.1mm. Similar to Figure 5-6, (a) isotropic solid calcite, (b) anisotropic low uniform porosity 10% (c) anisotropic average uniform porosity 30% (d) anisotropic high uniform porosity 50% (e) anisotropic graded porosity 10% to 50% (f) anisotropic graded porosity interpolated RVEs.

Fig. 5-14 Comparing specifically the axial stress, $\sigma_{3'3'}$, distribution of isotropic solid aboral spine under conical indenter loading to a depth 0.1mm with the axial stress distribution of several cases of anisotropic aboral spines, with material orientation specified, under conical indenter loading to a depth 0.1mm. Labels **a-f** refers to the same loading cases as Figure 5-13.

Fig. 5-15 The shear stress, $\sigma_{1'3'}$, distribution of isotropic solid aboral spine under conical indenter loading to a depth 0.1mm with the shear stress distribution of several cases of anisotropic aboral spines, with material orientation specified, under conical indenter loading to a depth 0.1mm. Labels **a-f** refers to the same loading cases as Figure 5-13.

Fig. 5-16 Comparing the maximum principal strain distribution of isotropic solid aboral spine under conical indenter loading to a depth 0.1mm with the maximum principal strain distribution of several cases of anisotropic aboral spines, with material orientation specified, under conical indenter loading to a depth 0.1mm. Labels **a-f** refers to the same loading cases as Figure 5-9.

Fig. 5-17 The axial strain, $\varepsilon_{3'3'}$, distribution of isotropic solid aboral spine under conical indenter loading to a depth 0.1mm with the axial strain distribution of several cases of anisotropic aboral spines, with material orientation specified, under conical indenter loading to a depth 0.1mm. Labels **a-f** refers to the same loading cases as Figure 5-13.

Fig. 5-18 Comparing the shear strain, $\varepsilon_{1'3'}$, distribution of isotropic solid aboral spine under conical indenter loading to a depth 0.1mm with the shear strain distribution of several cases of anisotropic aboral spines, with material orientation specified, under conical indenter loading to a depth 0.1mm. Labels **a-f** refers to the same loading cases as Figure 5-13.

Fig. 5-19 Mises and maximum principal strain contours of isotropic solid calcite case (**a** and **c**) compared to the anisotropic graded porosity case (**b** and **d**). Plots **a** and **c** are at an indentation depth of 0.13 mm while plots **b** and **d** are at a depth of 0.18 mm, with the same energy of 8.228e-6 J absorbed by the aboral spine.

# Table of Symbols and Abbreviations

| | |
|---|---|
| SEM | Scanning Electron Microscope |
| APS | Advanced Proton Source, at Argonne National Laboratory |
| ASR | Axial strut radius of the microstructural repeating unit |
| TSR | Transversal strut radius of the microstructural repeating unit |
| TSL | Transversal strut half-length (2 x TSL is the transversal strut length) of microstructural repeating unit |
| ASL | Axial strut length of microstructural repeating unit |
| FR | Fillet radius of repeating representative volume |
| microCT | Micro-computed tomography |
| RVE | Representative volume element |
| $R_1$ | Radius of axial strut in the representative volume element |
| $R_2$ | Radius of the six transversal struts in the representative volume element |
| $L_1$ | Axial strut length of the representative volume element |
| $L_2$ | Transversal strut length of the representative volume element |
| TSVS | Transversal strut vertical spacing |
| AA1, AA2, BB1, BB2, CC1, CC2, ZZ1, ZZ2 | Labels of the RVE boundary node sets used in implementing the periodic boundary conditions. |
| $\mathbf{u}$ | Displacement vector |
| $\mathbf{H}$ | Macroscopic displacement gradient |
| $\mathbf{X}$ | Reference position vector |
| $\mathbf{F}$ | Macroscopic deformation gradient |
| $\frac{\partial \boldsymbol{u}}{\partial \boldsymbol{X}}$ | Derivative of the displacement vector with respect to the reference position vector |
| N1, N2, N3 | Three virtual nodes used in the macroscopic displacement gradient |

| | |
|---|---|
| $\mathbf{S}$ | First Piola-Kirchhoff stress tensor |
| $\Xi_1, \Xi_2, \Xi_3$ | Generalized reaction forces |
| $V_o$ | Original volume of the representative volume element |
| $\mathbf{T}$ | Macroscopic Cauchy stress tensor |
| $\varepsilon^*$ | Strain |
| $\gamma$ | Shear strain |
| $\nu$ | Poisson's ratio |
| E | Young's modulus |
| G | Shear modulus |

# CHAPTER 1 Introduction

Among engineering materials, ceramics are often included for their high strength, low weight, and low conductivity. Yet, they are greatly limited by their brittle nature. To counteract this limitation, engineering of ceramic materials focus on the design of material components of the ceramic as well as the microstructure to increase its energy absorption and fracture toughness. Recent advances in multilayered composites as well as lightweight synthetic materials have vastly improved the quality of armor such as the small arms protective insert (SAPI) in military armor to protect against higher velocity rifle rounds and higher caliber ballistics. With insight from biological armor, where nature has only a limited access to resources and yet can still allow for effective protective designs, protection mechanisms can continue to evolve. Among protection systems, there is a wide mixture of mechanisms, both in nature and man-made systems, designed to absorb or deflect the specified impact and avoid catastrophic damage of the object to be protected. The strength and resilience stems from the nanoscale such as inherent material properties and crystallinity, to microscale layering or organization to the overall macroscale design and mechanisms such as macroscopic geometry or passive and dynamic mechanisms. In each component, there is a need to optimize for a variety of parameters such as energy absorption, weight, resource costs, flexibility, and coverage to create the specific type of resistance the protection system offers.

From the turbulent water environment and constant predatory attacks, the urchin *Colobocentrotus atratus*, has evolved separately from common spiny urchins to adapting unique flattened spines composed of single crystal magnesium-doped calcite covering its outer exoskeleton, also composed of the same material. In addition, the spines of the sea urchin are

attached to the body by a ball and socket joint arrangement with a low energy catch apparatus as both a passive and active control mechanism (Peters 1985). This adaptation essentially creates a second, more flexible barrier against harm. Prior research on other urchins and their spines has focused on the crystallinity, the catch apparatus, and the qualitative variation in microstructure (Weber 1971, Politi 2004, Presser 2009, Takemae 2005). What is missing is a quantitative characterization of the applicable mechanics of the material as a function of the microstructural variation. From the initial characterization, the porosity, magnesium content and morphological structure of the urchin's test plate was found to vary along the axis of the plate possibly because of different functions of the outer plate surface and the inner articulation surface of the spine's attachment to the body. The microstructure near the outer surface of the aboral spine is oriented to resist impact perpendicular to the plate surface while the articulation at the opposite side of the spine requires a smooth surface with porosity possibly to provide fluid flow as a lubricant to the ball and socket joint.

Because of the *C. atratus*'s distinctively spineless, single crystal calcite exoskeleton, its lightweight yet protective strength has the potential to inspire novel fabrication techniques for armor design by combining both the micro and macrostructural advantages of the shell's porous design with the resilience of modern materials. This research attempts to determine if the anisotropic and graded porous microstructural details of the urchin's exoskeleton has any relevance to the functionality of the flattened spines and how the organizational gradient in the microstructural geometry of the spine contributes to the stiffness and mechanical behavior of the spine.

# CHAPTER 2 Background

The species *Colobocentrotus atratus*, or helmet urchin, belongs in the class *Echinoidea*, which contain globular sea urchins or “regular” echinoids and “irregular” echinoids (Agassiz 1908). The class is characterized by a five-fold symmetry (pentamerism), spines radiating from the center of the body and hundreds of adhesive “tube feet” for movement and adhesion to rocks (Figure 2-3). Among the different species of urchins, there is a range in the color, sharpness of the spine tip, and thickness of the cross-sectional area of the spines. While on most urchins, the spines are long and often sharp to protect the urchin from predators and competitors, the aboral spines of the *C. atratus* have been reduced in size and flattened to tile the entire dome of the urchin’s aboral surface, creating an unusual, smooth layer on the body (Figure 2-1). This particular species has been found in the Indo-Pacific islands in the world: Zanzibar, Natal, Madagascar, Mauritius, the Seychelles, Christmas Island, Java, Timor, Amboina, and the Hawaiian Islands (Clark AH 1954). Only two other extant species of urchins (within the same genus, *Colobocentrotus*), *C. pedifer* found in Tuamotus and *C. mertensi* found in Bomin and Mariana, also exhibit a similar flattened, reduced aboral spines adaptation (Agassiz 1908).

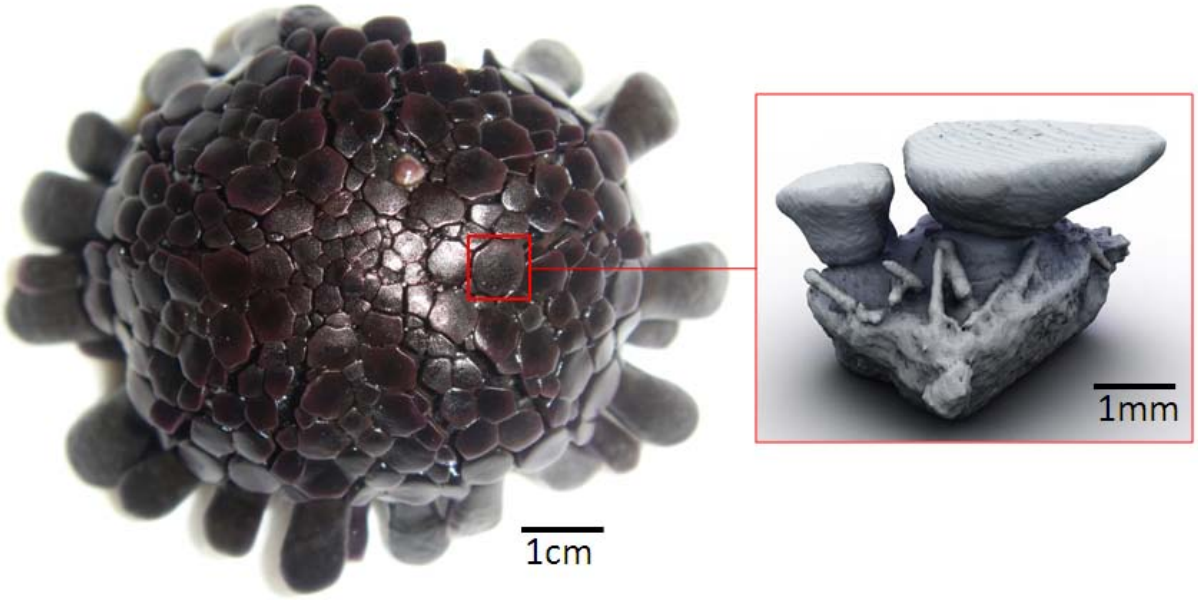


Figure 2-1: A top view of the sea urchin, *Colobocentrotus atratus.* The inset on the urchin shows a rendering of the aboral spine attached to the test plate.

Why are the spines of the *C. atratus* so different? The common explanation cites the species' specific habitat. Typically, while most sea urchins are found in the intertidal regions of the sea coasts, the *C. atratus* are more specifically located in the infralittoral zone, characterized by a rocky terrain and high energy surfs of powerful waves (D.B. James 1982). In comparison with other sea urchins and even with similar species (*C. pedifer* and *C. mertensi*), *C. atratus* exhibits a refined dome-shaped test and the highest attachment strength of their tube feet (Philippi 1996, Santos 2008). If detached, the creature may be subject to waves crushing them against the rocky shore and predators. Their adaptation to lock onto the substrate and survive in the turbulent zone of the intertidal region is attributed to the attachment strength of their tube feet as well as the geometric morphology of its body (Santos 2008, Mortenson 1943). The flattened aboral spines have been suggested to contribute to reducing the drag of the urchin's body to resist the energy of the clashing waves (Denny and Gaylord 1996, Gaylord 2000). As the

outermost protective surface of the urchin, the flat aboral spines must resist wave-induced hydrodynamic forces in addition to mechanical loads such as blunt impact against rocks as well as sharp or crushing predator attacks and from particles or rocks.

## 2.1 Anatomy of the Colobocentrotus atratus

Similar to other urchins, the test of the *C. atratus* is the exoskeletal boundary layer composed of collagen reinforced, joined or sutured magnesium calcite plates or ossicles, which encloses an urchin's internal organs, shown in Figure 2-5 (Ellers 1998, Telford 1985). It is composed of five ambulacral regions separated by five interambulacral zones (Figure 2-2), (Agassiz 1908). On each test plate, spines articulate freely on raised bumps called tubercles, controlled by collagenous fibers (Figures 2-5 and 2-6). From an urchin attachment strength study, the average *C. atratus* diameter is 34.8 ± 5.4 mm and height is 14.0 ± 1.9 mm of 30 urchins (Santos 2008). The microstructural composition of the test and spines are termed the stereom of the exoskeletal components. Among urchins, the stereom of the aboral interambulacral test of the *C. atratus* has a relatively large thickness, density and multiple layers of different porous microstructure (Smith 1980). The upper half of the urchin is the aboral surface, which includes the aboral spines and anus while the lower half is referred to as the oral surface and contains the mouth (Aristotle's Lantern) and tube feet (Figures 2-2, 2-3, and 2-4). Surrounding the adoral part of the test is a basal skirt of flattened spines.

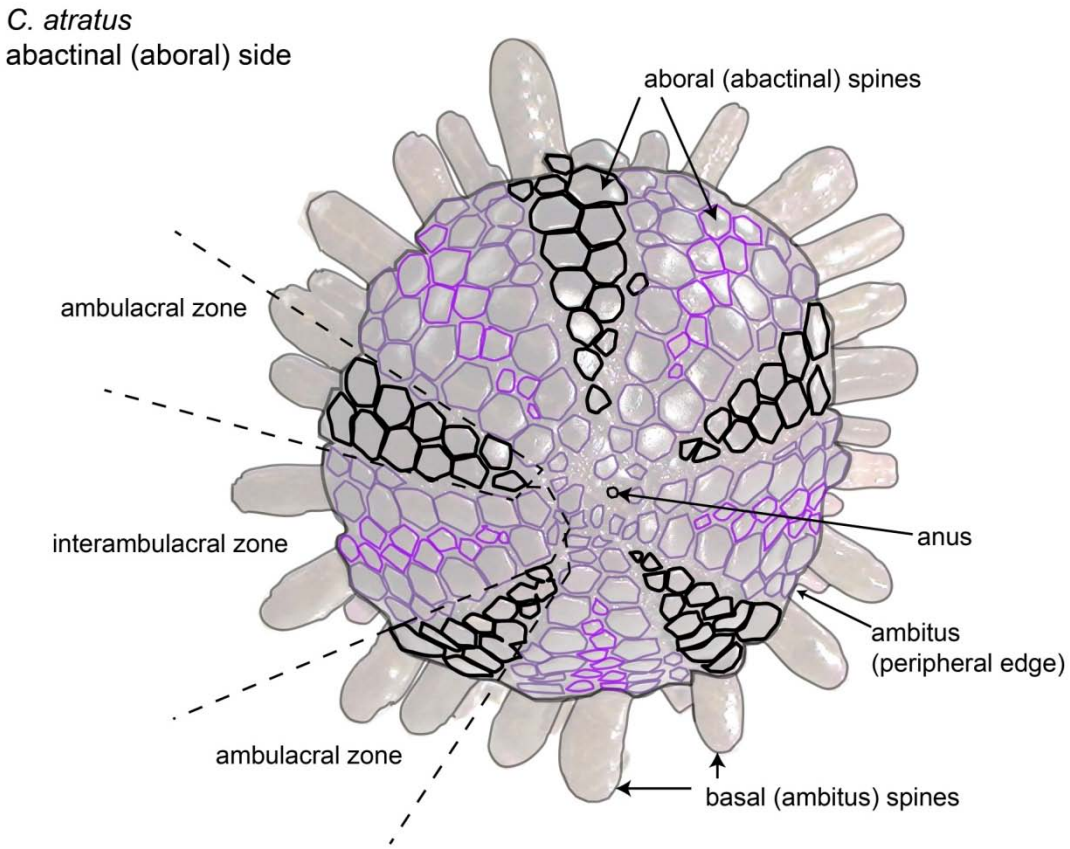


Figure 2-2: Schematic of the abactinal side of *C. atratus*. The boundary between two of the five ambulacral zones and one of the five interambulacral zones are indicated with dashed lines.

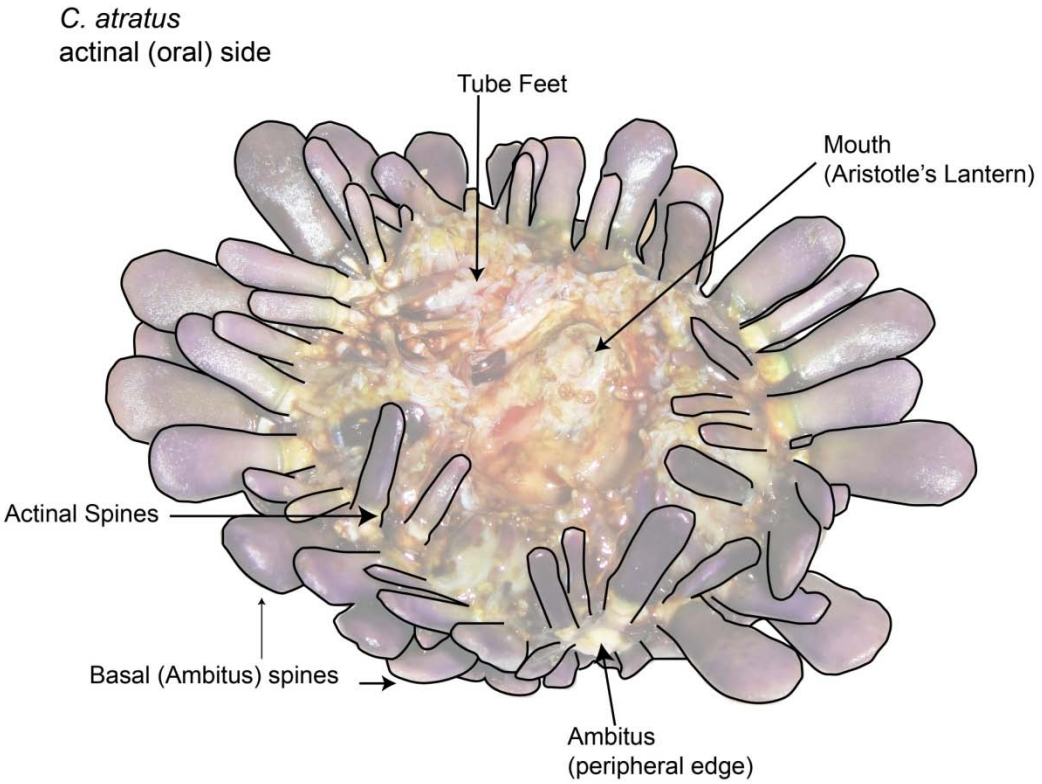


Figure 2-3: Schematic of actinal side of *C. atratus*

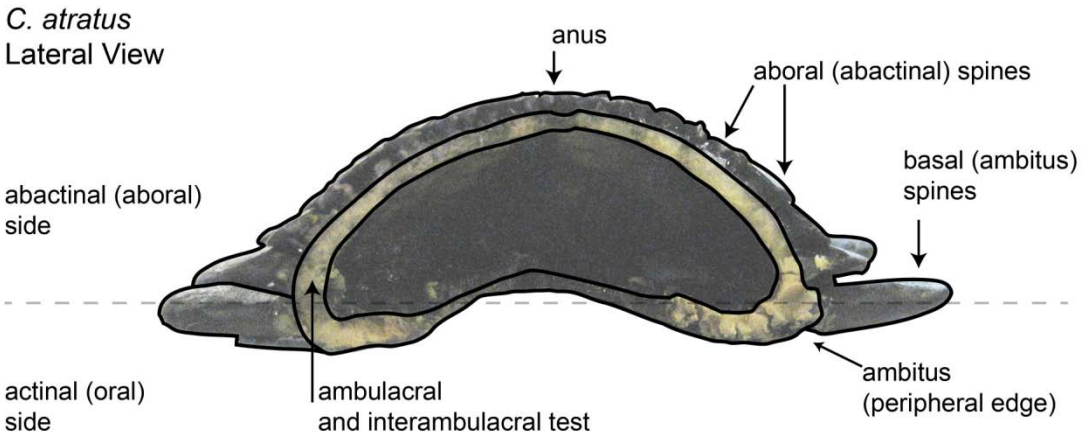


Figure 2-4: Schematic of lateral (side) view of *C. atratus* sectioned in half along the abactinal-actinal axis. The Aristotle's Lantern and surrounding actinal tests are not shown.

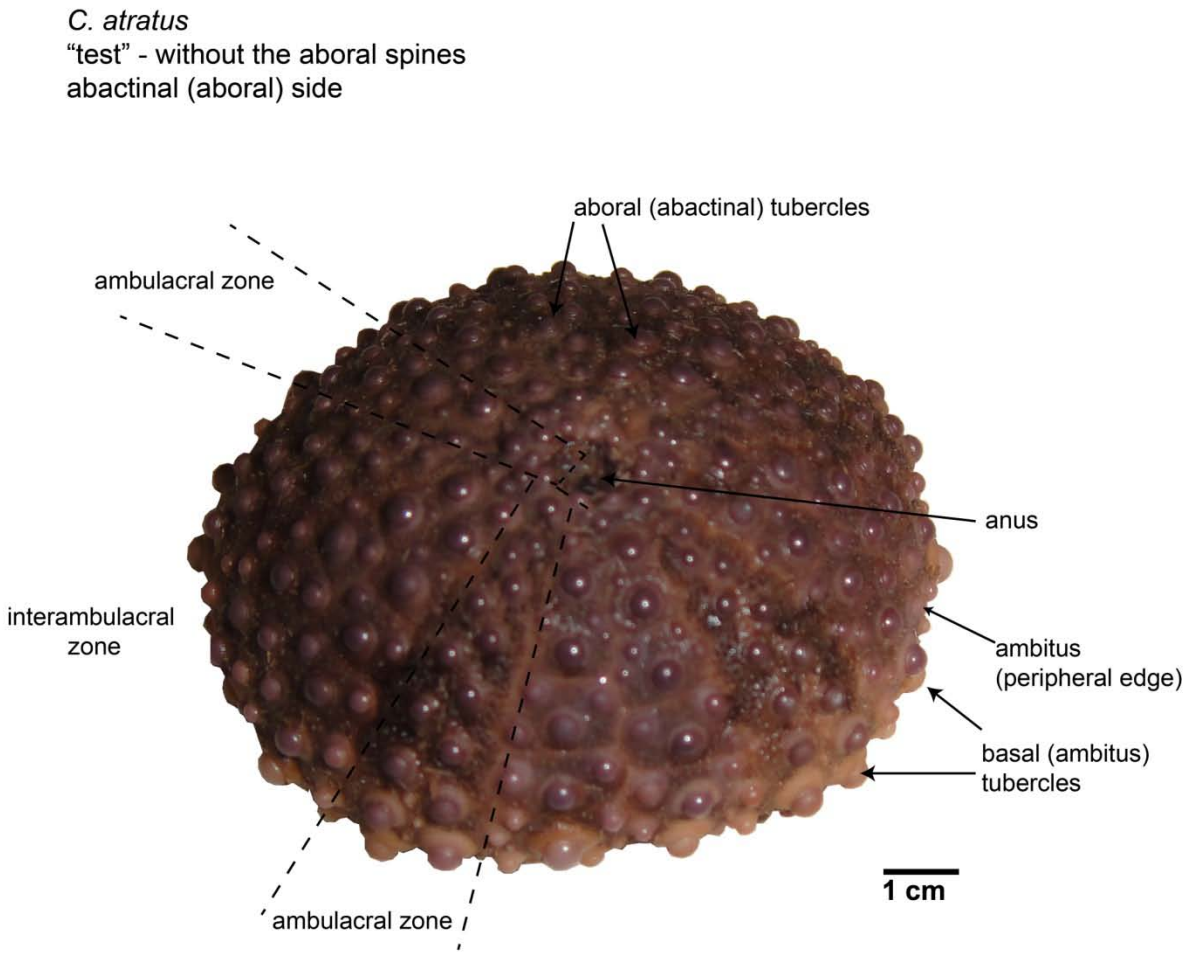


Figure 2-5: Picture of abactinal side of the test of *C. atratus*, with the boundaries between the ambulacral and interambulacral zones indicated by dashed lines. The bumps on the dome surface of the test are the tubercles, the "ball" part of the spine articulation joints. Photograph by Elaine Lee, shown with permission.

Both the test and spines of the *C. atratus* are composed of the same magnesium calcium carbonate material. In this thesis, the aboral spines will refer to the flattened spines that form a smooth cover of the dome of the body (the aboral surface) while the oblong, club-shaped spines that circle the base of the dome, forming a skirt will be referred to as the basal spines (Figure 2-2 and 2-4).

Of the two distinct morphologies of spines, the basal spines are the most motile with a wide range of movement in its articulation and are often used to aid in movement and bracing the urchin in crevices and rocks. Each of the aboral spines is also able to articulate by tilting on individual ball-and-socket joints, controlling the exposure and coverage of the underlying test. The articulating joints allows independent movement of each spine actively directed by a ring of muscle fibers, but is also controlled by a passive "Catch Apparatus," made of bundles of collagenous fibers, that stiffen to temporarily lock and prevent movement of the spines (Wilkie 2005, Takemae 2005).

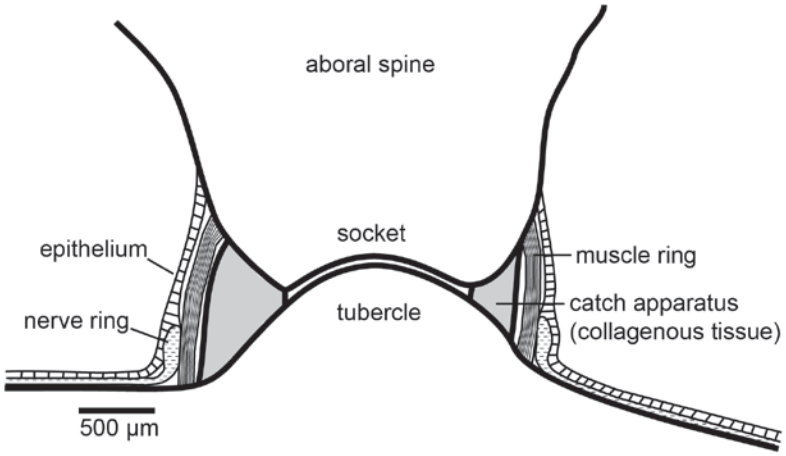


Figure 2-6: Schematic of the articulating ball-and-socket joint of sea urchin spines. (adapted from Peters 1985).

Although the test itself is rigid, as the urchin navigates through the rocks and corals, the movement of the aboral spines possibly provides flexibility of the body of the urchin. Both the aboral and basal spines are composed of a porous microstructure arrangement that can be categorized into several different kinds of oriented microstructural units: galleried, fascicular and labyrinthic microstructure (discussed in detail in chapter 3). While the top surface of the plate remains flat, the morphology of the aboral spines increase in size and are more elongated from

the apex of the dome to the basal spines. The basal spines have the most movement. Their elongated shape allows the urchin to use these spines to push off surfaces to aid moving and anchoring on and between rocks or in crevices.

Besides the anatomical orientation of the *C. atratus*, this thesis will employ a set of three regular Cartesian coordinates in describing the orientation of the components at three different length scales. The urchin's macro dome geometry will be oriented with (X,Y,Z), the urchin's spines (1`, 2`, 3`) and finally the microstructural unit (1,2,3), shown in Figure 2-7.

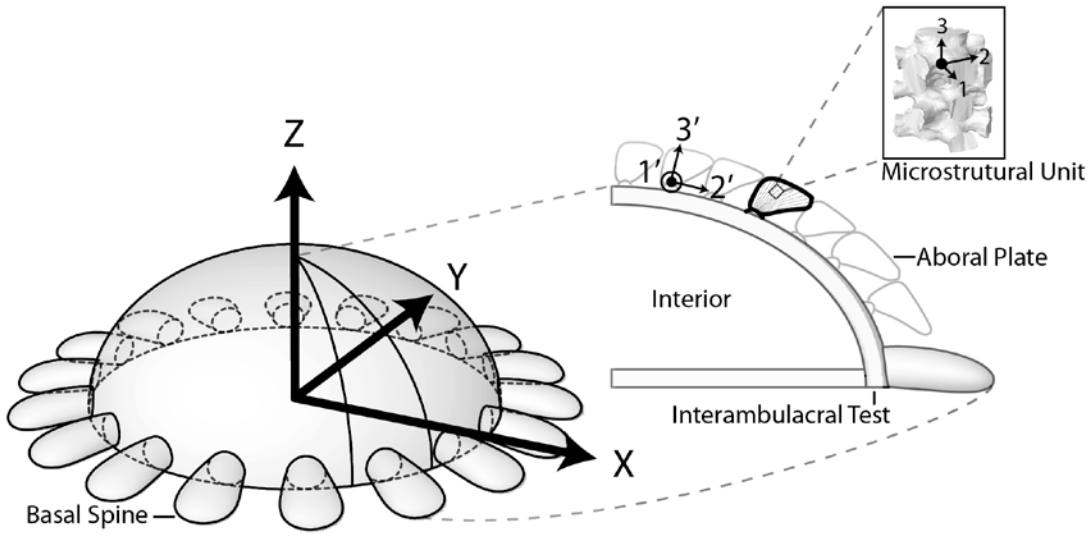


Figure 2-7: Schematic of urchin anatomy with three specified coordinate system: (X,Y,Z) for the overall urchin geometry and (1`,2`,3`) for each plate along the aboral test and (1,2,3) for the orientation microstructural repeating unit within each plate

## 2.2 Inherent material properties

Similar to the underlying test plates, the microstructure of each plate is an open-cell network of porous material, made of magnesium substituted calcite ($CaMgCO_3$) with a small percent of intercalated organic proteins (X. Su 2000, Magdans 2004). Some studies on the crystalline structure have suggested that the sea urchin spines are monocrystalline (Currey 1967, Donnay

1969, Raup 1959, Paquette 1990, Su 2000). Others have suggested a composition of polycrystalline aggregates, combination of both or single crystals with increased mosaicity (O'Neill 1981, Tsipursky 1993, Oaki 2006, Towe 1967, Blake 1984, Berman 1990, Aizenberg 1997). The inhomogeneous magnesium distribution in the spines of urchins has been suggested to strengthen the mechanical properties of the spines, especially in species with long spines, by inhibiting cleavage or catastrophic crack propagation (Magdans 2004). The crystal produces a wide variety of porous morphology, each with a different functional role. Bending, indentation and other mechanical studies on other urchins and calcite in Brachiopods have attempted to establish the inherent material properties of the biogenic magnesium calcite, summarized in Table 2-1. Literature reveals that the modulus of the organic calcite ranges from 30 GPa to around 100 GPa. This large range is due to the different species used, location of the experimental test (such as indentation location and depth), and sample preparation and condition during testing. Most of the values were obtained through nanoindentation of the porous material, so an indentation modulus was obtained.

Table 2-1: Properties of biogenic magnesium calcite found in literature

| Paper | Species | Material | Specimen Preparation | Single Crystal | Hardness | Reported Young's Modulus | Method |
|---|---|---|---|---|---|---|---|
| Perez-Huerta (2007) | Calcite Brachiopods | Calcite semi-nacre | Dry, polished | No | 0.4-3 GPa | 50-85 GPa | nanoindentation |
| Emlet (1982) | *S. Droebachiensis* (green urchin) and *S. Franciscanus* (red urchin) | Calcite in larval spicules | Dry, isolated with 5% sodium hypochlorite and washed | Yes | | 36.3 GPa +/- 2.9 GPa | Cantilever bending, measurement of deflection |
| | *Denraster Excentricus* (sand dollar) | Calcite in fenestrated spicules | Dry, isolated with 5% sodium hypochlorite and washed | Yes | | 48.9 GPa | Cantilever bending, measurement of deflection |
| Ma (2008) | *Paracentrotus Lividus* | Calcite from teeth | Embedded in methyl methacrylate, Dry | No | 5.7 GPa (no cracks) | 98.5 GPa | nanoindentation |
| | | Needles within tooth matrix | Wet | Yes | 3.5 GPa (cracks) | 71.1 GPa | nanoindentation |
| | Synthetic single-crystal calcite | Pure Calcite | | Yes | 2.7 GPa | 73.5 GPa | nanoindentation |
| | Geological Dolomite | | | | 6.5 GPa | 117 GPa | nanoindentation |
| Burkhardt and Markel (1980) | *Diadematid* | Urchin Spines | Dry | Yes | | 69.4 GPa | Bending |
| | | | Wet | Yes | | 52.1 GPa | Bending |
| Presser et. al. 2010 | *Heterocentrotus mammillatus,* | Urchin spines | Dry | Yes | | 40-63 GPa +/- 5 GPa | nanoindentation |
| | *Phyllacanthus imperialis* | | Dry | Yes | | 29-47 GPa +/- 5 GPa | nanoindentation |
| | *Prinocidaris baculosa* | | Dry | Yes | | 48-71 GPa +/- 5 GPa | nanoindentation |

# CHAPTER 3 Microstructural Analysis

In order to develop an understanding of the connections amongst microstructure, properties, and function, accurate characterization of not only the macrostructure, but also the unique features in the microstructure are needed. The focus of the microstructural analysis within this thesis is on the aboral spines, which provide protective armor coverage of the dome-shaped test of the urchin. Due to the small size of the urchin's aboral spines, high resolution scanning electron microscopy, low resolution microcomputed tomography, and high resolution X-ray phase contrast microcomputed tomography were employed in an attempt to reconstruct both the macroscale and microscale features of the aboral spines from the millimeter to micrometer length scales. With both two-dimensional and three-dimensional scans of the aboral spines, quantification of the porous network and other microstructural features can be achieved with high accuracy as well as the reconstruction of the three-dimensional geometries to be imported into a mesh visualization or finite element discretization for analysis within a program such as ABAQUS.

## 3.1 Experimental Methods

*Scanning Electron Microscopy (SEM)*

Initial characterization of the plate microstructure incorporated the use of scanning electron microscopy (SEM) on several aboral spine samples as well as systematic cross-sectional slices of the aboral spines. Live *C. atratus* specimens were obtained from Pisces Pacifica Co. in Honolulu, Hawaii and maintained in saltwater aquariums. The spine samples for imaging and characterization analysis were collected from deceased urchins.

For the micrographs of the external surfaces, aboral spines were collected and simply cleaned, sonicated in distilled water using an *Ultramet* ultrasonic cleaner for 10 seconds and air-dried. Aboral spines were placed on a standard sample holder coated with 10nm of Au-Pd and micrographs were obtained from a JEOL JSM-6060 Scanning Electron Microscope (SEM 6060). During imaging, the sample plane was oriented perpendicular to the electron beam incidence. A 10-20 kV accelerating voltage was applied.

To obtain micrographs of the interior structure of the aboral spines, several spines from a single urchin were collected and sonicated in distilled water for 60 seconds to expel debris from the pore spaces of the microstructure. The aboral spines were left to dry overnight before embedding each in room-temperature curing epoxy (Loctite Fixmaster Poxy-Pak 81120) to facilitate cutting. A day later, the aboral spines embedded in epoxy were sectioned with a diamond-impregnated annular wafering saw (Buehler Isomet 5000) at 800–900 RPM. Two to three 1 mm slices were obtained from the aboral spines to cross-section the plate in the longitudinal and transverse directions (Figure 3-4). The exposed surfaces were then viewed in the SEM under various magnifications. Additional images of a fracture surface of a plate were taken after fracturing the plate with a sharp indenter.

*Microcomputed Tomography (microCT)*

Because the feature size of the pores range from 5 to 20 microns, even at the highest resolution of 6 microns, the conventional micro-CT machines built for medical applications such as the Scanco Medical AG – MicroCT 40 are not quite at the resolution high enough to resolve the smaller pores and struts present in the microstructure. But, the Scanco MicroCT machine can capture features larger than 50 microns quite well using a resolution of the scans of 12 microns

with a field of view of around 30.7 mm. This range in field of view can create a scan of a portion of an urchin as well as a single plate.

Two scans were performed using the Scanco Medical AG – MicroCT 40 at Beth Israel Deconnes Orthopoedic lab in Boston, MA. The first was a test and plate system removed from the exoskeleton of a *C. atratus* using a razor blade. The specimen has a large plate detached from its tubercle as well as a smaller plate attached to the smaller tubercle. The second sample consisted of roughly a quarter of the same *C. atratus's* exoskeleton with aboral spines and basal spines intact. The samples were kept in a freezer until scanning, but no other sample treatments were performed. To prepare the samples for scanning, the test-plate system and the quarter exoskeleton were placed in 12.3 mm diameter and 30.7 mm diameter Kapton tubes in between pieces of foam to hold the sample in place. The test-aboral spine system was scanned at a resolution of 12.0 μm at voltage of 45 kVp, current of 177 μA and with a field of view of 12.3 mm. The larger specimen, the quarter exoskeleton, was scanned with the same voltage and current, but at a lower resolution of 30 μm and field of view 30.7 mm.

Higher spatial resolution scans, but with a limited field of view of the detector, was possible with synchrotron-based microtomography at the Advanced Photon Source (APS) at Argonne National Laboratory. Smaller plate samples, around 1mm in length, were placed in a 2.5 mm diameter Kapton tube mounted vertically on a mound of Boekel tackiwax on the metal sample holder which affixes to the X-ray stage (Figure 3-2). Care was taken to align the sample in the center of the rotation stage, such that the rotational axis was centered and the sample was always in the X-ray's field of view. Wax was inserted in the tube to prevent the sample from shifting during rotation of the sample stage. The scans were performed at a voltage of 15 keV with a 0.12 degree angle interval between scans. The raw images created after a full rotation was

digitally reconstructed to create transversal slices of the sample using ImageJ and a custom script in IDL.

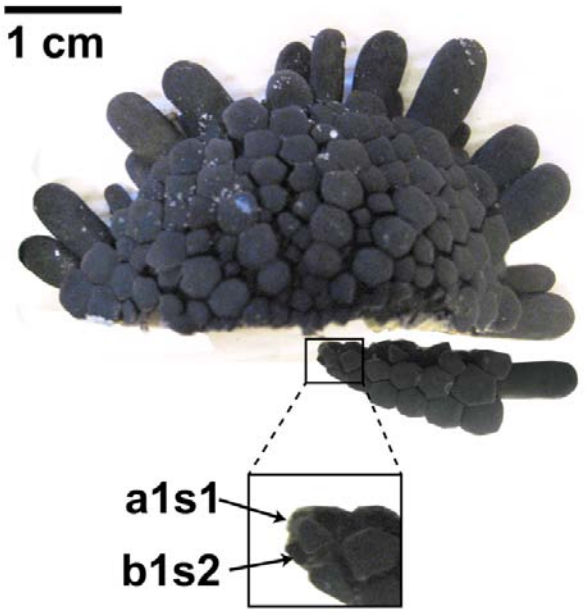


Figure 3-1: Sectioning exoskeletal dome of *C. atratus* to obtain samples "a1s1" and "b1s2", located near the anus, at the apex of the dome.

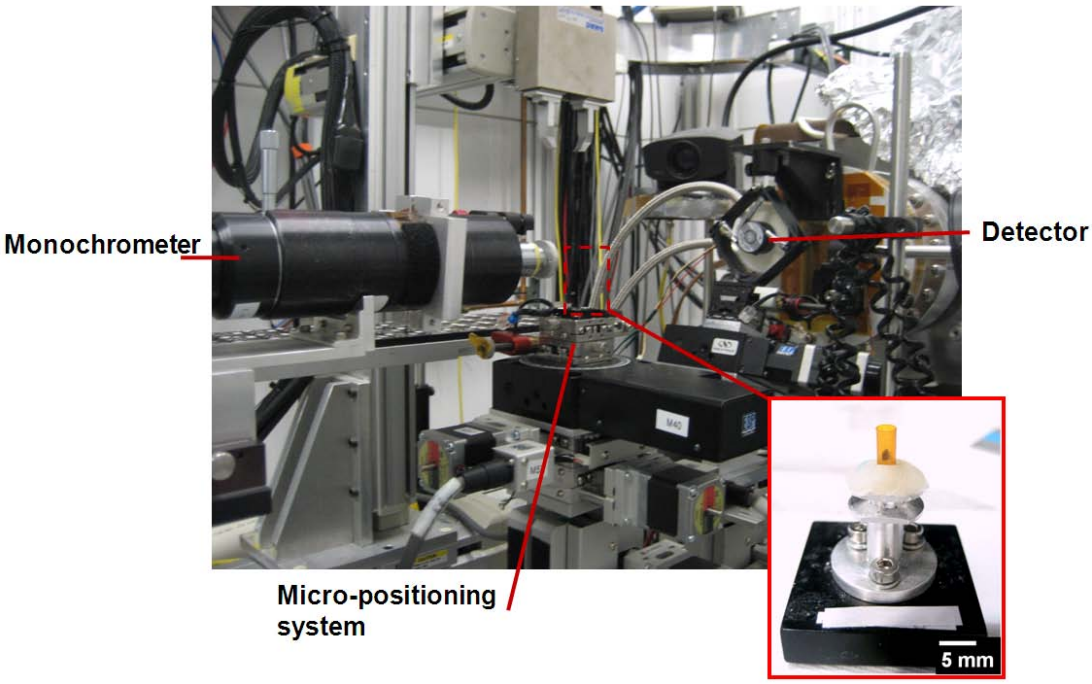


Figure 3-2: X-ray tomography set-up and sample mounting stage at 2BM at the National Argonne Laboratory.

### 3.2 Spatial Two-Dimensional Imaging with SEM

From the SEM micrographs of the top external surface of the plate, there was a clear sign of the periodicity in the microstructure where the long gallery structures are capped with bulbous geometry (Figure 3-3.b). Each protrusion has a connectivity of five or six to neighboring bulbous protrusions. The pores range from 10 to 15 microns in diameter and are approximately circular or elliptical in shape. These pores seem to extend down, perpendicular to the surface, into the aboral spine (seen more clearly in the cross-sectional images, Figure 3-4). Beginning at the edge of the top surface to the edge of the socket region, long ridges, 10-15 microns thick and 5-15 microns apart, run along the external sides of the plate to create a textured external surface bounding the sides of the aboral spines (Figure 3-3.c). The socket in Figure 3.3.d is a surprisingly smooth, curved surface with micro-pores only several microns in diameter, organized in a similar pentagonal and hexagonal pattern as the top exterior surface in Figure 3.3.b.

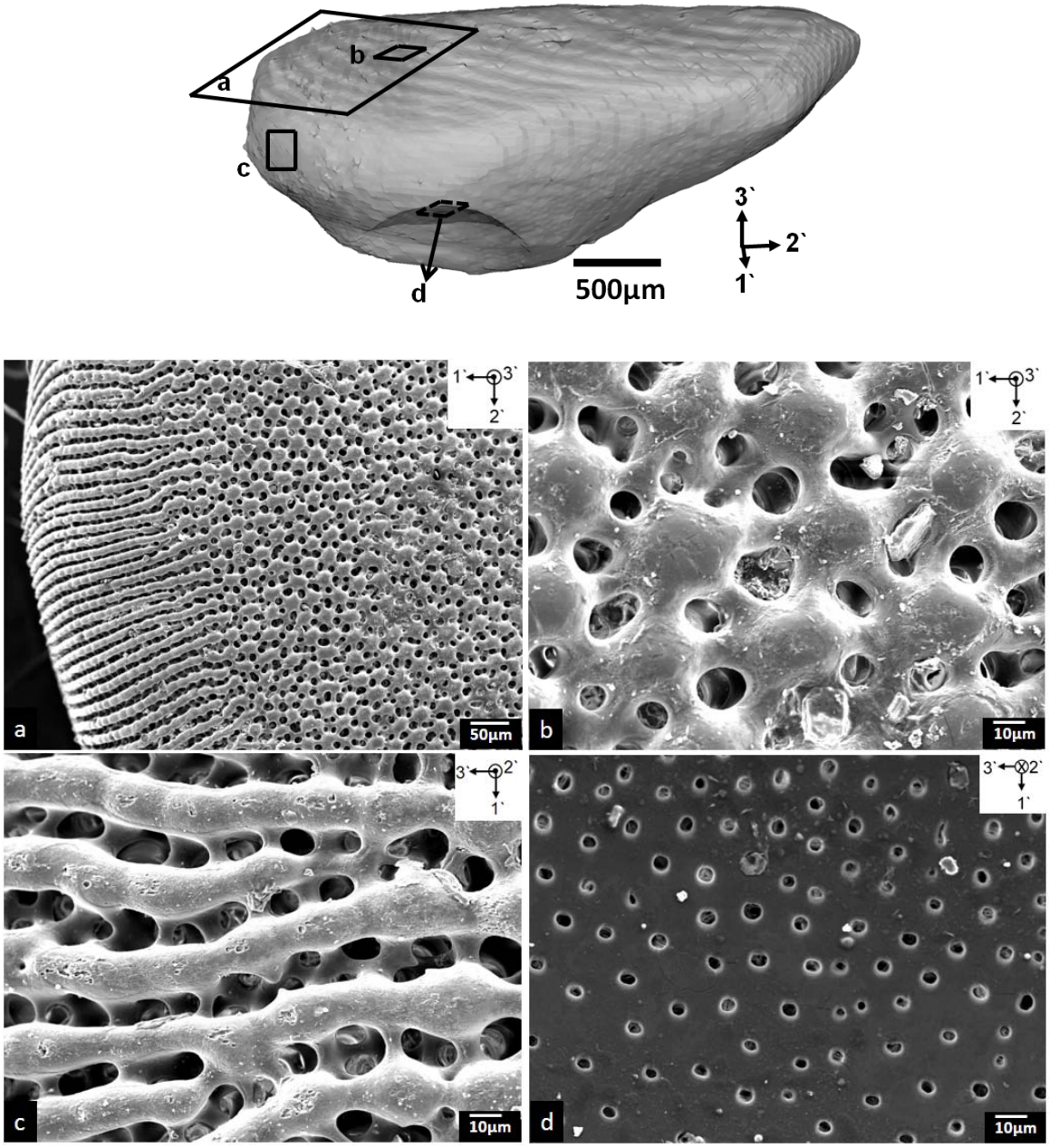


Figure 3-3: SEM micrographs of aboral spine external surfaces with schematic of aboral spine showing a rough location of scan. (**a-b**) Top surface of aboral spine. (**c**) Ridges along sides of aboral spines. (**d**) Surface of aboral spine socket. (SEM micrographs by Elaine Lee, shown with permission)

The cross sectional images in Figure 3-4 and Figure 3-5 shows, more clearly, an open-porous microstructural network with long galleries of struts that run radially along the longitudinal direction of the aboral spine. The galleries seem to stem from the socket region of the spine and radially branch out until it reached the external surface of the spine, creating a radial pattern of the microstructure (Figure 3-4.e). From the cross-sectional micrographs, pore dimensions and spacing were measured and summarized in Table 3-1. Thick bands, or discontinuities in the radial lines indicate growth rings, as described by Su, are visible in both the longitudinal and transversal cross-sectional micrographs of Figure 3-4 and orthogonal to the radial lines formed by the continuous galleries (X. Su 2000). Closer observation of the microstructure reveals transversal struts which connect the axial galleries in either a hexagonal or rectilinear connection. Overall, the microstructure is an open-porous network of the magnesium calcite, organized perpendicular to the direction of spine growth.

Table 3-1: Measured values from the SEM micrographs of plate cross-sections

| | Axial Pore Diameter (μm) | Axial Strut Diameter (μm) | Lateral Pore Center to Center Distance (μm) | Lateral Pore Diameter (μm) |
|---|---|---|---|---|
| Minimum | 9.5 | 50 | 22.7 | 9.1 |
| Average | 16.7 | 59.1 | 28.4 | 16.3 |
| Maximum | 28.6 | 76.2 | 37.9 | 28.8 |

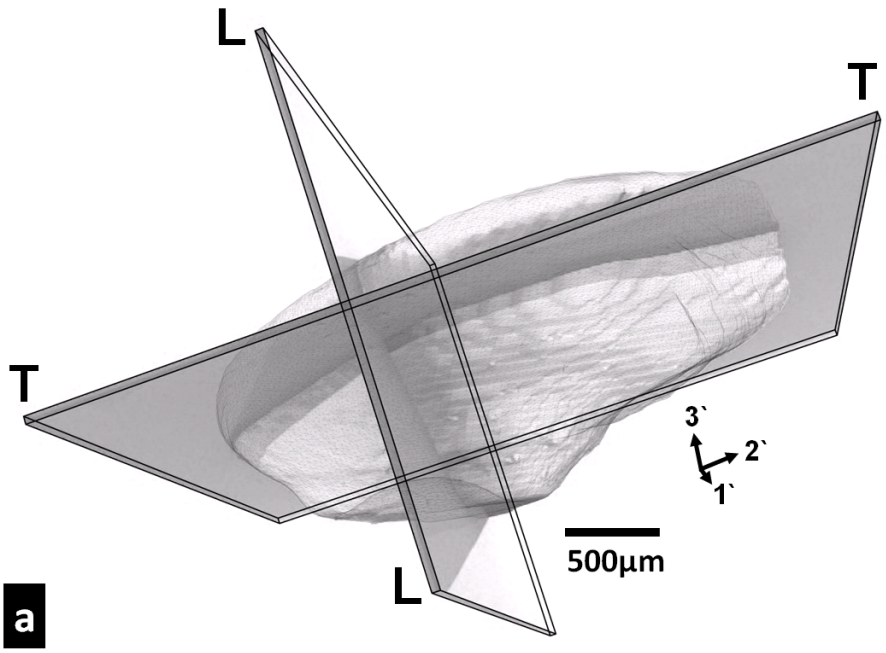
L
T
T
3`
2`
1`
500µm
L
a

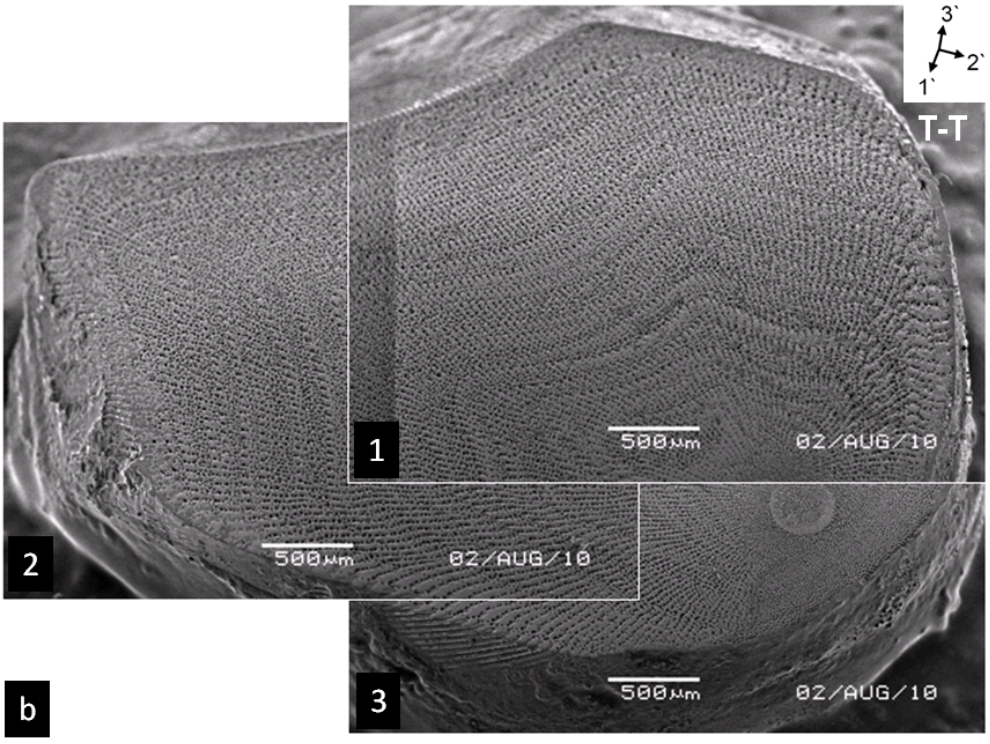
3`
2`
1`
T-T
1
500µm
02/AUG/10
2
500µm
02/AUG/10
3
500µm
02/AUG/10
b

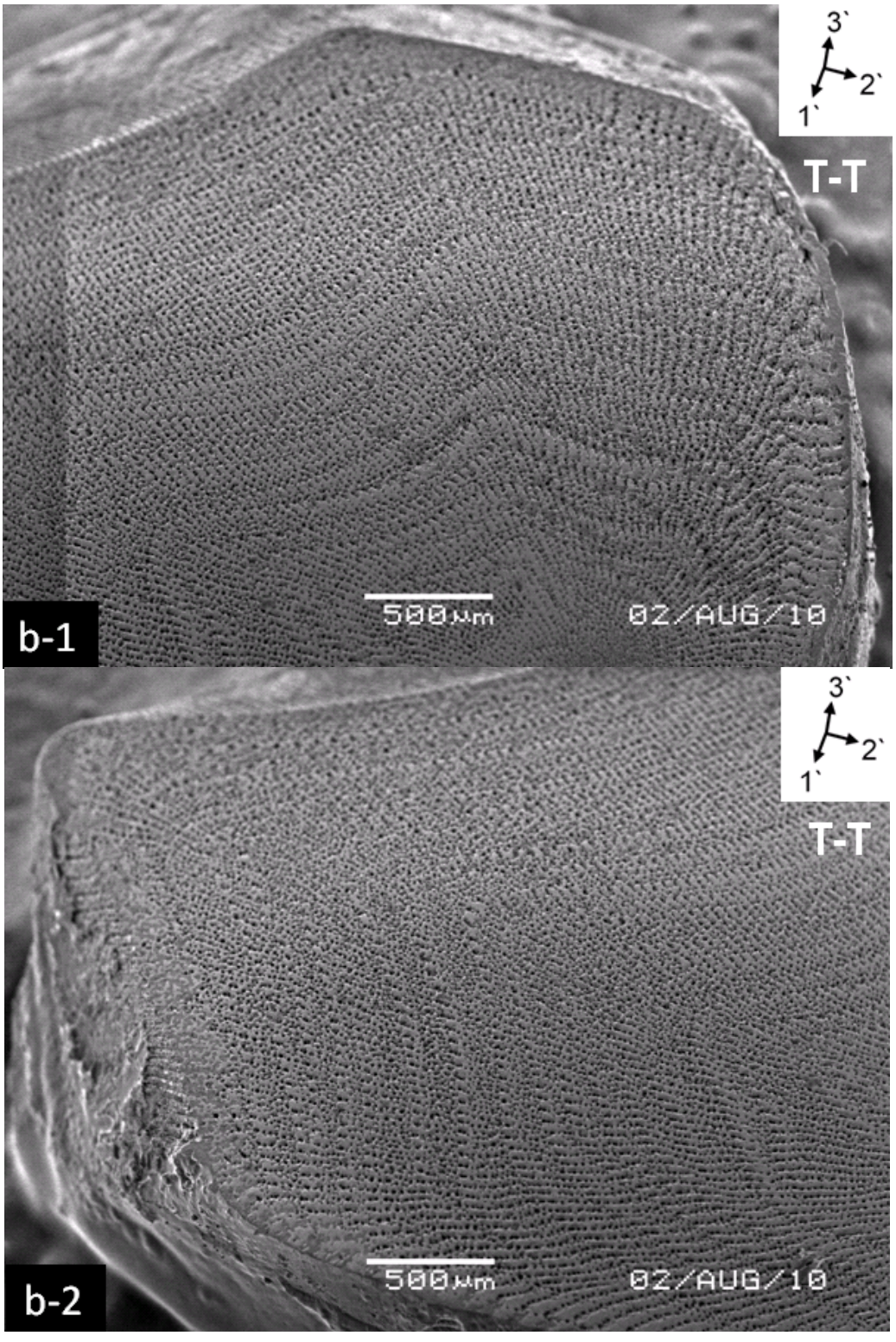
3`
2`
1`
T-T
500㎛
02/AUG/10
b-1
3`
2`
1`
T-T
500㎛
02/AUG/10
b-2

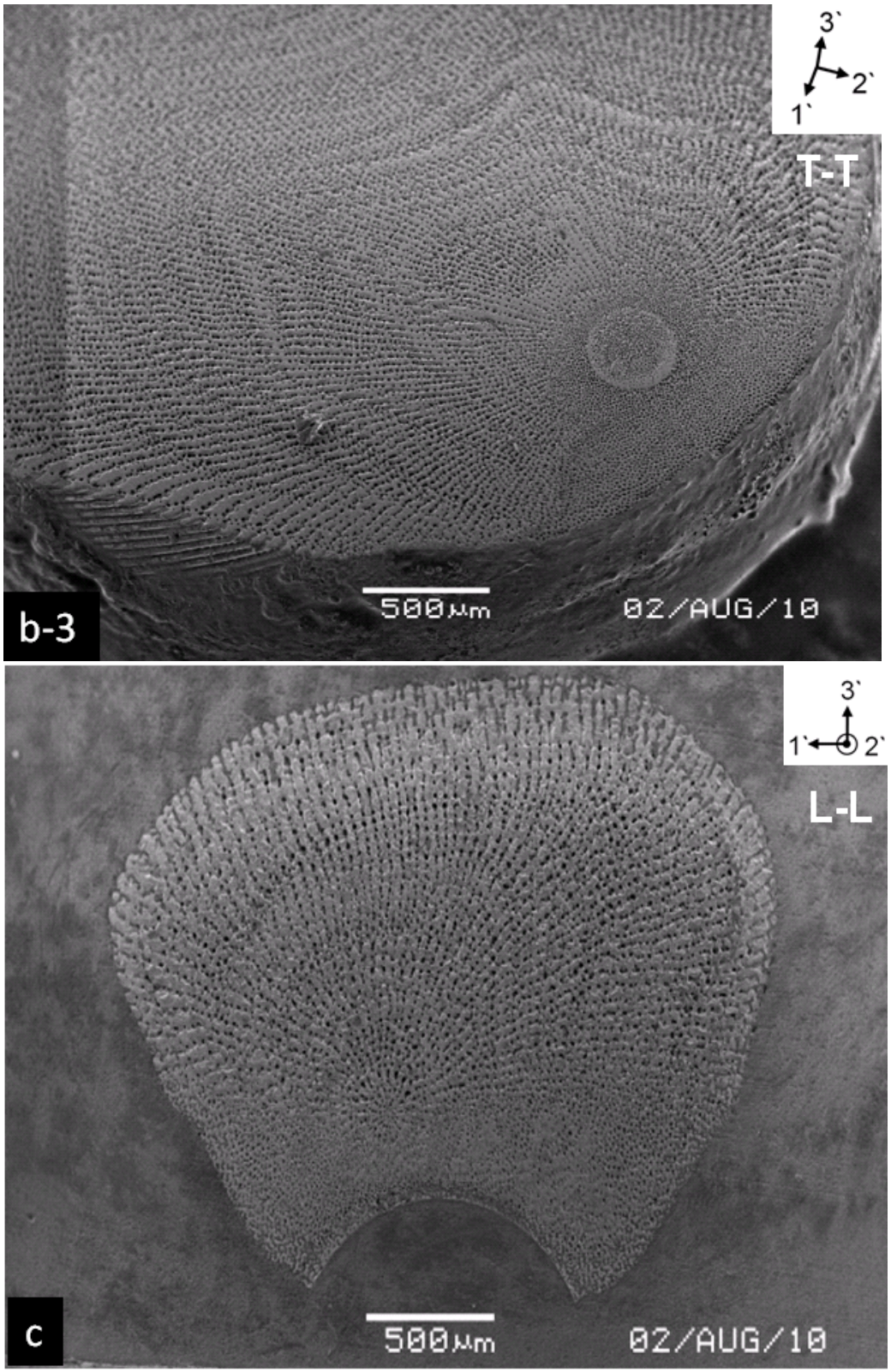


Figure 3-4: SEM images of polished, longitudinal (L-L) and transverse (T-T) cross-sectional surfaces of an aboral spine. (**a)** indicates location of cut plane of an isolated aboral spine**.** (**b-1 to b-3)** are sections of the same T-T cross-section surface (**b**). (**c)** is a longitudinal cut.

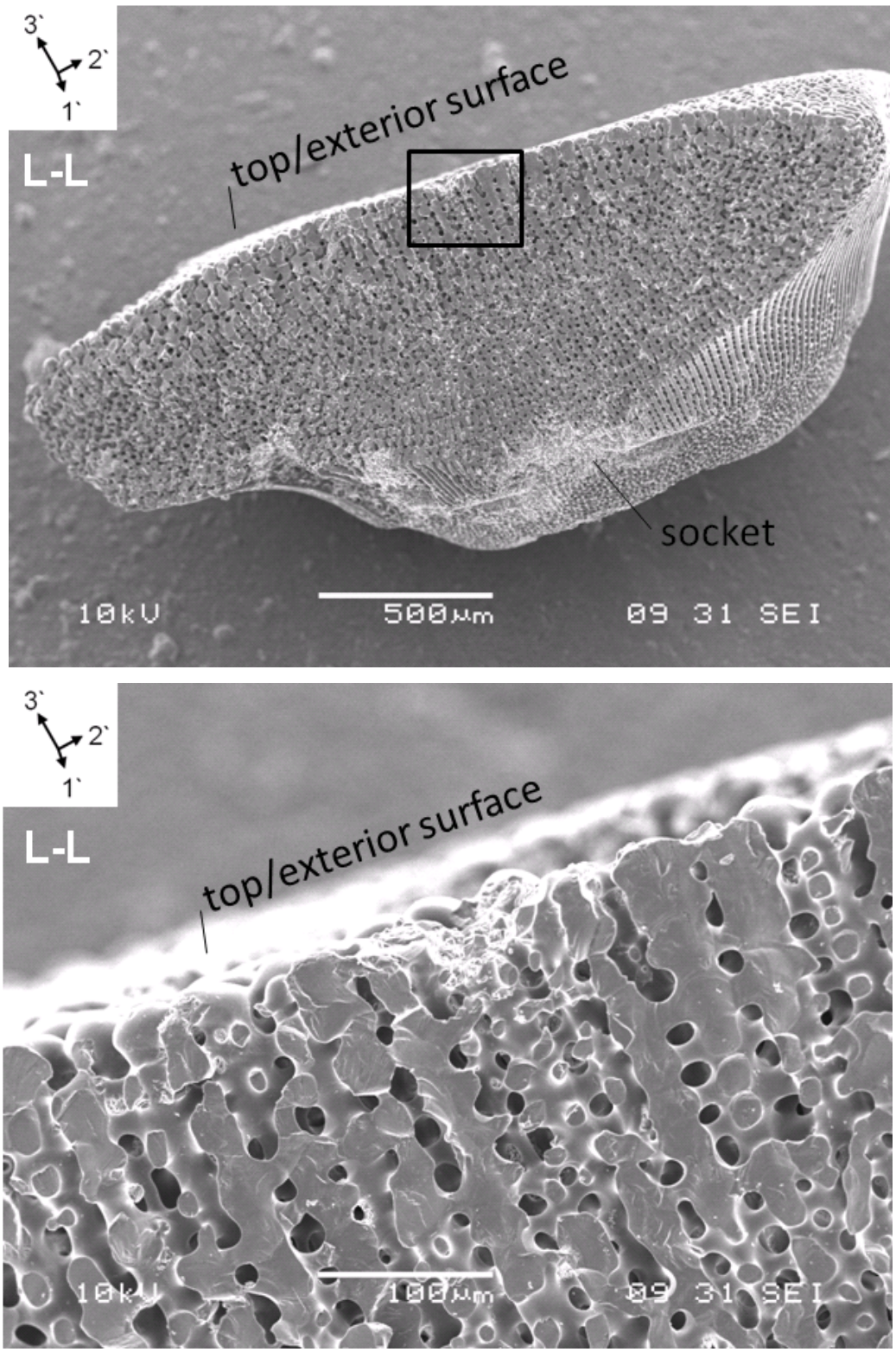


Figure 3-5: Cross-sectional SEM images of fractured aboral spine surface. Right image shows a longitudinal cross-section (L-L) of the galleried structure, oriented perpendicular to the outer plate surface. Aboral spine fractured roughly in the L-L plane (see Figure 3-4.a).

From the cross-sectional micrographs, there seems to be a radial distribution in porosity ranging from the socket (connected to the body) to the outer surface of the plate. From literature, the aboral spines are composed of 3 main types of microstructure geometry: micropreforated, gallery, and labyrinthic (A.B. Smith 1980). Yet, through closer examination with microCT volume reconstruction, the geometry of microperforated, galleried, and labyrinthic microstructure all seem to be variants of a similar geometry. Changes in structure, orientation and porosity are summarized in the schematic showing a cross-section of the test and plate system (Figure 3-6).

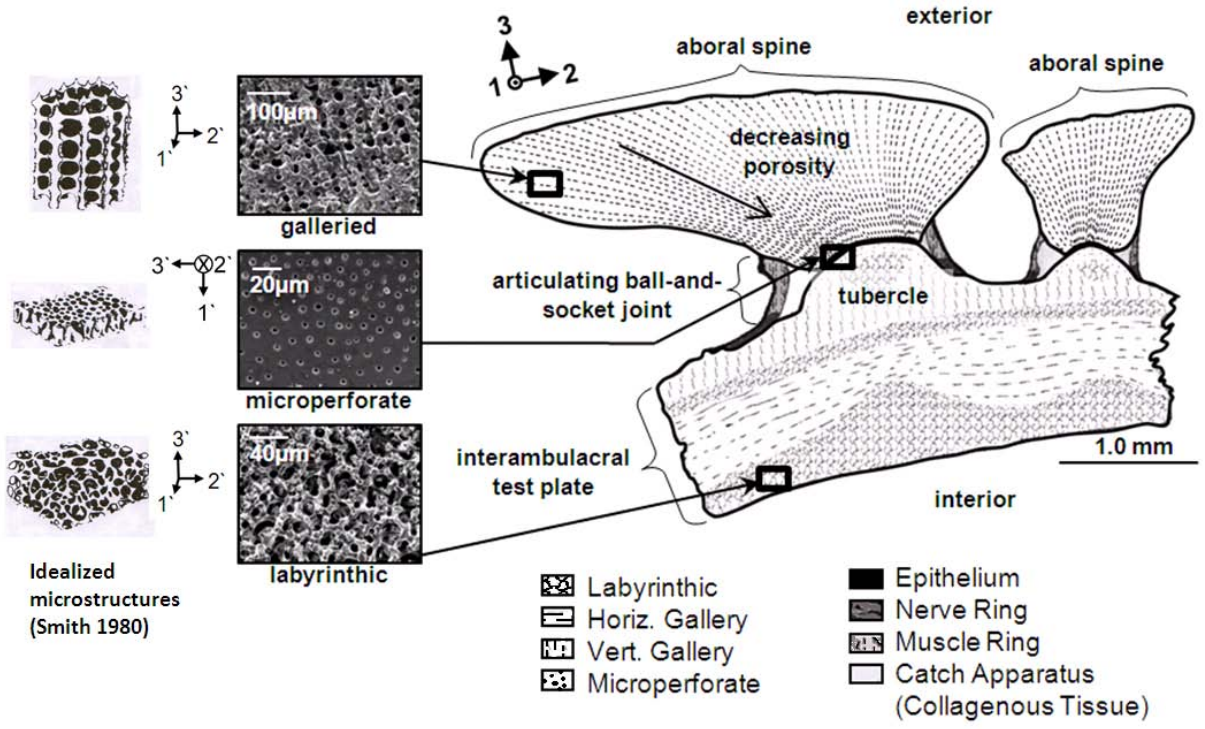


Figure 3-6: Schematic of plate-test system of urchin exoskeleton showing the different microstructural components and orientation of the interambulacral test and aboral spines. Schematic of idealized microstructure (left) reproduced from Smith 1980. SEM micrographs by Elaine Lee, shown with permission.

In identification with microstructural categories proposed by A.B. Smith in 1980 and other literature on echinoderm microstructure, four main structures were found from the SEM

micrographs of various regions in the exoskeleton of the *C. atratus*. The material anisotropy, due to the variation in microstructure, is regionally specific and oriented. From the micrographs in Figure 3-4 and Figure 3-5, the aboral spines were composed almost entirely by a galleried structure, characterized by long, parallel galleries aligned in one direction, with the lateral pores smaller than the long vertical gallery openings (Figure 3-6).

From a cross-sectional SEM image of the test, the upper portion of test plate is also dominated by galleried stereom, with the galleries oriented vertically in the z-direction, perpendicular to the surface of the plate (Figure 3-7.b). Pore sizes range from 9 to 28 micrometers in diameter. At the articulation surface, the microstructure becomes a microperforate layer, around 62 micrometers thick, which is essentially the perforation of the articulation surface by the galleries at that region. Articulation surface of tubercle is also microperforate, while the inner region of the tubercle is labyrinthic.

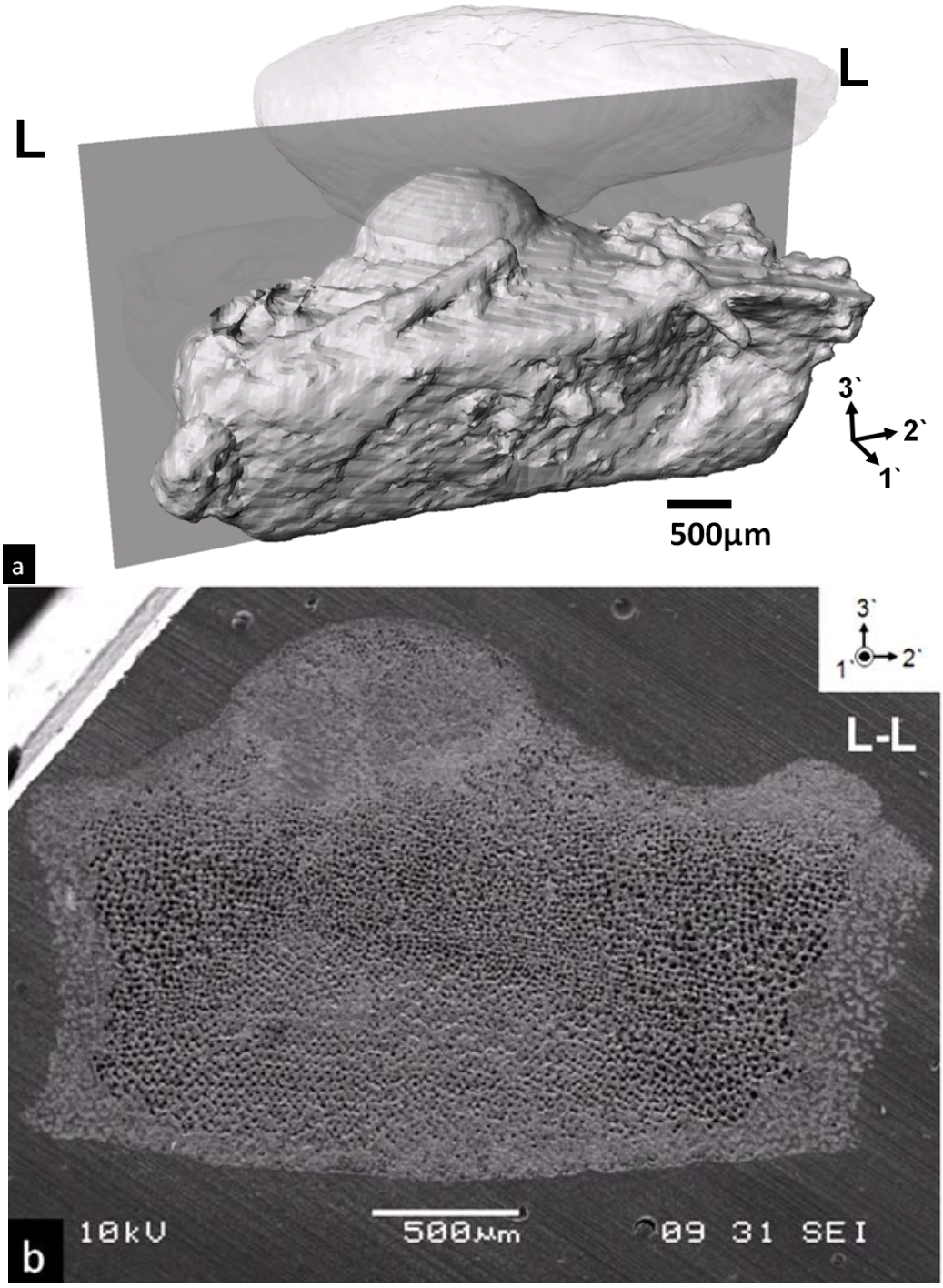
L
L
3`
2`
1`
500µm
a
3`
1`
2`
L-L
10kV
500µm
09 31 SEI
b

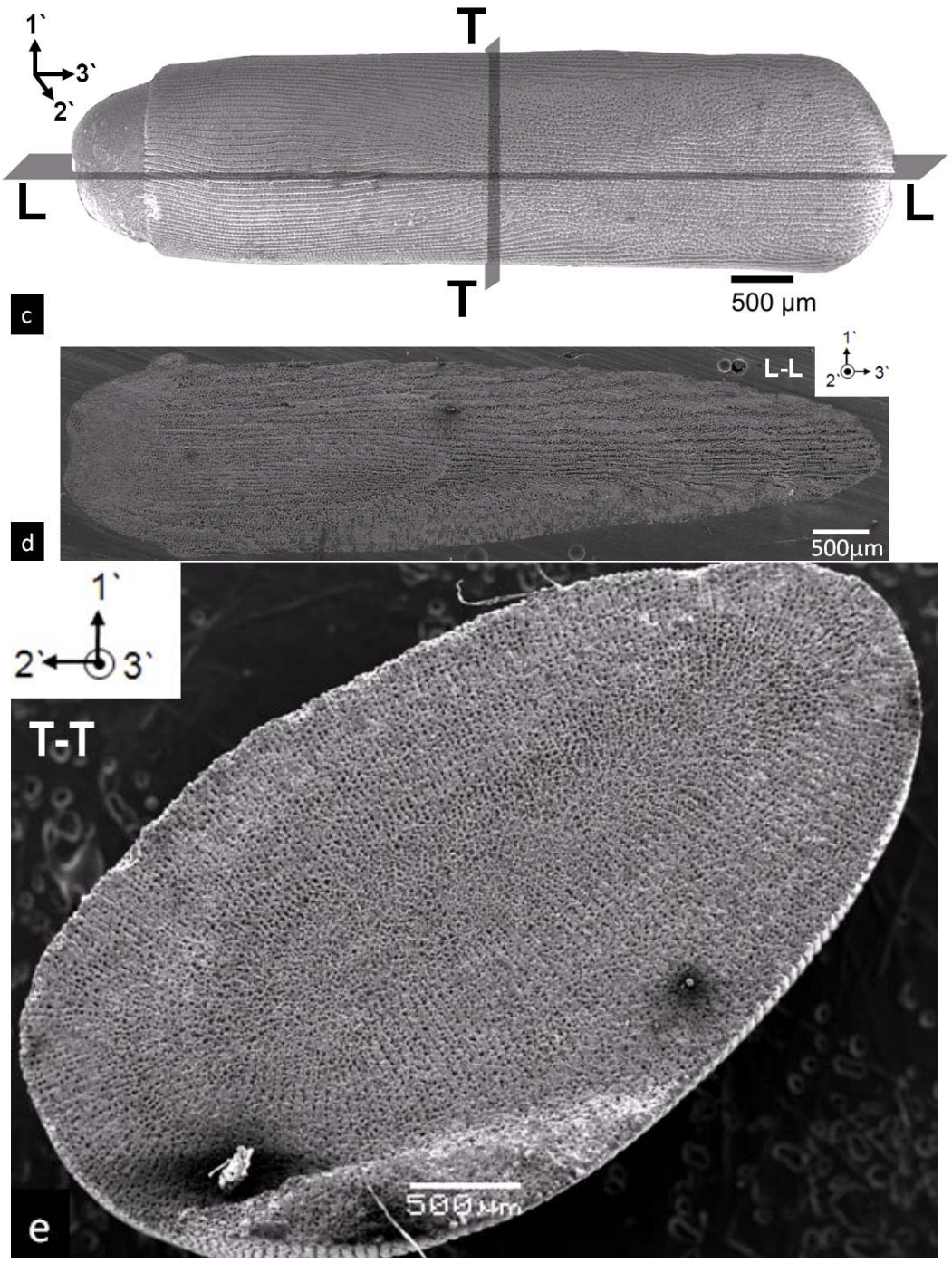


Figure 3-7: (**a**) Schematic of test and plate system showing orientation of longitudinal cut. (**b**) Cross-sectional surface of interambulacral test plate, (**c**) schematic of basal spine showing longitudinal and transverse cuts. (**d**) longitudinal cross section of basal spine, (**e**) transverse cross-section of basal spine. (Images (**d** and **e**) by Elaine Lee, shown with permission).

The test thickness is around 0.96 mm and contains the most variety of microstructures in the exoskeleton. Compared to other echinoderms, the stereom of the *C. atratus's* test has been

found to have a relatively large thickness, high density, and, as commonly found in urchin tests, multiple layers of different porous microstructures (Smith 1980). The tubercles shown have curvatures of 0.011 and 0.023. The gallery region of the test, with the galleries oriented horizontally, parallel to the surface of the test, in the 1`-2` plane. In other (spiny) urchins, long bundles of collagenous fibers were found to penetrate deep into the test along the galleries to a depth of around 25 to 100 μm (Peters 1985). These fibers have been suggested to restrict growth of the crystal calcite by maintaining alignment of the vertical pores. Upper and lower regions of the test are composed of dense labyrinthic. A column of labyrinthic structure also appears aligned vertically directly under the tubercle.

The microstructure of the basal spines exhibited more of a “fascicular” structure rather than the more organized “galleried” structure (Figure 3-7). It has been characterized by rapid, unidirectional growth of the calcite material and suggested to have been derived from the labyrinthic stereom (Smith 1980). The labyrinthic stereom is characterized by an unorganized mesh or 3-dimensional tangle of interconnecting trabeculae. Compared to the other organized structures, this mesh would be more isotropic in strength as well as in growth.

### 3.3 Three-Dimensional microstructure visualization with microcomputed tomography

Although the SEM images revealed the microstructure, an area porosity distribution, and density gradients quite well, there was a limit observing the strut dimensions, the angles between the struts and exactly how the struts were connected in three dimensions because of the uncertainty in the cross-sectional location and angles during the cross-sectioning procedure. There was also difficulty in determining the volume porosity distribution rather than trying to characterize an area porosity of a three-dimensional porous network through a limited number of

two-dimensional slices per plate. In order to exceed the two-dimensional limits of the SEM images, microcomputed tomography was employed to obtain an accurate 3-dimensional visualization of the microstructure.

With lower resolution scans performed using the Scanco MicoCT40, large portions of the urchin could be scanned, such as a section of the urchin's exoskeleton along with the aboral and basal spines (Figure 3-8). From the scans, there is an observable change in morphology in the aboral spines from the apex of the dome to the actinal edge where the basal spines are. The aboral spines closer to the basal spines are typically larger and more elongated than the aboral spines near the apex.

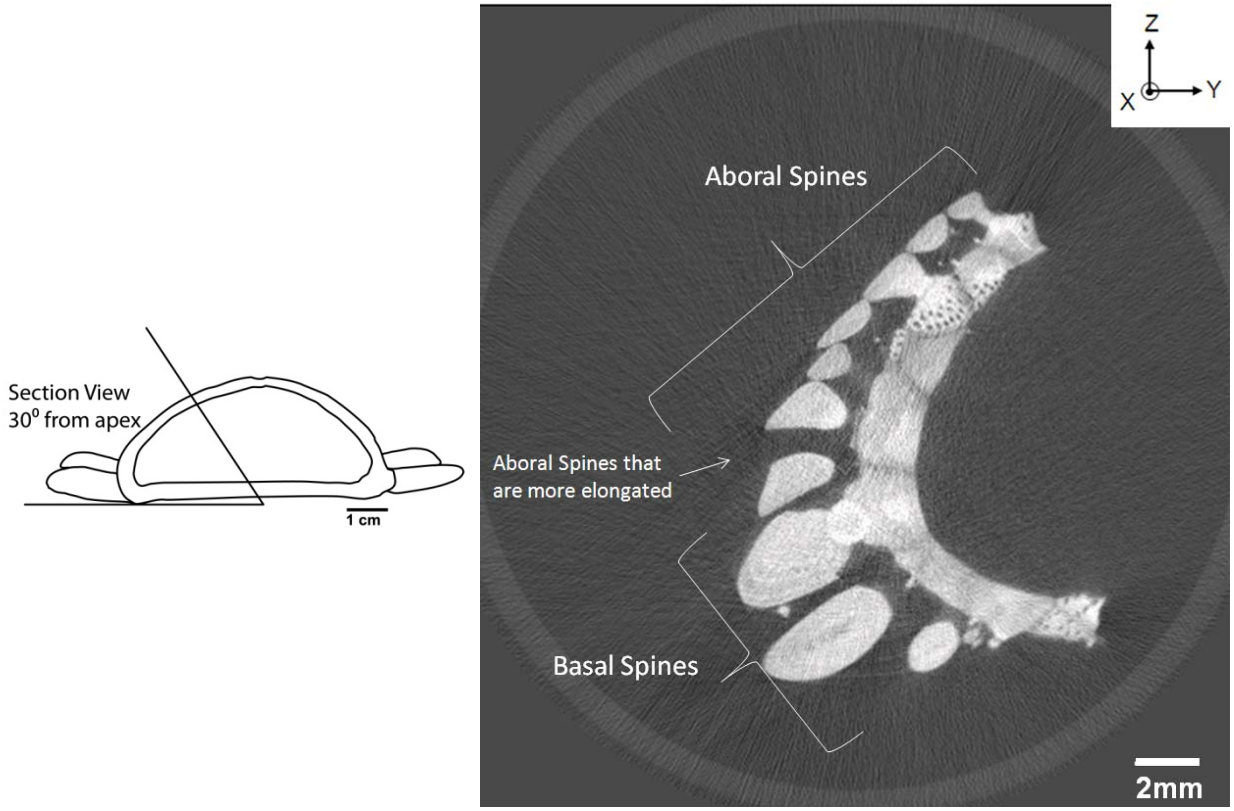


Figure 3-8: Low resolution scan of a section of an urchin exoskeleton. The approximate angle of the section is shown in the schematic to the left. (Scanco MicroCT40, voxel size 30 microns).

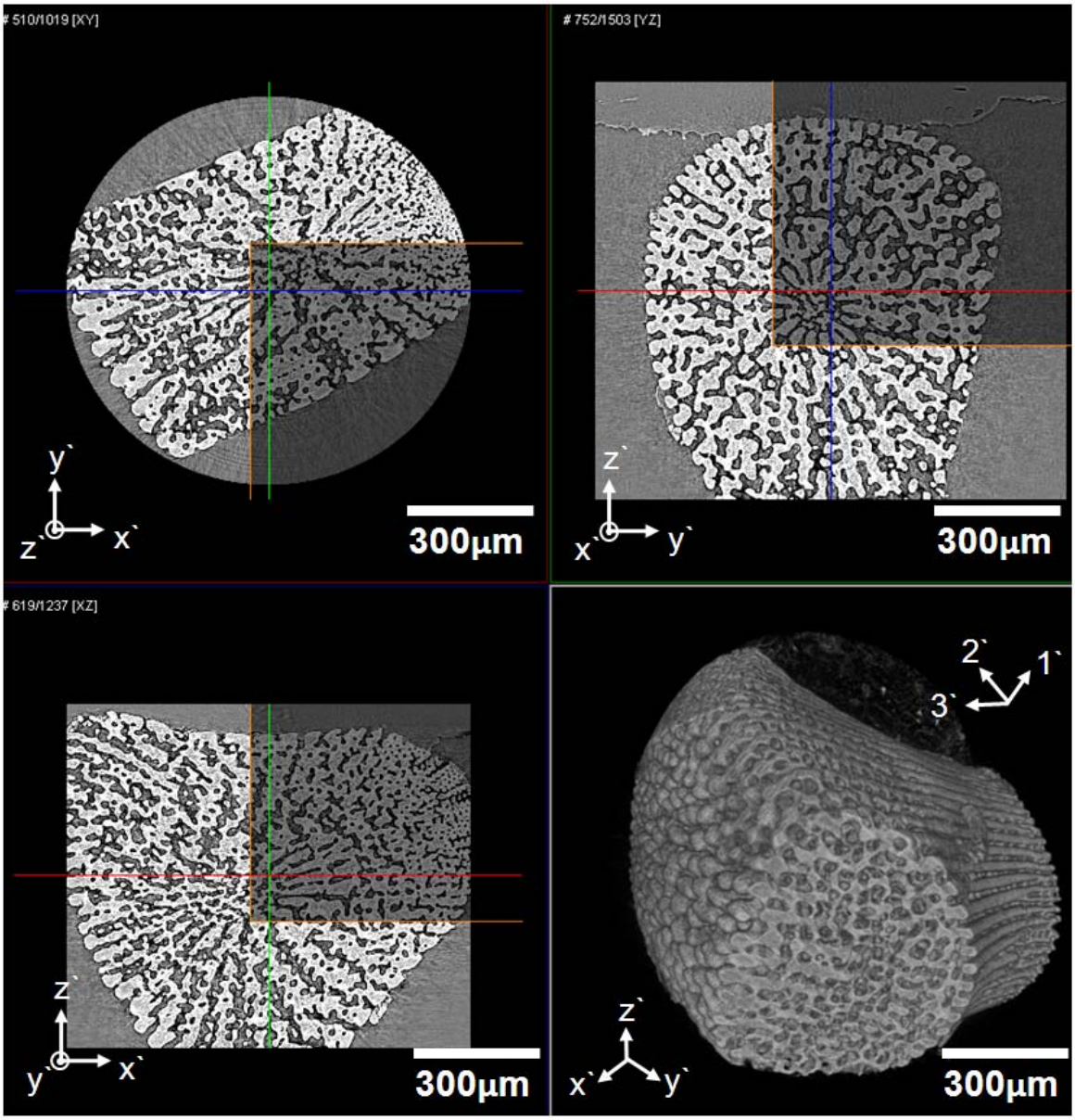


Figure 3-9: Orthogonal slices of a high resolution synchrotron scan and three-dimensional reconstruction of the aboral spine (APS 2BM, voxel size 0.7 microns). In the lower right figure, a portion of the three-dimensional volume is cut out to reveal the interior microstructure.

While both are similar, nondestructive methods of obtaining internal and external microstructural information of the specimen, the X-ray microtomography system at the APS proved to be ideal for the urchin aboral spines and test plates since it was able to surpass the resolution limitation of the Scanco microCT machine and allowed clear visualization of the microporous structure. Yet, because of the larger field of view with the Scanco machine, the

macroscopic geometry of the test and arrangement of several spines were able to be obtained from a single scan. From APS, the actual porous network and whole plate was obtained, but due to the smaller field of view, an aboral spine of smaller than average size was used. For this thesis, the data from APS was more relevant to the microstructural study of the aboral spine so more emphasis was placed on processing the data from the X-ray scans at APS.

### 3.4 Isolation of the repeating unit of the gallery structure

The raw, reconstructed slices from the X-ray scans were imported into ImageJ to re-orient the slices to be perpendicular to the axis of the aboral spine and converted to bitmap format. The slices were then imported into Mimics for thresholding and segmentation. The threshold mask, to exclude noise, ranged from a value of 1000 to 3056. This threshold was determined visually such that the threshold was large enough to maintain the microstructure's solidity (no internal voids) and connectivity observed in the SEM images. After the threshold mask, a multi-slice region grow operation was performed on the mask to exclude detached noise from the mask. To fill in the extraneous voids within the mask due to contrast noise, a multi-slice cavity fill operation on the background was performed to create a "mold" of the porous volume and a second cavity fill operation in the mold was performed to obtain the final volume (Figure 3-10). The entire aboral spine volumes were then subdivided into small cubic units to analyze for local porosity, structural dimensions, and isolation of representative unit volumes in a mesh editing software, Rhinoceros.

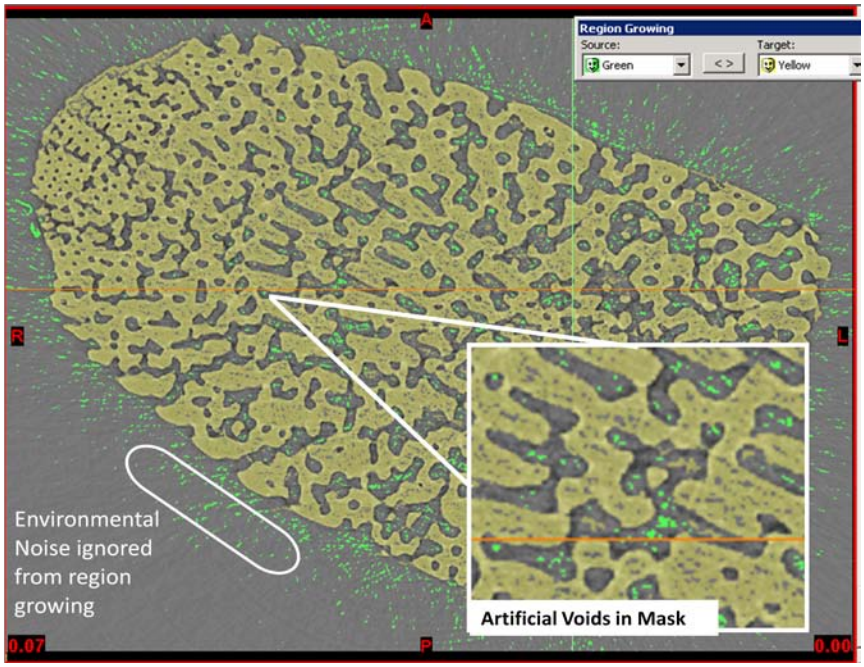


Figure 3-10: Segmentation of X-ray tomography scans

Because of the high resolution of the scans, extracted cubic units can be further analyzed to isolate the repeating elements that combine to create the microscopic structure and porous network. Consistent with literature and prior SEM images, the gallery element was found, which has a thick axial strut roughly 30 microns in diameter and six transversal struts, of diameter around 12 microns, that connect to neighboring axial struts (Figure 3-11 and 3-12). The axial strut actually extends, unbroken, from the socket region to the top surface of the aboral spine. With pieces are extracted from different regions of the aboral spine, the regional dependence of the features (such as strut lengths, strut diameter, strut spacing and spatial arrangement of the struts) in the microstructure can be determined as well as any trends in the change of the features in the repeating unit. Although the entire aboral spine seems to be composed of variants of this repeating galleried structure, these slight microstructural differences between regions of the

aboral spine correspond to porosity differences and may even correspond to a functional mechanical difference for the aboral spine as a whole.

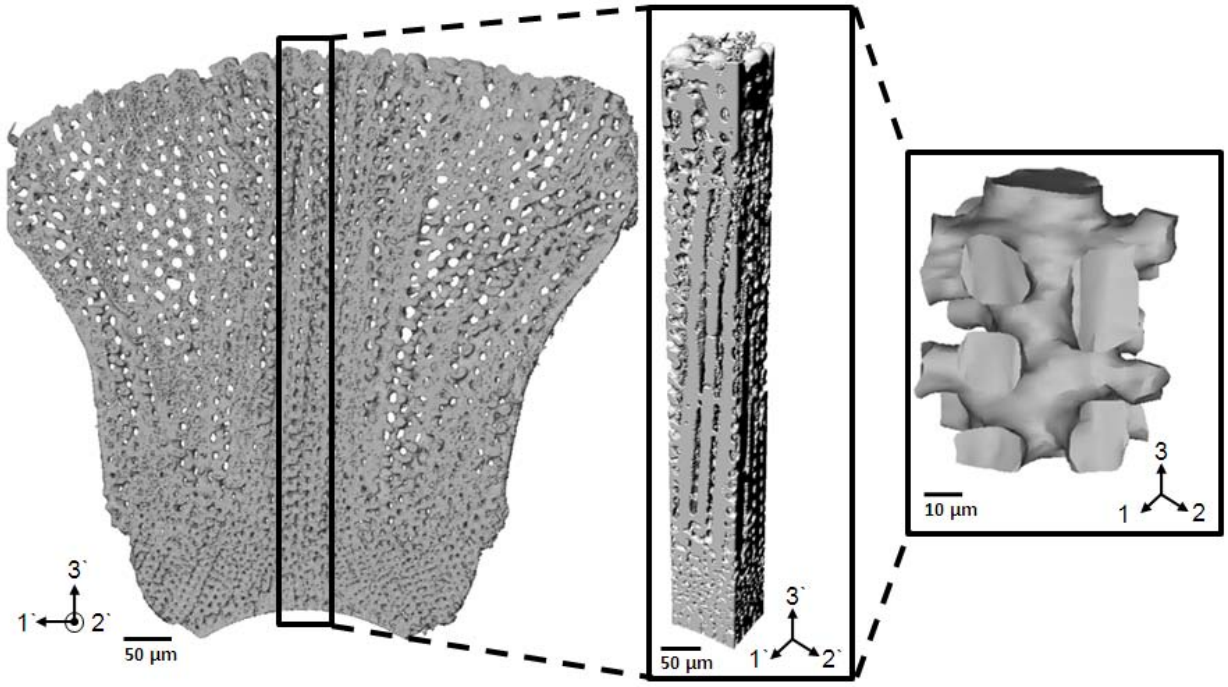


Figure 3-11: Extraction of isolated repeating gallery unit from cubic units of reconstructed scans of the aboral spine.

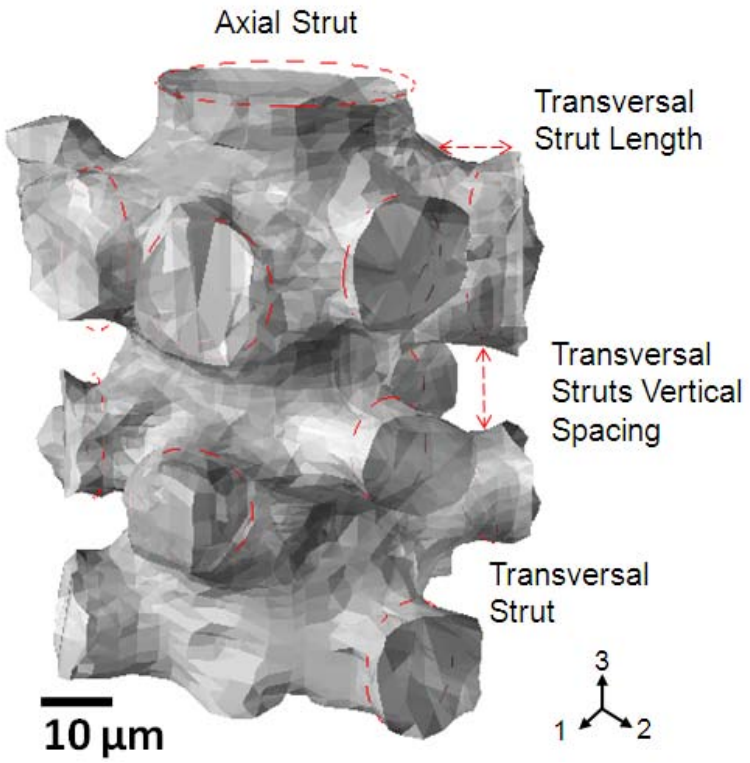

Figure 3-12: Identification of the four key parameters of the repeating gallery unit.

Table 3-2: Measured quantities of isolated gallery unit.

| Sample | Trans Strut Diameter | Axial Strut Diameter | Trans Strut Vert. Spacing | Trans Strut Length | Porosity |
|---|---|---|---|---|---|
| **B1s2 Piece 5 (near socket)** | 13.8 µm | 30.2 µm | 12.5 µm | 6.4 µm | 37.2% |
| **B1s2 Piece 11 (near top)** | 13.5 µm | 28.9 µm | 10.6 µm | 9.3 µm | 26.1% |
| **A1s1 Piece 14 (near top)** | 10.7 µm | 11.7 µm | 12.8 µm | 6.2 µm | 31.5% |

### 3.5 Characterization of the Microporous Network

The advantage of possessing a three-dimensional scan of the aboral spine at high resolution is the ability to fully characterize the microporous network within micrometers as a whole as well as locally within spatial regions of the aboral spine. Because of the high resolution required

to obtain accurate imaging of the smallest pores in the aboral spines and the limited field of view of the high resolution scans, aboral spines near the apex of the exoskeletal dome were used because they are smaller than the majority of the aboral spines tiling the exoskeleton of the urchin, which range from 1mm to 4mm. Both of the samples, named “a1s1” and “b1s2”, are from the region surrounding the anus of the urchin, near the apex of the urchin’s exoskeletal dome (Figure 3-1). Sample “b1s2” was scanned with a 5x lens at a resolution of 1.4μm while sample “a1s1” utilized a 10x lens to achieve a scan with a resolution of 0.7μm. Both scans were performed with 1500 projections at voltage of 15keV.

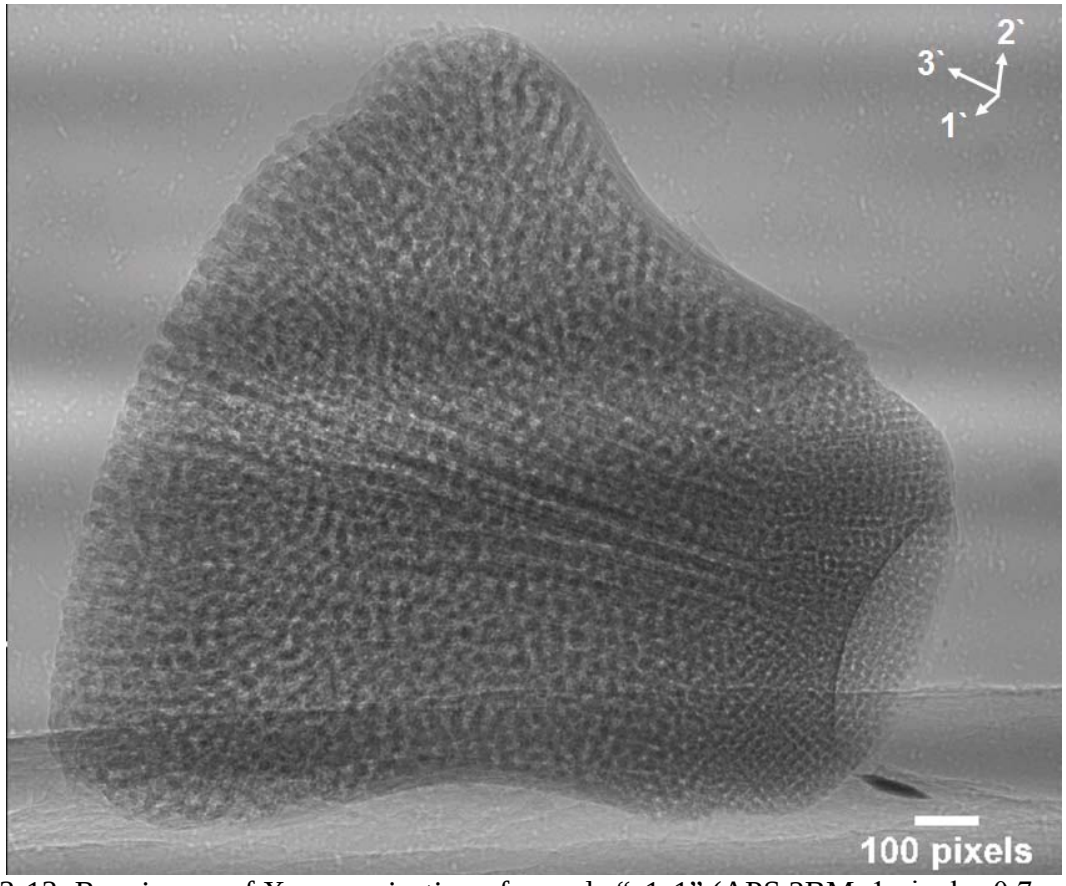

Figure 3-13: Raw image of X-ray projection of sample “a1s1” (APS 2BM, 1 pixel = 0.7μm).

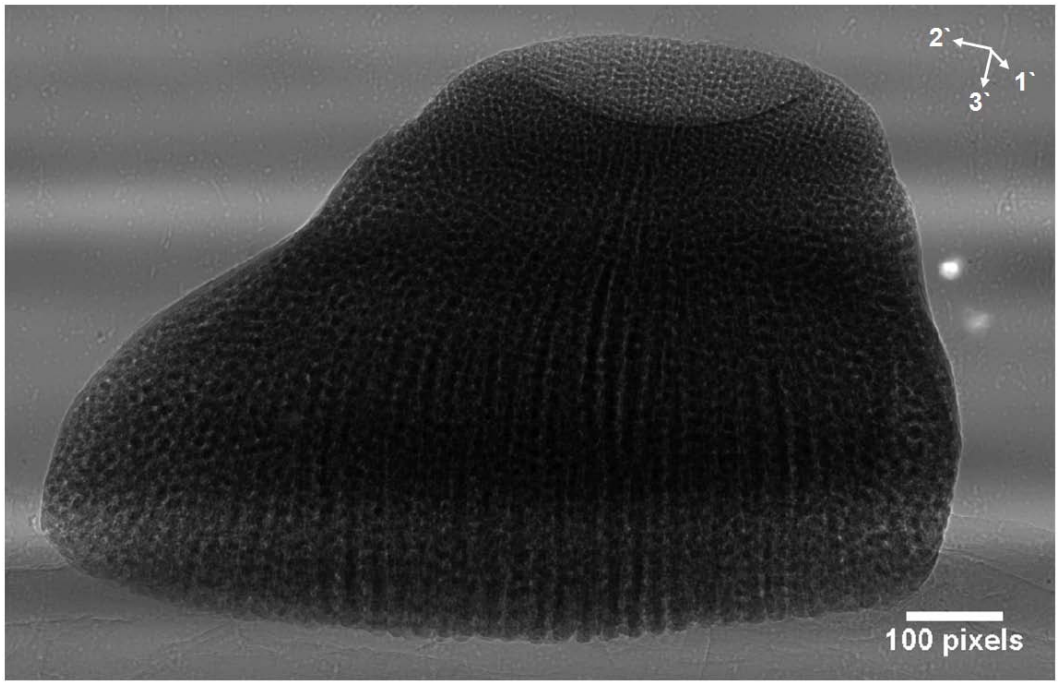

Figure 3-14: Raw image of X-ray projection 74 of sample “b1s2” (APS 2BM, 1 pixel = 1.4μm).

By extracting small row or column regions from the aboral plate scans, localized volume fraction calculations were done on samples “a1s1” and “b1s2”. Within the software Rhinoceros, the volume fraction was determined by creating a bounding box of each cubic volume and subsequently calculating the fraction of the box the volume occupies. Using sequential cubic volumes extracted from the aboral spines, a porosity distribution along the aboral spine axis and transverse direction was calculated from the volume fractions for two aboral spines. For both samples “a1s1” and “b1s2”, an axial stack of cubic volumes were extracted and the volume fraction was calculated for each of the cubic volumes in the column (Figures 3-15, 3-16, 3-19 and 3-20). Additionally, for sample “a1s1”, a radial row of cubic volumes were extracted to determine if there is any significant porosity distribution in the transverse direction (Figures 3-17 and 3-18).

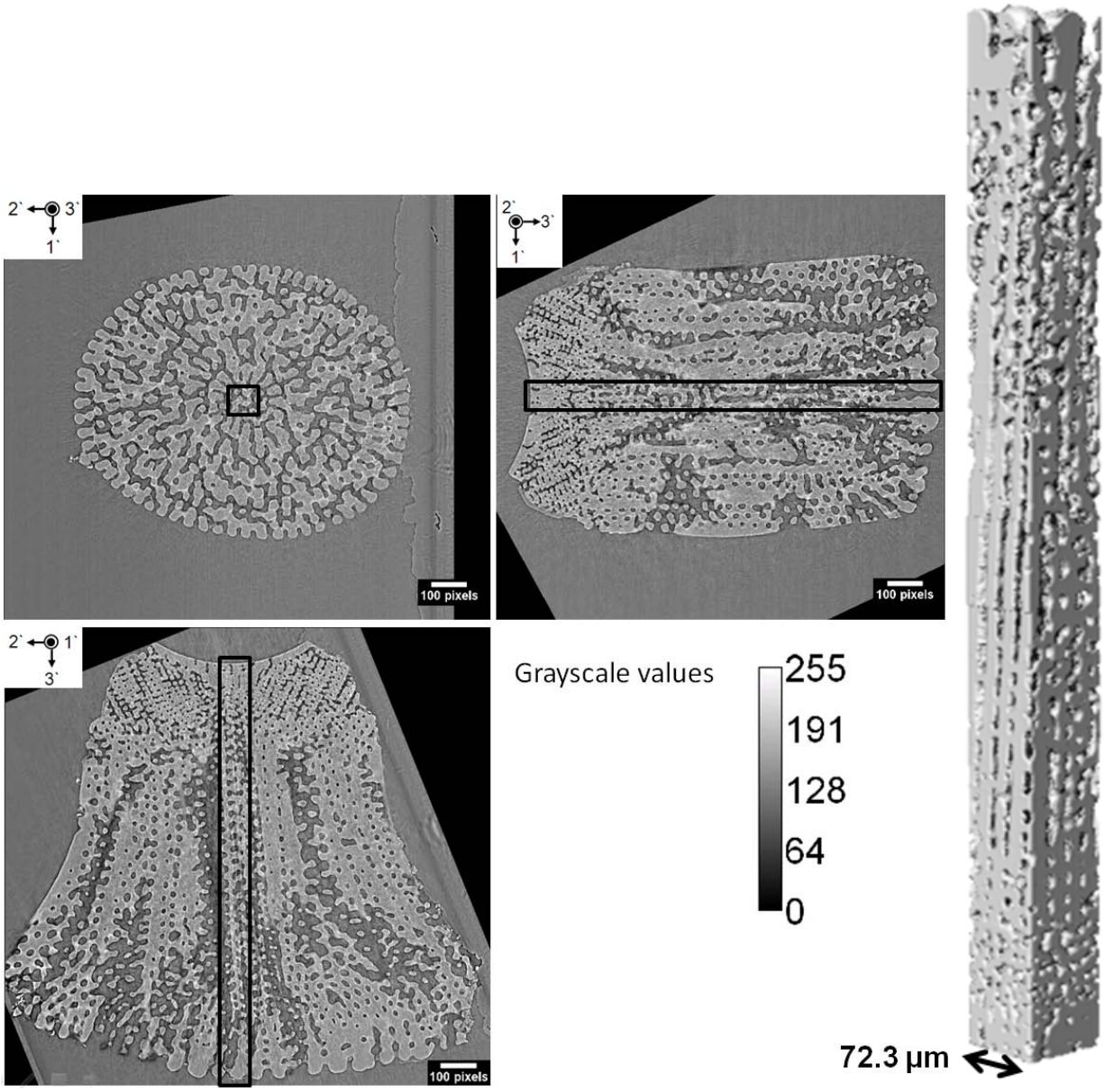


Figure 3-15: Three-dimensional reconstruction of the center axial column of the aboral spine "**a1s1**". Composed of 15 vertically stacked cubic volumes (72.3 x 72.3 x 72.3 µm) extracted from X-ray reconstructed images (dimensions: 72.3 x 72.3 x 806.5 µm). Scans from APS 2BM.

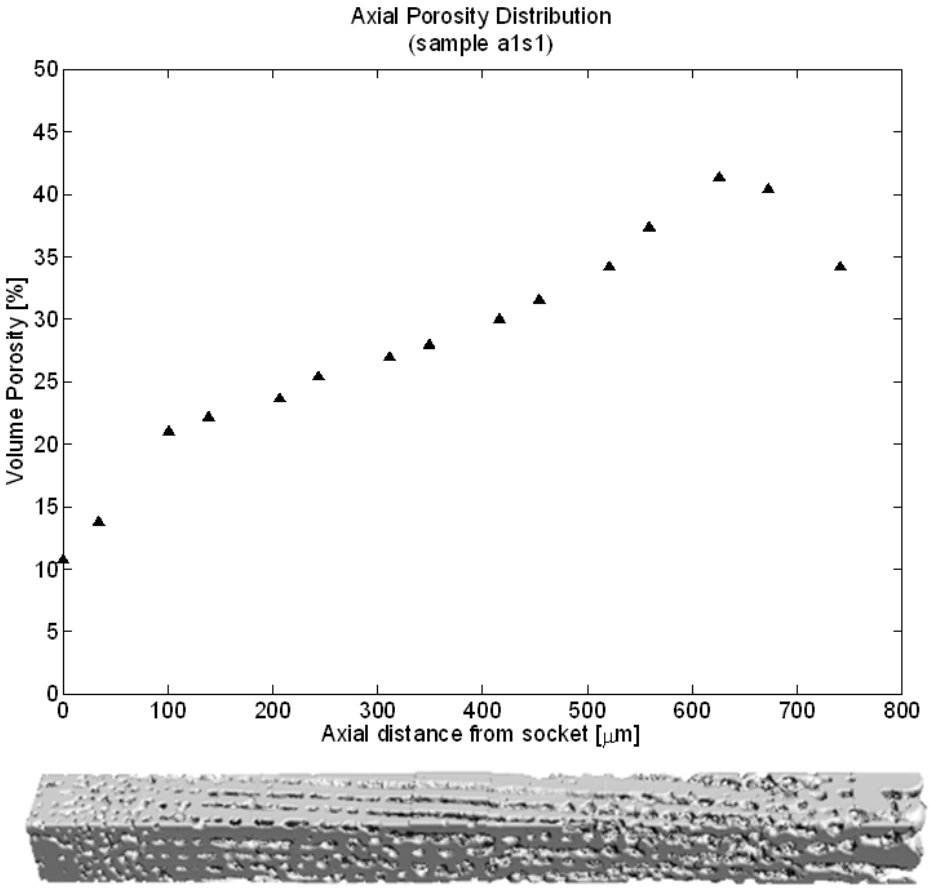


Figure 3-16: Volume porosity distribution of axial column extracted from sample "**a1s1**".

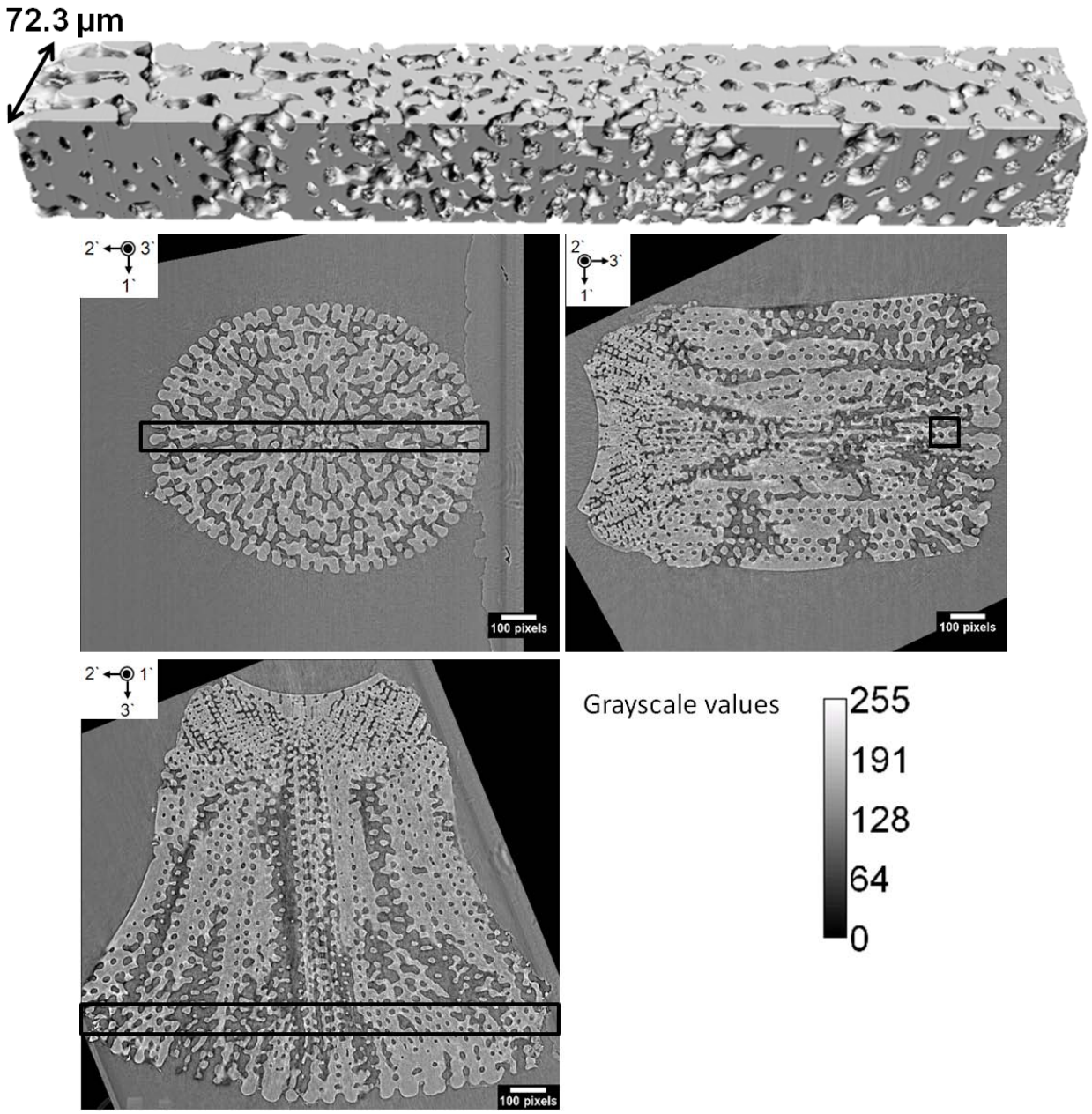


Figure 3-17: Three-dimensional reconstruction of the top radial row of the aboral spine "**a1s1**". Composed of 17 horizontally stacked cubic volumes (72.3 x 72.3 x 72.3 µm) extracted from X-ray reconstructed images (dimensions: 72.3 x 72.3 x 818.9 µm). Scans from APS 2BM.

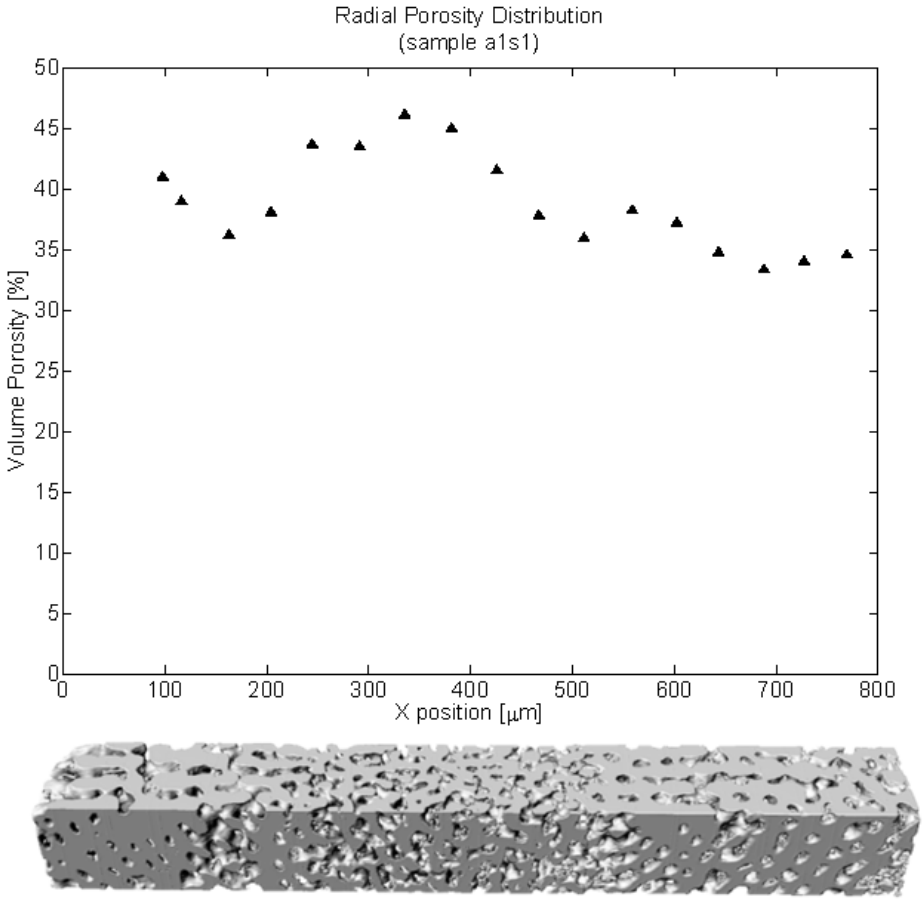


Figure 3-18: Volume porosity distribution of radial row extracted from sample "**a1s1**" with an average volume porosity of 38.5% (standard deviation=3.7%).

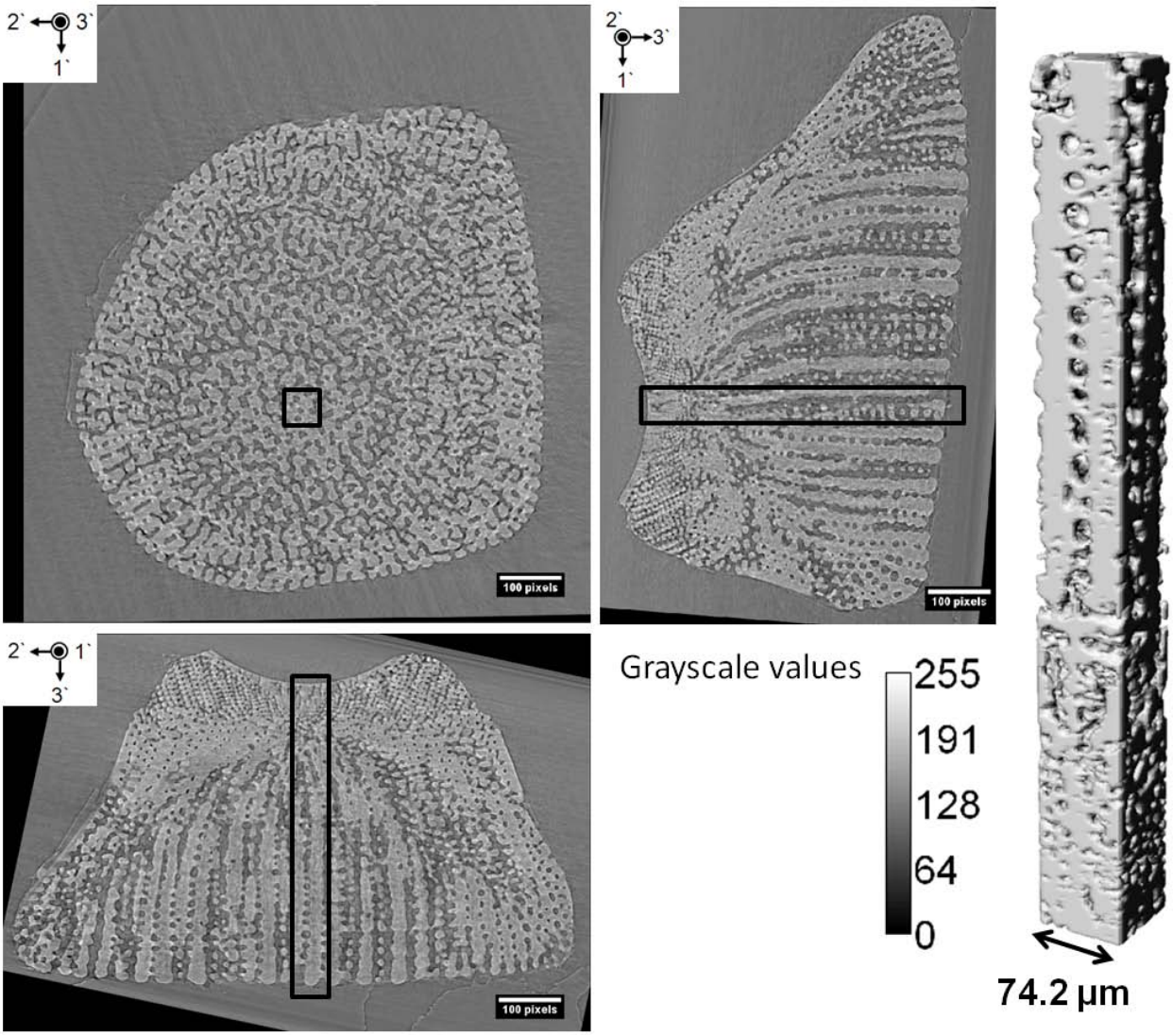


Figure 3-19: Three-dimensional reconstruction of the center axial column of the aboral spine "**b1s2**". Composed of 13 vertically stacked cubic volumes (74.2 x 74.2 x 74.2 µm) extracted from X-ray reconstructed images (dimensions: 74.2 x 74.2 x 660.8 µm). Scans from APS 2BM.

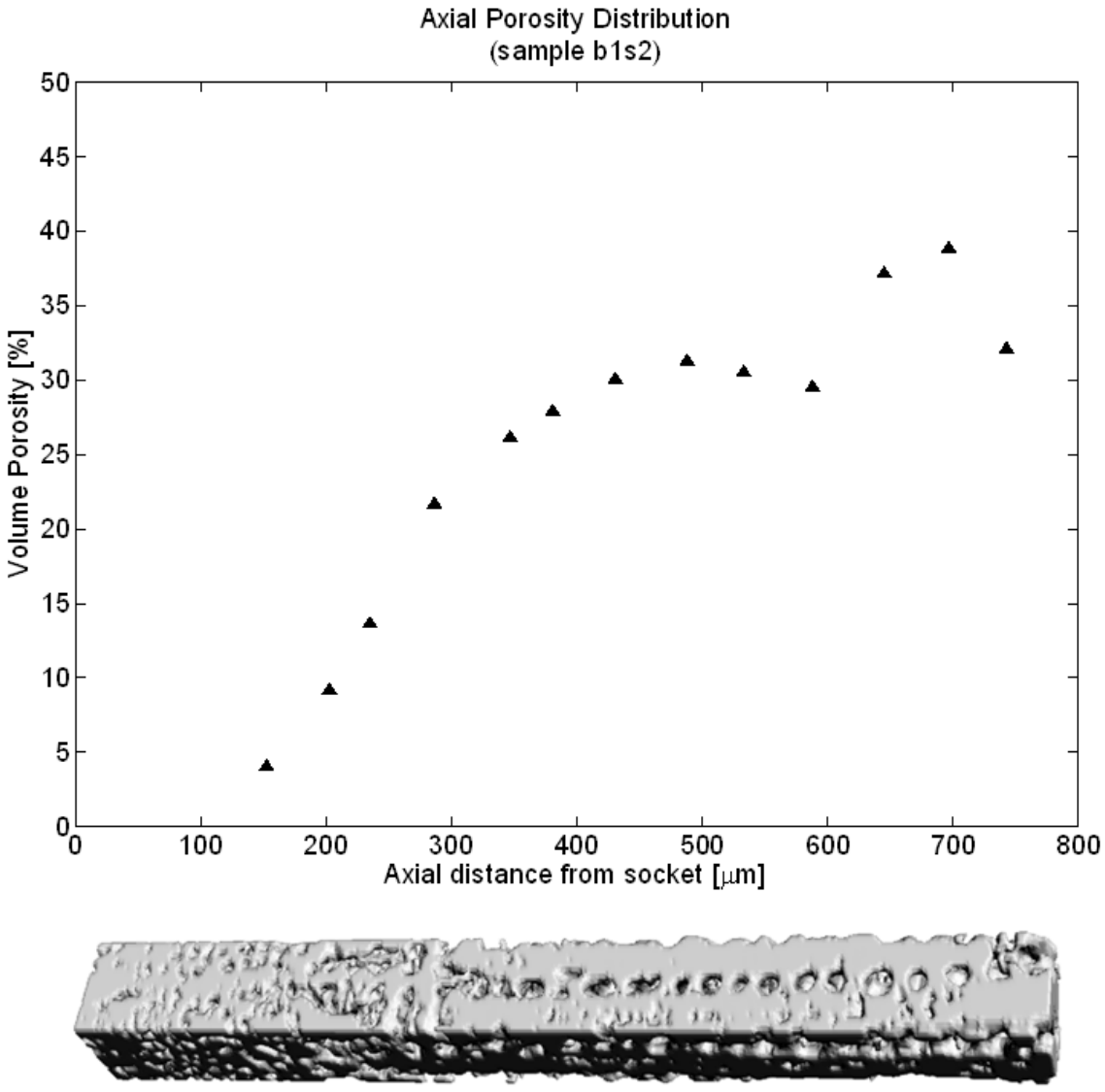


Figure 3-20: Volume porosity distribution of axial column extracted from sample "**b1s2**".

The axial porosity distribution from the two separate aboral spines were combined and plotted in Figure 3-21 for comparison. Referring back to the data collected from SEM images, the areal porosity distribution calculated from an image of the socket surface (Figure 3-3.d) is also indicated in the plot.

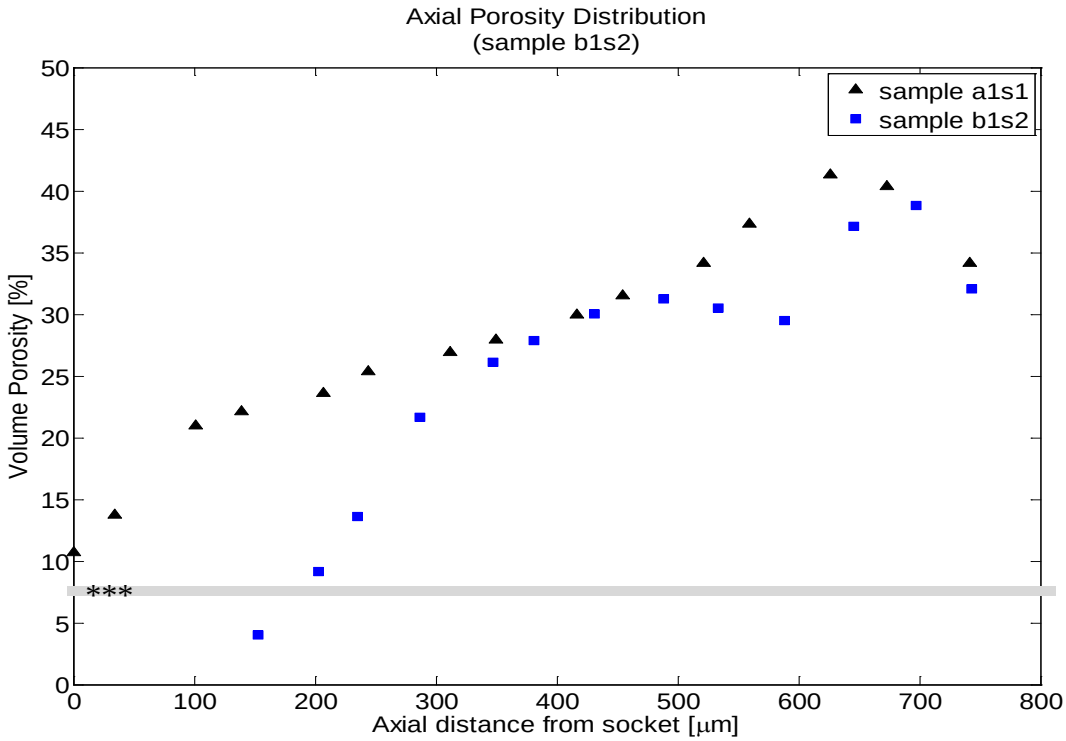


Figure 3-21: Volume porosity distribution of axial column extracted from samples "**a1s1**" and "**b1s2**". (******* 7.2% Area Porosity calculated from SEM image of socket, figure 3-3.d)

The axial porosity of aboral spines "a1s1" and "b1s2" both exhibit a similar trend of increasing volume porosity with increasing axial distance from the socket joint of the aboral spine. In both aboral spines, the axial porosity increases from 5% or 10% volume porosity to around 40% porosity, with the porosity dropping slightly at the region near the top of the aboral spine. This drop may be attributed to the bulbous geometry at the exterior surface of the aboral spine, causing more material volume near the surface. In the transverse direction, the porosity distribution is fairly constant across the aboral spine about a mean porosity. Essentially, the aboral spines have a radial distribution of porosity, where the porosity increases linearly from the socket to the surface of the aboral spine along radial lines created by the axial struts. The unbroken line of the axial struts maintains 6 connections via transversal struts to neighboring axial struts, such that the angle between the struts is 60 degrees. The transversal struts

themselves are horizontally aligned and the majority of the struts not staggered in vertical position. Along the length of the axial strut, there are a couple of instances where small buds of transversal struts appear, disrupting the regularity of the transversal strut arrangement.

To quantify these observations, a continuous column of the axial strut along with the transversal struts was digitally isolated from the same axial column of the aboral spine sample "b1s2" used in the porosity calculations using the three-dimensional mesh editing software, Rhinoceros. The strut was isolated until 152.6μm from the socket because the X-ray scan resolution (1.4μm) was not high enough to resolve small pores near the socket region. Using a custom script within Rhinoceros, the center point of each strut was found, a circle was fitted to the mesh points of each strut and the axial strut circles were lofted to create a representation of the connected axial strut (Figure 3-22). From the derived circles, the radii of both the axial and transverse struts can be approximated. For the transversal strut radii and lengths, the measured values at a certain distance from the socket region were averaged.

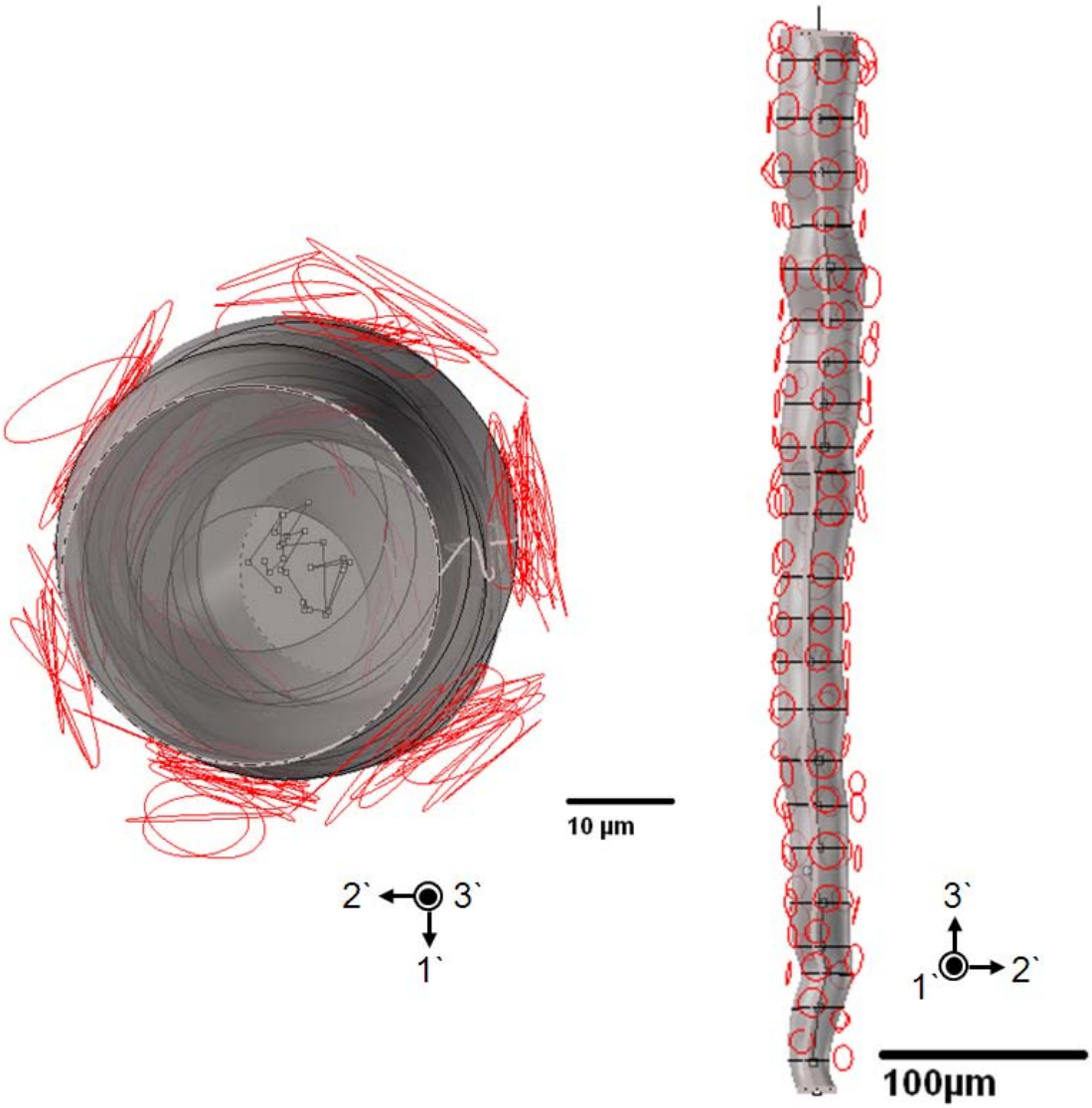


Figure 3-22: Top view (left) and right view (right) of an isolated central axial column of the galleried structure from sample “b1s2”. Spatial distribution of transversal struts and alignment of axial strut from circular fit of strut diameters, shown in red. The surface loft of axial struts along length of isolated galleried structure, shown in light gray.

The four key parameters, axial strut radius (ASR), transversal strut radius (TSR), transversal strut half-length (TSL), and transversal strut vertical spacing along the length of the axial column were measured and plotted as a function of distance from the socket (Figure 3-23). Of the four parameters, while the transversal strut radii does not change significantly, the axial strut radii and the transversal strut vertical spacing increase as the distance from the socket

increases. Also note, there is a slight increase in the transversal strut length. This is consistent with the two-dimensional images from SEM and microCT slices of the aboral spines. Since the transversal strut radius stays relatively constant and the axial strut radii are smaller nearer to the socket, what causes the increase in porosity further away from the socket is the increase in the transversal strut length. Because there are six struts to account for, a slight increase in transversal strut length causes a large increase in porosity as seen in Figure 3-24, where an increase in the transversal strut length by 2 microns can increase the porosity by as much as 10%. An increase in the axial strut radius, on the other hand, has a more subtle effect on the porosity. Thus, in Figure 3-23, the increase in axial strut radius (ASR) is compensated by the slight increase in transversal strut radius (TSL) along with the transversal strut vertical spacing (ASL) to cause the porosity increase observed in Figure 3-21. The abrupt jumps in the values may reflect to distortion of the gallery structure within the oblong aboral spine and the growth rings observed in the SEM micrographs.

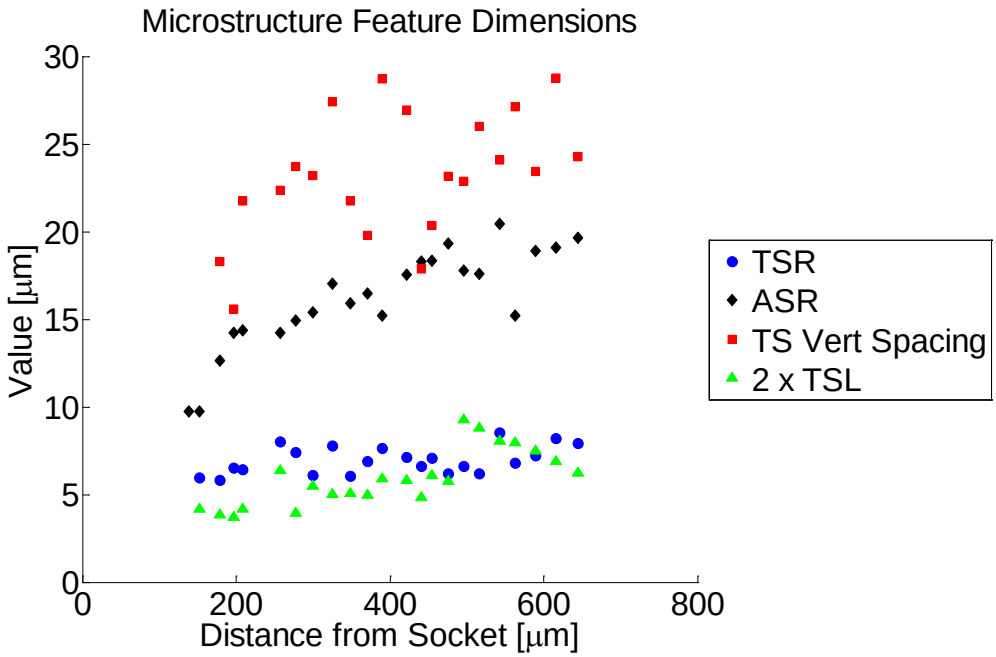


Figure 3-23: The four feature parameters from the quantitative analysis of the synchrotron microstructural scans. TSR=Transversal Strut Radius, ASR=Axial Strut Radius, TS Vert Dist=Transversal Strut Vertical Spacing, 2 x TSL= Transversal Strut Length

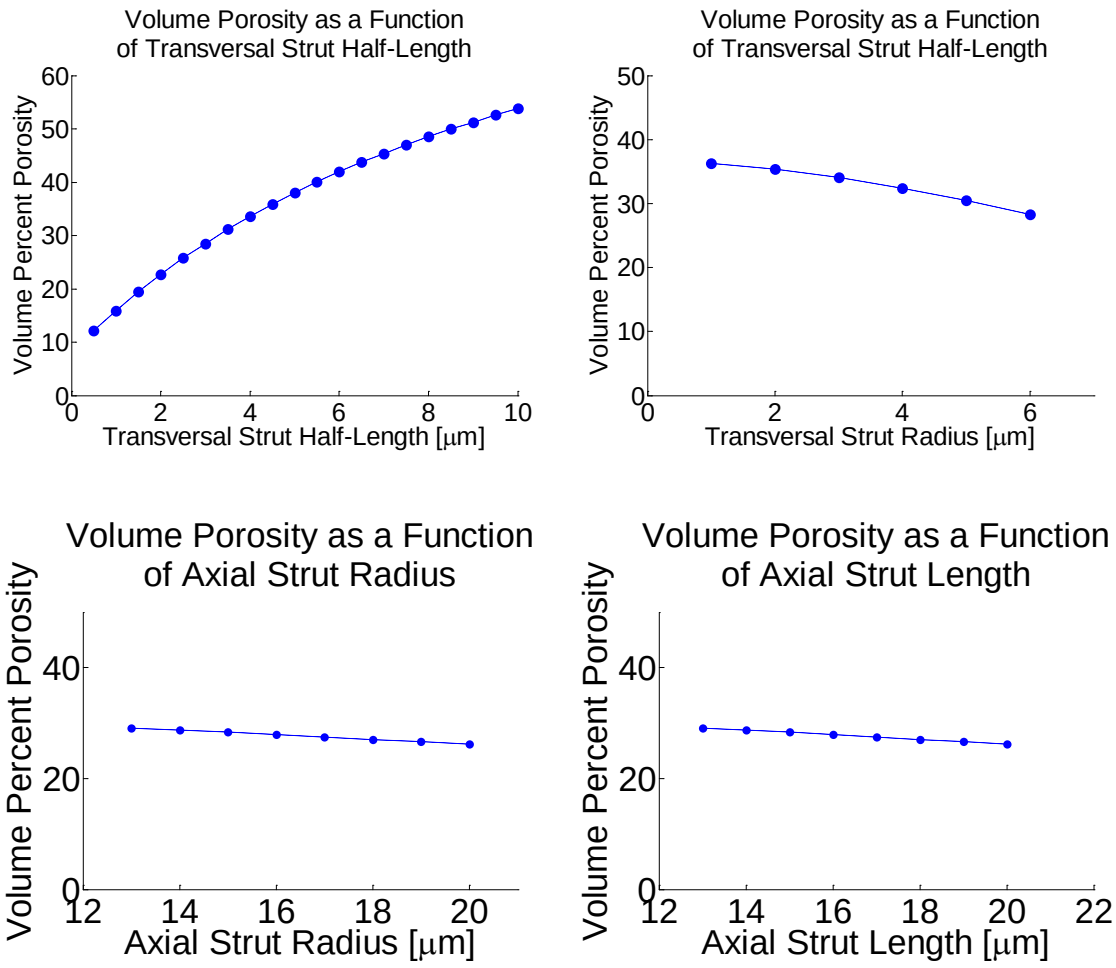


Figure 3-24: Variation in the volume porosity as a function of variation in each of the four feature parameters: TSR=Transversal Strut Radius, ASR=Axial Strut Radius, ASL=Axial Strut Length (related to transversal strut vertical spacing), and TSL= Transversal Strut Half-Length. The constant values for the parameters not varied in each case are: ASR = 15 μm, ASL = 24 μm, TSL = 3 μm, and TSR = 6 μm.

### 3.4 Summary of microstructural features

With the range of experimental methods performed on specimens of the *C. atratus,* both a descriptive set of micrographs and images as well as a series of quantitative results were obtained to fully characterize not only the detailed microstructure of the aboral spines that tile the urchin's body, but also how these armor units are arranged and articulated on an urchin. In

the following chapters of the thesis, many of these quantitative results aboral spine microstructure will be utilized as input into finite element simulations. Thus, in summary, the key microstructural features of the aboral spine microstructure are:

- Long, galleried structures that are directionally aligned extend from surface of the socket to the top/exterior surface of the aboral spine, causing anisotropy in the microstructure of the aboral spine.

- Due to a gradual change in the gallery feature dimensions and the spatial arrangement between the galleries, there exists a density gradient within the aboral spine. The region near the exterior/top surface is almost 30% more porous than the region near the socket.

- The repeating unit which makes up the galleried structure can be described by four main features: Transversal strut length and radius, transversal strut vertical spacing, and axial strut diameter (with values ranging from 5μm for the radius of a transversal strut to 35μm for the transversal strut vertical spacing). The variation in these parameters governs the local anisotropy in the microstructure as well as the porosity.

- From spatial analysis of an isolated galleried structure, the axial strut is continuous along the longitudinal length of the aboral spine, while sets of six struts transversely aligned, encircle the axial strut to connect to surrounding axial struts.

With quantitative detail of the aboral spine microstructure, a simplified model of a representative volume element (RVE) can be created to mimic the microstructure and its variations throughout the aboral spine. The simplification of the microstructure and the effect of the graded microstructure observed with SEM micrographs and microCT reconstructions will be discussed further in the following chapters.

# CHAPTER 4 Micromechanical Modeling of Gallery Structure Using Representative Volume Elements

Since attempting to simulate the entire three-dimensional spine with a finite element program would be computationally too expensive to be plausible, a multiscale simulation can be created by systematically simulating loading conditions on several idealized representative volume elements with periodic boundary conditions and then using the results as an input into a larger macroscale model. With a repeating unit volume isolated from the X-ray microtomography three-dimensional reconstruction, an idealized representative volume element (RVE) can be used to simulate the microstructure and obtain an effective elastic compliance tensor. By parametrically varying the idealized RVE, a range of elastic stiffness could be obtained and input into a macroscopic model of the entire aboral spine to simulate the entire unique microstructural arrangement of the aboral spine.

## 4.1 Construction of the RVE

In order to simulate the micromechanics of the aboral spine microstructure, the material properties of the solid (magnesium calcite) must first be determined as an input into the simulation. From literature of mechanical tests on calcite specimens, typically from other species of urchins, there is a large range in the modulus of echinoderm calcite due to the variety in the different species specimens themselves, the location of testing and the method used. The average modulus of the organic calcite is 70 GPa with a hardness of around 3 Mohrs (Vincent 2001), (Table 2-1). Because the actual Young's modulus of the solid organic calcite in the exoskeleton of *C. atratus* is not known, an isotropic of synthetic single-crystal calcite: Young's of 73.5 GPa

and shear modulus of 29.4 GPa, will be used in the simulations, while the results will be normalized by this value.

Considering the SEM micrographs, but more significantly, the microCT three-dimensional results, the proposed representative volume element (RVE) for the galleried structure is composed of an axial strut with six transversal struts equally spaced around the axial strut. As a parametric model, the RVE has four independent parameters that can be varied to change the geometry and consequently, the porosity of the RVE. The two types of struts are connected cylindrical rods with the axial strut radius (ASR), termed $R_1$, and the transversal strut radius (TSR), identified as $R_2$. The axial strut length (ASL), $L_1$, determines the vertical spacing between the transversal struts while the transversal strut half-length (TSL), $L_2$, is the same for all 6 struts surrounding the axial strut and determines the distance between the axial struts (Figure 4-1). These are the same four parameters measured from the microCT scans in the previous chapter. To avoid intersection of the transversal struts at the base of their connection to the axial strut, the range of the axial strut radius is limited to be large enough to have six struts surrounding its perimeter. To mimic the curved surface of the connection between the transversal struts and the axial strut, fillets were implemented on the connecting edge. To determine the significance of the fillet, the variation in the radius of the fillet is also possible in the parametric model, though it does not significantly change the porosity of the RVE.

With the established parametric model, regions of the actual aboral spine and the volume porosity at that specific region can be modeled by setting the four feature parameters to match the microstructure at that location in the aboral spine. Figure 4-2, shows three examples of representative volume elements that model the microstructure at the indicated location within the cross-section slice of the aboral spine sample “b1s2”. Table 4-1 lists the RVE parameters used to

generate the volumes shown and Figure 4-3 shows the top view and perspective views of the tessellations of the three RVE in three-dimensional space, which show more clearly how the volume porosity is greater near the top of the aboral spine (RVE A) even though the axial strut radius is larger. The slight increase in transversal strut length greatly increases the pore size between the RVEs, as discussed in section 3.2 (Figure 3-24).

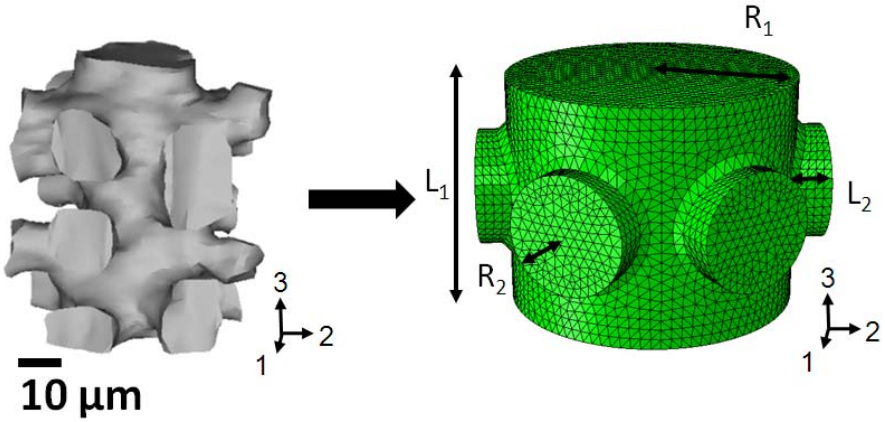


Figure 4-1: Idealized representative volume element with the four parametric variables assigned. RVE of volume porosity 24% shown ($L_1$=24 µm, $L_2$=3 µm, $R_1$=15 µm, $R_2$=6 µm)

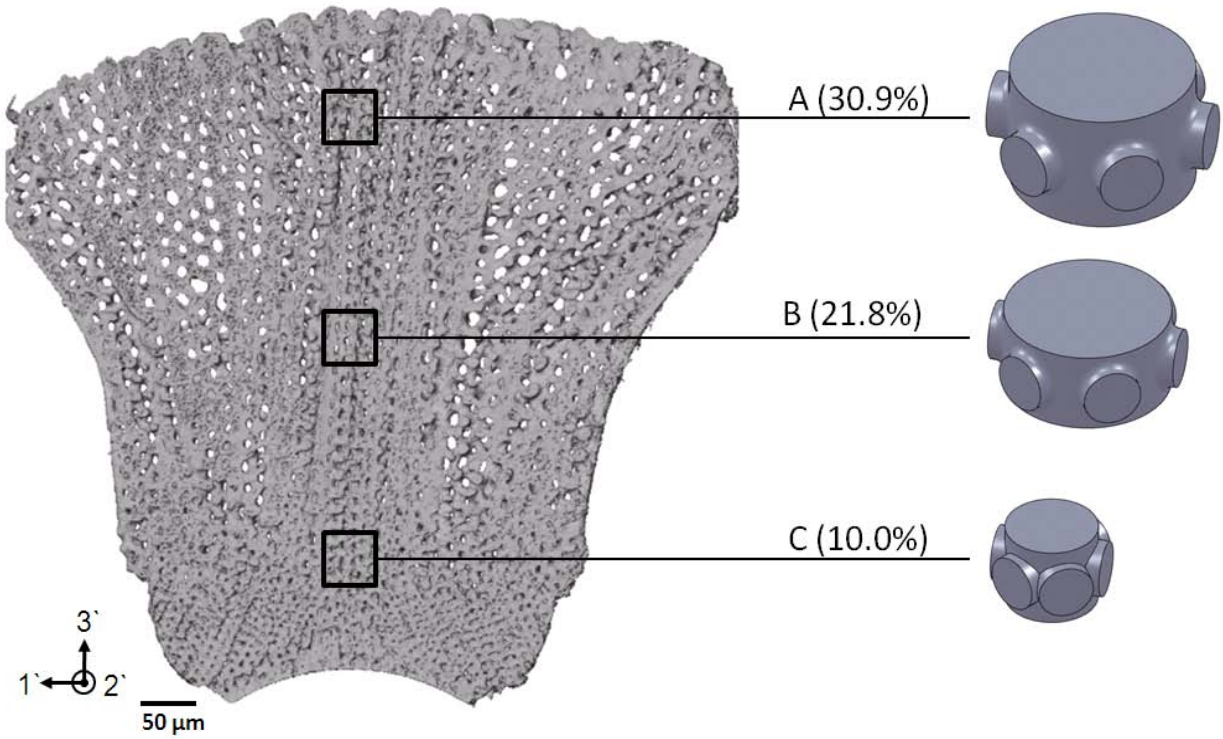


Figure 4-2: Three examples of idealized representative volume element using feature parameters found in sample "b1s2" (Chapter 3) with volume porosities indicated. (**A**) RVE near socket joint, (**B**) RVE from middle region, (**C**) RVE near top/exterior surface.

Table 4-1: Parameters, volume fraction and porosity of the three RVE shown in Figure 4-2

| | **Position** | **TSR (µm)** | **ASR (µm)** | **TSVS (µm)** | **TSL (µm)** | **Volume Fraction** | **Volume Porosity** |
|---|---|---|---|---|---|---|---|
| A | Top | 7 | 15 | 27 | 8 | 0.69 | 30.9% |
| B | Middle | 6.5 | 18 | 18 | 5 | 0.78 | 21.8% |
| C | Bottom | 6 | 10 | 18 | 4 | 0.90 | 10.0% |

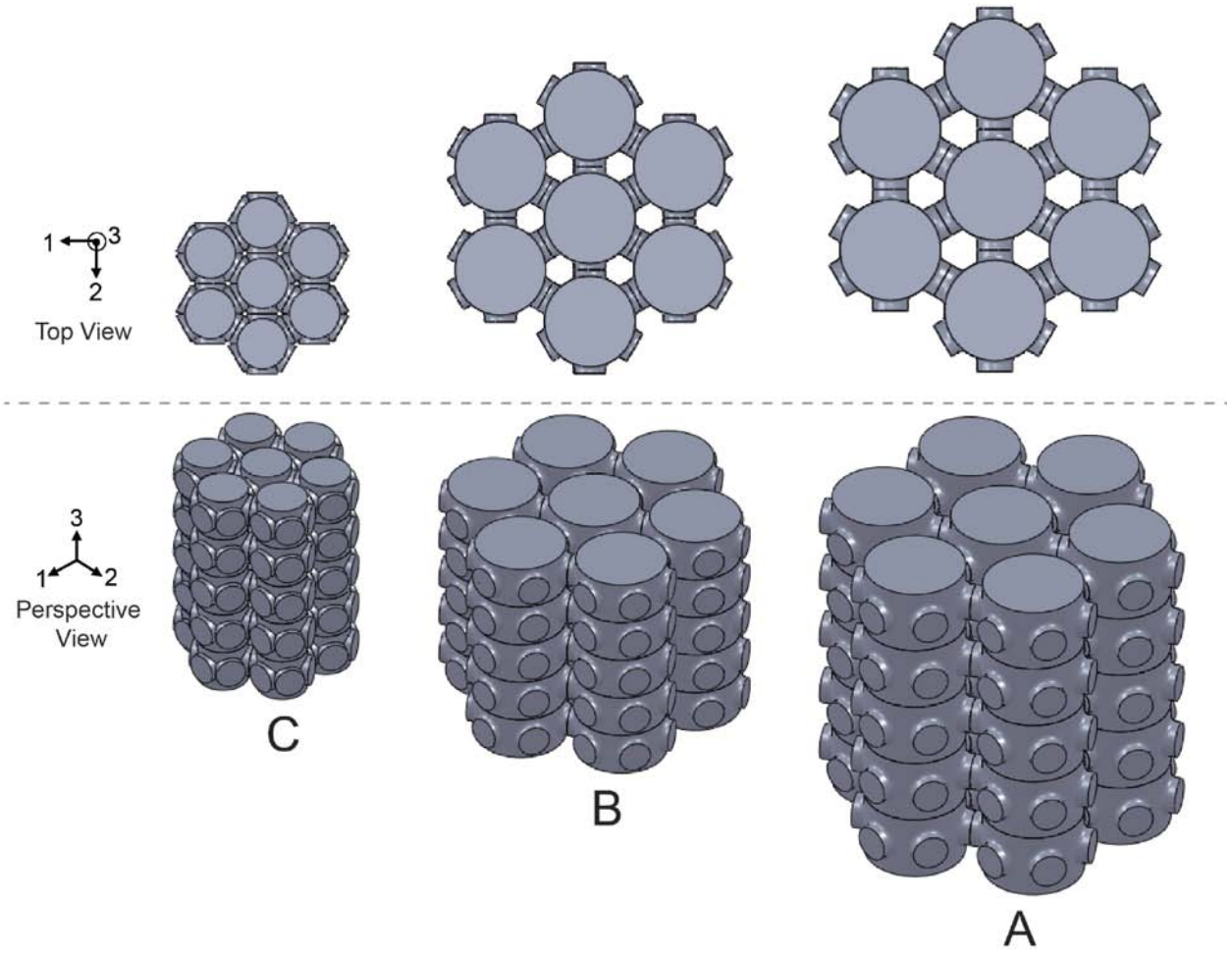


Figure 4-3: Top views and perspective views of tessellation of idealized representative volume elements: A, B and C shown in Figure 4-2. (Parameter values listed in Table 4-1)

The bounding volume of the RVE is simply the circumscribed hexagonal prism. The exact volume fraction for each RVE can be determined by ABAQUS, but an approximate volume fraction equation can also be easily calculated by neglecting volume effects at filleted edge between transversal struts and the axial strut:

$$Volume\ Fraction\ (R_1, R_2, L_1, L_2) \cong \frac{\pi R_1^2 L_1 + 6\pi R_2^2 L_2}{\sqrt{3}(R_1 + L_2)^2 L_1} \tag{4.1}$$

### 4.3 Periodic Boundary Conditions

To simulate an infinite arrangement of the representative volume elements, periodic boundary conditions are applied to the connecting faces of the RVE. This includes the top and bottom surfaces of the axial strut and the six faces of the transversal struts. Because the boundary conditions apply to pairs of nodes on opposite faces, the same number and position of nodes must be on the corresponding opposite side. The labels AA1, AA2, etc refer to opposite boundary node sets to be tied by the periodic boundary conditions. AA1 is associated with AA2, ZZ1 associated with ZZ2, and so on. As a result, the volumes are meshed to ensure opposite surfaces have corresponding nodes to satisfy the periodic boundary conditions.

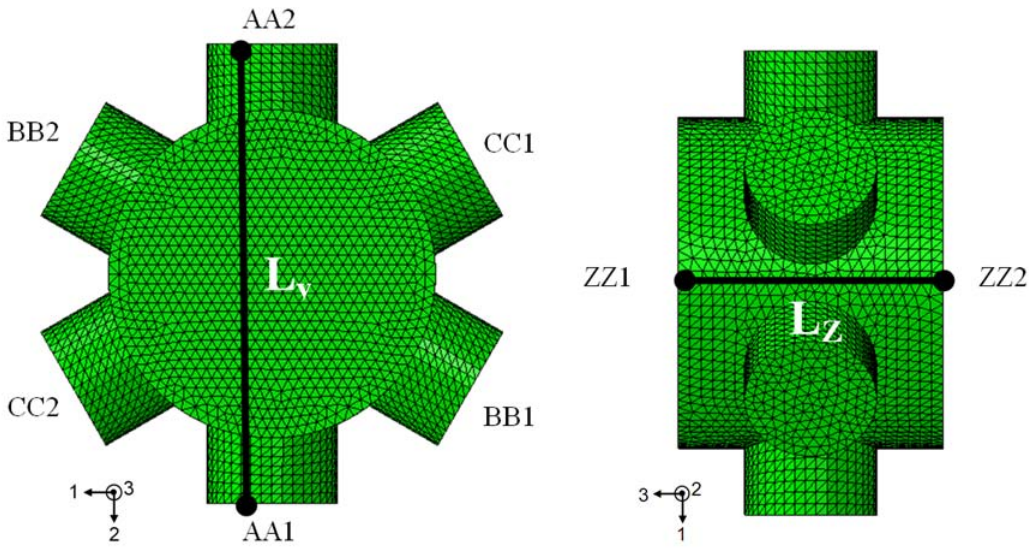


Figure 4-4: Boundary node sets and reference lengths of representative volume elements. Ly and Lz refer to the reference distance between the indicated boundary node sets.

Periodic boundary conditions are implemented by tying the motion of each boundary node A to that of the corresponding boundary node B:

$$\boldsymbol{u}(B) - \boldsymbol{u}(A) = \boldsymbol{H}[\boldsymbol{X}(B) - \boldsymbol{X}(A)] \tag{4.2}$$

where A and B are node sets of connecting sides, **u** is the displacement vector of the node set, **H** is the macroscopic displacement gradient applied to the material and **X** is the reference position vector of the node set. The displacement vector, **u**, is not the same for all nodes on a given surface. Deformations are performed via a specified macroscopic displacement gradient, **H**, which is related to the macroscopic deformation gradient, **F**, by:

$$\mathbf{H} = (\mathbf{F} - \mathbf{1}) \tag{4.3}$$

where the macroscopic deformation gradient is defined by:

$$\boldsymbol{F} = \boldsymbol{I} + \frac{\partial \boldsymbol{u}}{\partial \boldsymbol{X}} = \begin{pmatrix} F_{11} & F_{12} & F_{13} \\ F_{21} & F_{22} & F_{23} \\ F_{31} & F_{32} & F_{33} \end{pmatrix} \tag{4.4}$$

where X is the position vector of the reference configuration and **u** is displacement vector.

In ABAQUS, the macroscopic displacement gradient is applied through 3 virtual nodes: N1, N2, and N3; where displacing node N1 in the 1-direction, $u_1$(N1), assigns the value of **H**(1,1), displacing the node N2 in the 2-direction, $u_2$(N2), assigns the value of **H**(2,2), and so on:

$$\boldsymbol{H} = \begin{pmatrix} u_1(N1) & u_2(N1) & u_3(N1) \\ u_1(N2) & u_2(N2) & u_3(N2) \\ u_1(N3) & u_2(N3) & u_3(N3) \end{pmatrix} \tag{4.5}$$

Using the principal of virtual work, the overall mechanical response of the representative volume element can be determined. The components of the macroscopic first Piola-Kirchhoff

stress tensor, **S**, can be derived in terms of the generalized reaction forces of the three virtual nodes (Danielsson et. al. 2002):

$$\boldsymbol{S} = \frac{1}{Vo}\begin{pmatrix} \Xi_1(N1) & \Xi_2(N1) & \Xi_3(N1) \\ \Xi_1(N2) & \Xi_2(N2) & \Xi_3(N2) \\ \Xi_1(N3) & \Xi_2(N3) & \Xi_3(N3) \end{pmatrix} \tag{4.5}$$

where $V_o$ is the original volume of the RVE, in this case, a hexagonal prism circumscribing the represented structure. Additionally, from the first Piola-Kirchhoff stress tensor, a macroscopic Cauchy stress tensor, **T**, can be calculated as:

$$\boldsymbol{T} = \frac{1}{J}\boldsymbol{S}\boldsymbol{F}^{\boldsymbol{T}} \tag{4.6}$$

where J=det(**F**).

### 4.4 RVE Loading and Determination of Effective Elastic Moduli

To obtain the elastic mechanical behavior and the elastic moduli of the RVE, six different loading conditions are imposed on the RVE. For uniaxial tension in the **1 direction**, the deformation gradient will be:

$$H_{11} = \varepsilon^*$$

$$H_{12} = H_{21} = H_{13} = H_{31} = H_{32} = H_{23} = 0 \qquad \boldsymbol{H} = \begin{pmatrix} \varepsilon^* & 0 & 0 \\ 0 & - & 0 \\ 0 & 0 & - \end{pmatrix}$$

$$H_{22}\ and\ H_{33}\ are\ not\ constrained.$$

For uniaxial tension in the **2 direction**, the deformation gradient will be:

$$H_{22} = \varepsilon^*$$

$$H_{12} = H_{21} = H_{13} = H_{31} = H_{32} = H_{23} = 0 \qquad \boldsymbol{H} = \begin{pmatrix} - & 0 & 0 \\ 0 & \varepsilon^* & 0 \\ 0 & 0 & - \end{pmatrix}$$

$$H_{11}\ and\ H_{33}\ are\ not\ constrained.$$

For uniaxial tension in the **3 direction**, the deformation gradient will be:

$$H_{33} = \varepsilon^*$$

$$H_{12} = H_{21} = H_{13} = H_{31} = H_{32} = H_{23} = 0$$

$$H_{11} \text{ and } H_{22} \text{ are not constrained.}$$

$$\boldsymbol{H} = \begin{pmatrix} - & 0 & 0 \\ 0 & - & 0 \\ 0 & 0 & \varepsilon^* \end{pmatrix}$$

For simple shear on the surface with normal in the 2 direction:

$$\boldsymbol{H} = \begin{pmatrix} 0 & \gamma & 0 \\ 0 & 0 & 0 \\ 0 & 0 & 0 \end{pmatrix}$$

For simple shear on the surface with normal in the 1 direction:

$$\boldsymbol{H} = \begin{pmatrix} 0 & 0 & 0 \\ 0 & 0 & \gamma \\ 0 & 0 & 0 \end{pmatrix}$$

For simple shear on the surface with normal in the 3 direction:

$$\boldsymbol{H} = \begin{pmatrix} 0 & 0 & \gamma \\ 0 & 0 & 0 \\ 0 & 0 & 0 \end{pmatrix}$$

By plotting the stress and strain curves, the elastic moduli resulting from strains in different directions can be found ($E_1$, $E_2$, $E_3$) as well as the three shear moduli ($G_{23}$, $G_{13}$, $G_{12}$).

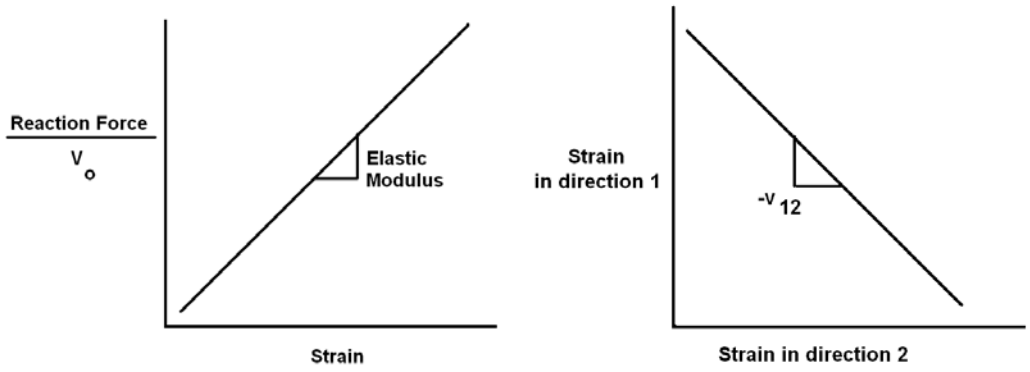


Figure 4-5: Determination of the elastic moduli and Poisson's ratios.

The Poisson's ratio can be obtained by calculating the amount of contraction in the other two directions for uniaxial tension. The slope in the plot of the strain in the other direction against the strain in the uniaxial tension direction will result in the Poisson's ratio.

From the characterization of the microstructure in the previous chapter, the microstructure can be described by a fourth order orthotropic elastic tensor, with the three mutually perpendicular symmetry planes. This reduces the number of constants to 9 independent material constants: $E_1$, $E_2$, $E_3$, $G_{23}$, $G_{13}$, $G_{12,}$ $\nu_{21}$, $\nu_{31}$, and $\nu_{23}$. The constants $\nu_{12}$, $\nu_{13}$, and $\nu_{32}$ can be found from the relation:

$$\frac{\nu_{ij}}{E_i} = \frac{\nu_{ji}}{E_j} \tag{4.7}$$

By straining the volume in 6 different directions, the orthotropic compliance tensor can be found:

$$S_{orthotropic} = \begin{pmatrix} \frac{1}{E_1} & -\frac{v_{21}}{E_2} & -\frac{v_{31}}{E_3} & 0 & 0 & 0 \\ -\frac{v_{12}}{E_1} & \frac{1}{E_2} & -\frac{v_{32}}{E_3} & 0 & 0 & 0 \\ -\frac{v_{13}}{E_1} & -\frac{v_{23}}{E_2} & \frac{1}{E_3} & 0 & 0 & 0 \\ 0 & 0 & 0 & \frac{1}{G_{23}} & 0 & 0 \\ 0 & 0 & 0 & 0 & \frac{1}{G_{13}} & 0 \\ 0 & 0 & 0 & 0 & 0 & \frac{1}{G_{12}} \end{pmatrix}$$

Because the representative volume used in the simulation has the additional six-fold symmetry (the six transversal struts are identical), the RVE is actually transversely isotropic. The material is isotropic in the 1-2 plane (symmetry plane p) but anisotropic in the 3 direction (perpendicular to the symmetry plane). This reduces the number of independent elastic constants to just five: $E_p$, $E_t$, $\nu_p$, $\nu_{pt}$, and $G_t$, such that the compliance tensor has the form:

$$S_{transversely\ isotropic} = \begin{pmatrix} \frac{1}{E_p} & -\frac{v_p}{E_p} & -\frac{v_{tp}}{E_t} & 0 & 0 & 0 \\ -\frac{v_p}{E_p} & \frac{1}{E_p} & -\frac{v_{tp}}{E_t} & 0 & 0 & 0 \\ -\frac{v_{pt}}{E_p} & -\frac{v_{pt}}{E_p} & \frac{1}{E_t} & 0 & 0 & 0 \\ 0 & 0 & 0 & \frac{1}{G_t} & 0 & 0 \\ 0 & 0 & 0 & 0 & \frac{1}{G_t} & 0 \\ 0 & 0 & 0 & 0 & 0 & \frac{1}{G_p} \end{pmatrix}$$

The constants must satisfy the following relations:

$$E_1 = E_2 = E_p, E_3 = E_t \tag{4.8}$$

$$\nu_{21} = \nu_{12} = \nu_{\mathrm{p}}, \nu_{31} = \nu_{32} = \nu_{\mathrm{tp}}, \nu_{23} = \nu_{13} = \nu_{\mathrm{pt}} \tag{4.9}$$

$$G_p = \frac{E_p}{2(1+\nu_p)}, \frac{\nu_{\mathbf{tp}}}{\mathbf{E_t}} = \frac{\nu_{\mathbf{pt}}}{\mathbf{E_p}} \tag{4.10}$$

## 4.4 RVE Parameterization

Prior to parametric variations of the RVE geometry, the optimum mesh for accurate finite element results was determined by a mesh convergence study. For the average RVE shape features (TSR = 6.0 μm, ASR = 15 μm, TSL = 3.0 μm, and ASL=24 μm), only the mesh size was varied from a very coarse mesh to a very fine mesh. The results were plotted as a function of the number of nodes to determine the largest mesh size sufficient to provide accurate results (Figure 4-6). From the simulations, the the mesh size had only a slight effect on the resulting elastic constants. Thus, a mesh size of 1.0 microns was chosen as an appropriate mesh density in the rest of the simulations.

For the following plots, the relative moduli represent the actual moduli divided by that of isotropic solid calcite material property used in the simulation: Young's modulus of 73.5 GPa, shear modulus of 29.4 GPa, and Poisson's ratio of 0.25.

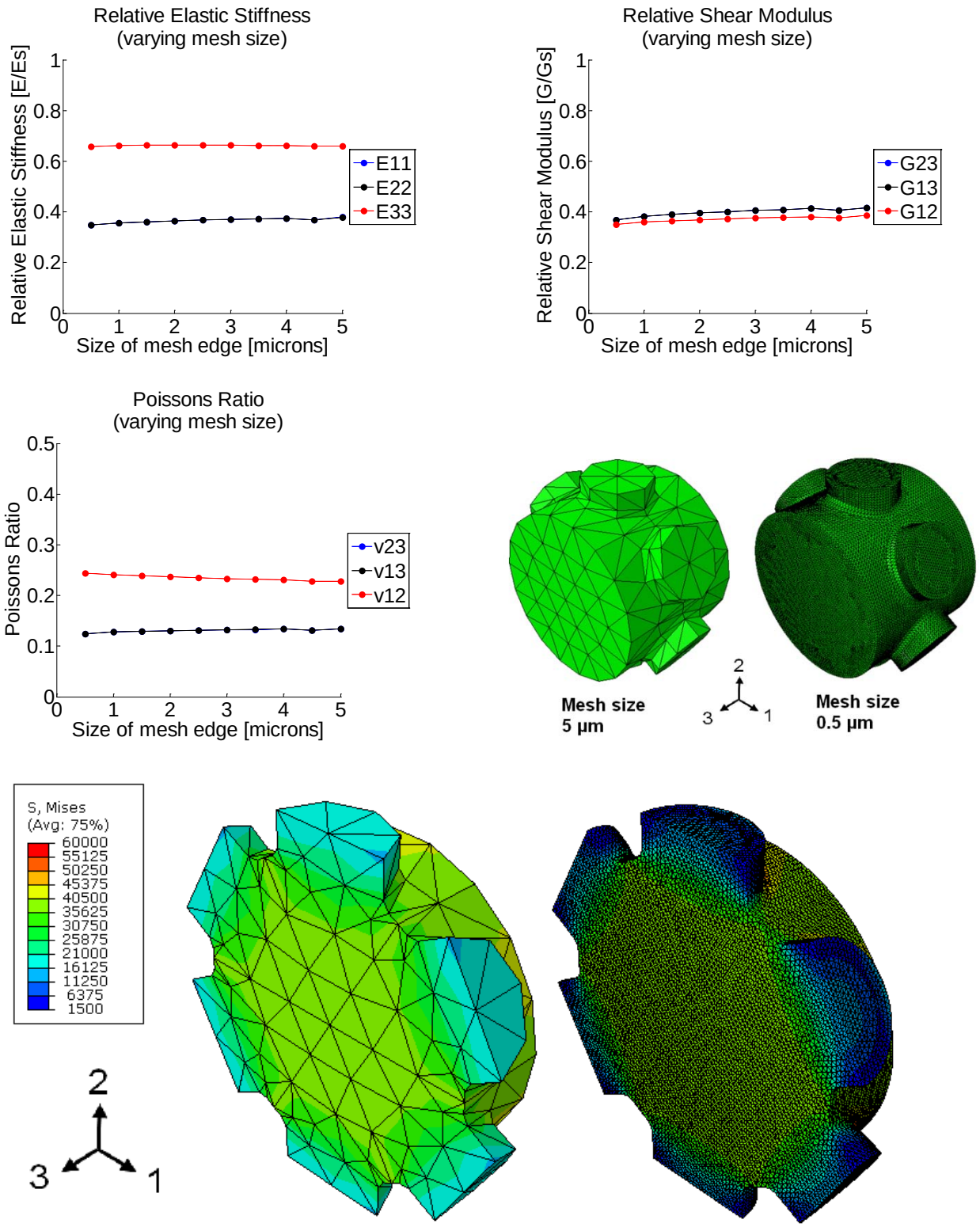


Figure 4-6: Mesh convergence of RVE simulation. Mises stress for compressive loading in the 3-direciton to a strain of 0.05. (TSR = 6.0 µm, ASR = 15 µm, TSL = 3.0 µm, and ASL=24 µm).

After determining an appropriate mesh size for the RVE, the fillet radius of the transversal strut was varied to determine if the fillet was a significant factor in the mechanical properties of the RVE. Then, for the four geometric parameters (axial strut radius, axial strut length, transversal strut radius, and transversal strut half-length), one of the four parameters was varied while the other three parameters were held constant.

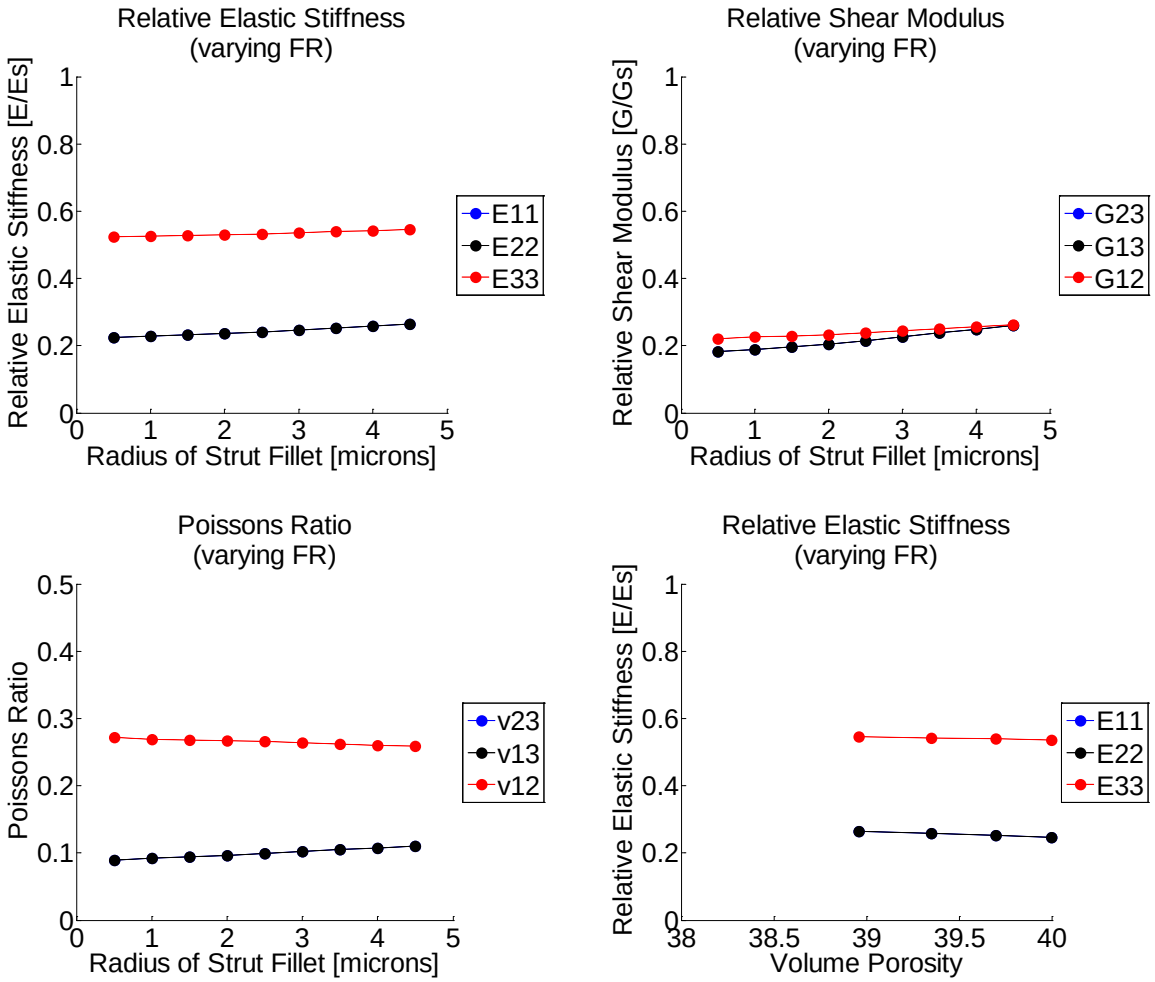


Figure 4-7: Effect of variation of fillet radius on moduli and Poisson's ratio.

By varying the fillet size on the edge that connects the transversal struts to the main axial strut, the large stress concentration of that fillet edge transfers from the fillet to the edges of the

axial strut. Although change in fillet radius from 0.5 microns to 4.5 microns (a factor of 5 increase) creates a noticeable change in the stress distribution within the structure, it is only a 2% change in the volume fraction between the two RVEs. Comparing the actual stiffness values, in Figure 4-7, there is slight increase of axial stiffness as a function of fillet radius but a more noticeable increase in shear stiffness, due to the strengthening of the transversal strut base by the fillet.

This effect is best seen in the stress and strain contours resulting from both axial loading (3 direction) and shear loading (2-3 direction). With axial loading in the 3 direction, the base of the transversal strut experiences the highest stress and compressive axial strain in the smaller fillet case, while the boundary edge of the axial strut carries the axial load and compressive axial strain with the larger fillet (Figure 4-11 and 4-12). Comparing the shear strain contours between the two fillet size extremes in axial loading shows the direct relation between the fillet size and concentration of stress at the base of the transversal strut (Figure 4-13). From the Mises stress of a shear loading case in the 2-3 direction (Figures 4-14), it can be seen that the larger fillet also distributes the shear stress at the base of the transversal struts, transferring a small portion of the load to the axial strut while in the smaller fillet, the higher loads are more concentrated at the base of the transversal strut. The axial and shear strains of the shear loading reveals the axial strain in the 3 direction is concentrated at the base of the struts, while the shear strain is distributed by the fillet at the base of the strut to the axial strut, with the larger fillet being more effective (Figure 4-15 and 4-16).

From the micrographs discussed in chapter 3, the fillet radii can be approximated from the radii of the pores, which range from 3.0 μm to 5.0 μm (Figures 3-3 and 3-5). Yet, for the following simulations, a fillet radius of 1.0μm was used in order to prevent intersection of the

transversal struts when attempting to vary the other four parameters in the RVE model through a sufficient range of values.

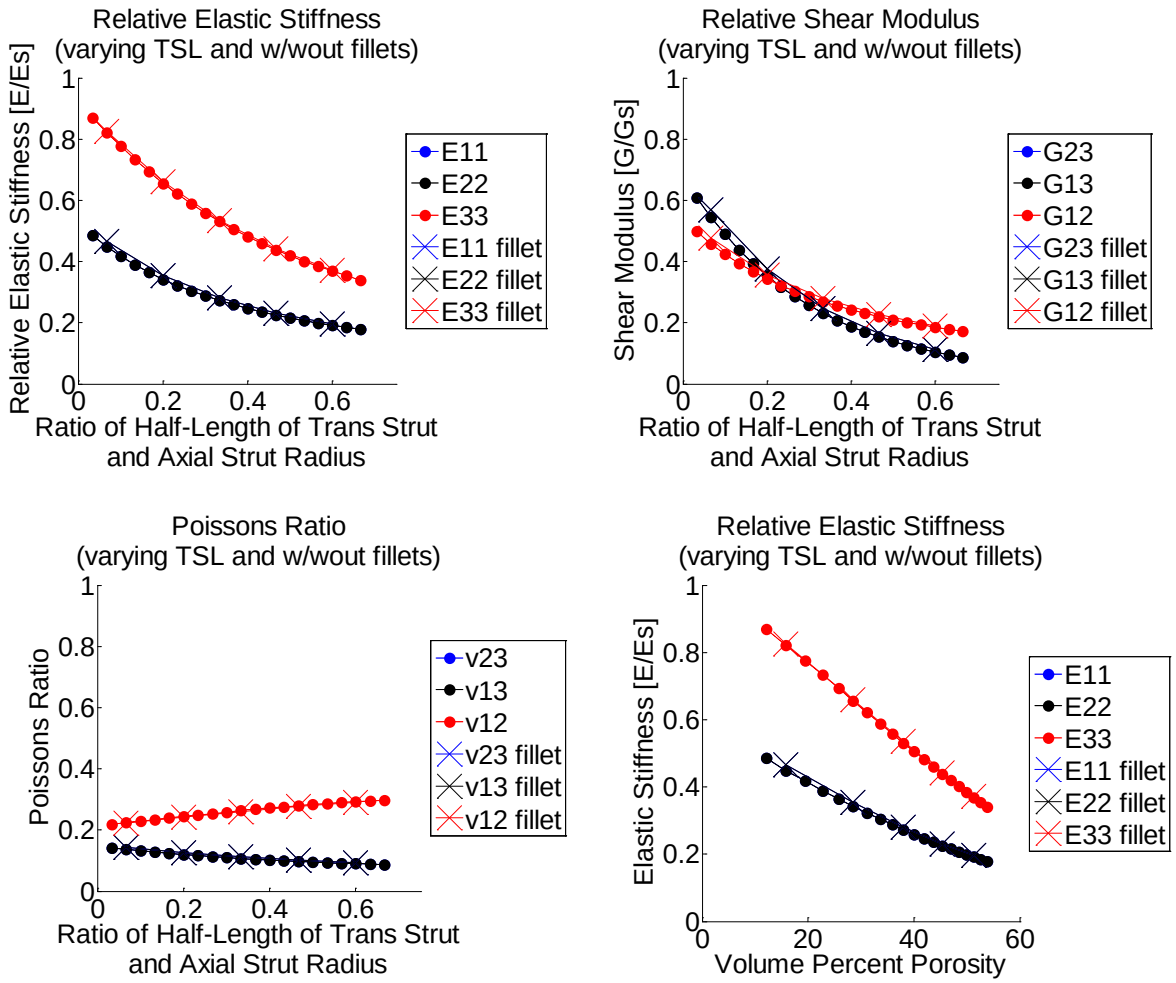


Figure 4-8: Effect of variation of transversal strut half-length on moduli and Poisson's ratio. Transversal strut length found to range from 2.34μm to 11.88μm (half-length ranges from 1.17μm to 5.94μm) in microCT measurements.

The variation in transversal strut half-length from 2 microns to 20 microns increases the volume percent from 12% to 53% porous (Figure 4-8). While relative axial stiffness decreases by a factor of 2.7 as the volume porosity increases, the relative shear moduli decreases linearly by a factor of 7.5 within the same range. At around 30% volume porosity, the three shear moduli are

approximately equal. Note that this porosity corresponds to the average porosity of the actual spine microstructure found in Chapter 3. With the same set of RVE dimensions, a small, 1 micron radius fillet was applied to the RVEs and its effects were also plotted in Figure 4-8. As expected from the previous simulations of varying the fillet radius, the small fillet slightly increases the results for the moduli and Poisson's ratio.

From the contour plots, the effect of the longer transversal strut can be seen in the higher stress concentration at the base of the transversal strut during loading in the axial 3-direction (Figure 4-11). Although the longer strut carries lower stresses, there is a higher stress state at the base of the strut, where the fillet would be. The localization of the stress state in the shorter transversal strut case is accompanied by the higher compressive axial strains and shear strains at the base of the short struts (Figure 4-12 and 4-13). Note that the axial strut is insensitive to the axial loading since the stress and strain contours in the axial strut remain similar in both strut cases. From the shear loading in the 2-3 direction, the shorter transversal strut distributes more of the stress to the axial strut but by having higher axial strains at the base of the transversal strut results in the axial strut having more sensitivity to the shear stress and strains in the transversal strut (Figure 4-14 and 4-15). Figure 4-16, of the shear strain during shear loading, captures the strain localization effect of the longer transversal strut, where the shorter transversal strut is able to transfer the shear strains more effectively to the axial strut.

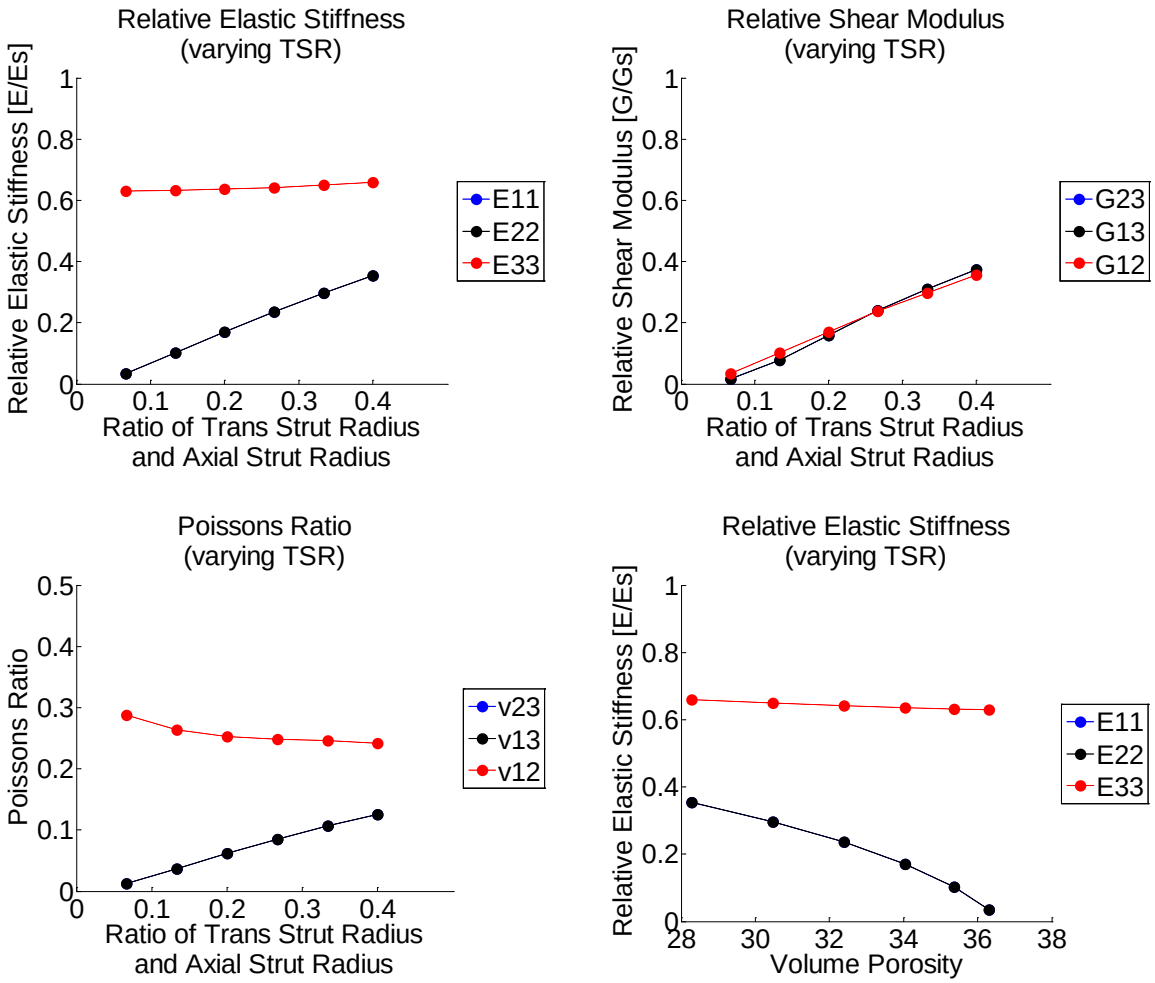


Figure 4-9: Effect of variation of transversal strut radius on moduli and Poisson's ratio. Transversal strut radius found to range from 4.74µm to 9.95µm in microCT measurements.

Since, by increasing the radius of the transversal strut, the ratio of transversal strut radius over the axial strut radius increases, the effect of relative strut radius of the axial and transversal struts can also be observed with this variation. While the relative stiffness in the axial direction is insensitive to changes in the transversal strut radius, the stiffness in the plane of the transversal strut decreases to nearly zero as the radius decreases to 1.0 micron (Figure 4-9). The three shear

moduli increases linearly with the transversal strut radius. Most of the axial load is carried by axial strut so the response to shear stresses and transversal stresses is directly dependent on the geometry of the transversal struts. As the transversal struts increase in radius, more of the load carried by the axial strut is transferred to the transversal struts, thereby increasing the stress concentration on the attachment edge at the base of the transversal struts.

This is most apparent in the stress and strain contours resulting from shear loading in the 2-3 direction (Figure 4-14, 4-15 and 4-16). When the transversal strut radius is much smaller than the axial strut radius, most of the shear stress and shear strains are localized in the transversal strut while the axial strains, which are localized at the base of the transversal strut, are more highly concentrated in the larger strut case. When loaded axially, the RVE with the larger transversal strut has slightly higher axial compressive strains in the axial strut and a larger area of concentrated axial and shear strains at the base of the transversal strut (Figure 4-12 and 4-13). But with a more even ratio in the radii of the transversal and axial struts, the axial strut begins to carry more of the load on the structure and the deformations as well.

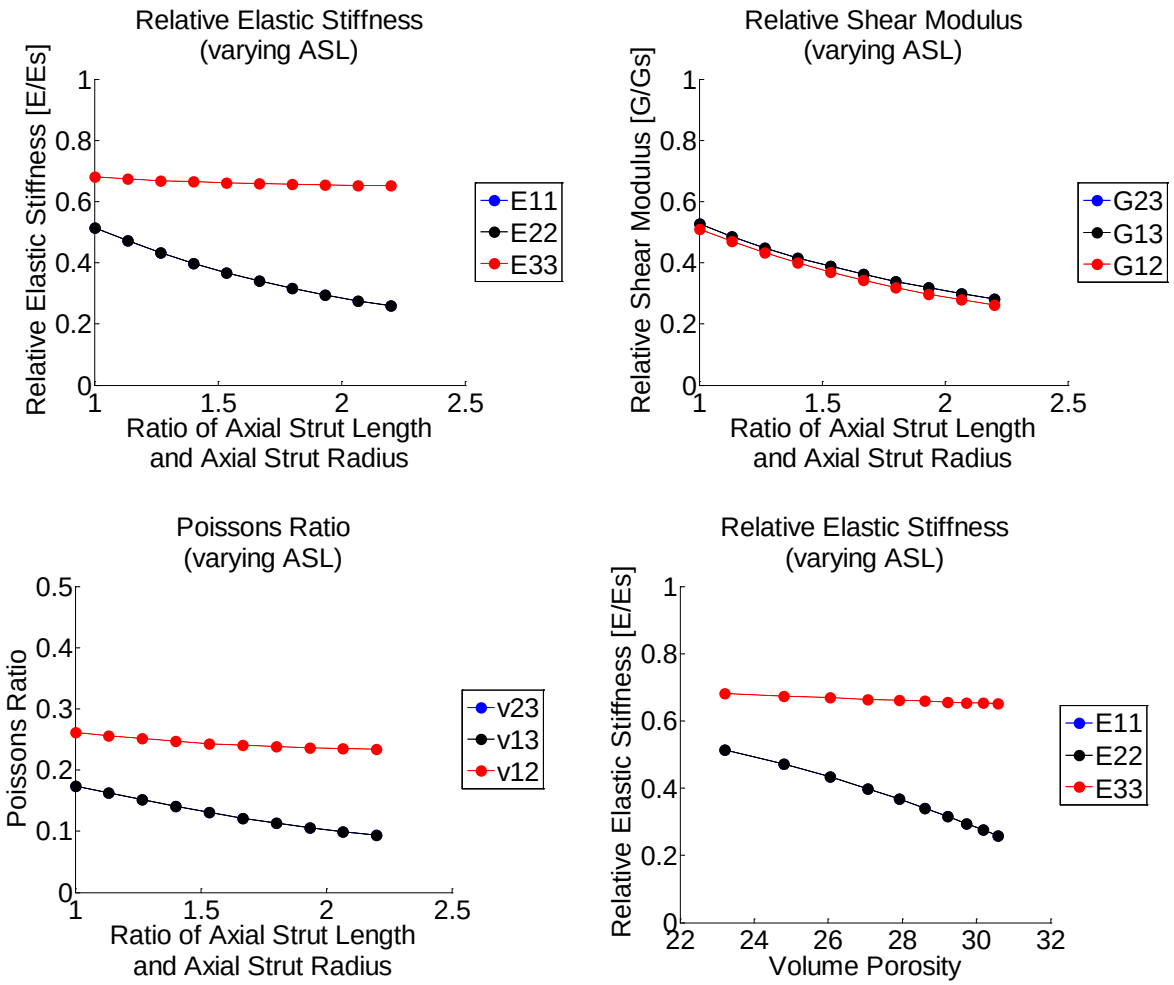


Figure 4-10: Effect of variation of axial strut length on moduli and Poisson's ratio. Axial strut length found to range from 12.84μm to 35.5μm in microCT measurements.

Through variation of the axial strut length of the RVE, the vertical center-to-center distance between the transversal strut is varied. Although the axial stiffness in the 3-direction is not affected by this length, the shear moduli and axial stiffness in the in-plane directions 2 and 3 decrease with increasing axial strut length (Figure 4-10). From the contour plots of the Mises stress resulting from loading in the axial 3-direction, the decrease in shear stiffness and in-plane stiffness can be attributed to the distance between the transversal struts (Figure 4-11). With a smaller axial strut length, the high stress concentration at the base of the transversal strut is magnified by its proximity to the other transversal strut above and below it along the 3-direction.

This is observed also in the axial strains from the compressive axial loading, where the axial compressive strains are highest are the axial strut edges for the smaller axial strut length (Figure 4-12). In the RVE with the longer axial strut, this concentration is not observed; rather, the high compressive axial strain is concentrated at the base of the transversal strut. Figure 4-13, of the shear strain under axial loading, reveals a similar distribution of shear strains in both RVEs, while the axial strut exhibits very little shear strain. This effect of the proximity between the transversal struts can also be seen from the shear loading in the 2-3 direction (Figure 4-14 and Figure 4-16). At the circular edge in the axial strut of the RVE is essentially the midpoint between transversal struts in the 3 direction because of periodic boundary conditions. Comparing the stresses and shear strains at that circular edge, the RVE with the larger axial strut length, or larger transversal strut spacing along the 3 direction, has much lower stress state between the transversal struts and higher shear strains in the axial strut. The axial strain under shear loading is concentrated at the base of transversal struts, higher in the RVE with larger axial strut length.

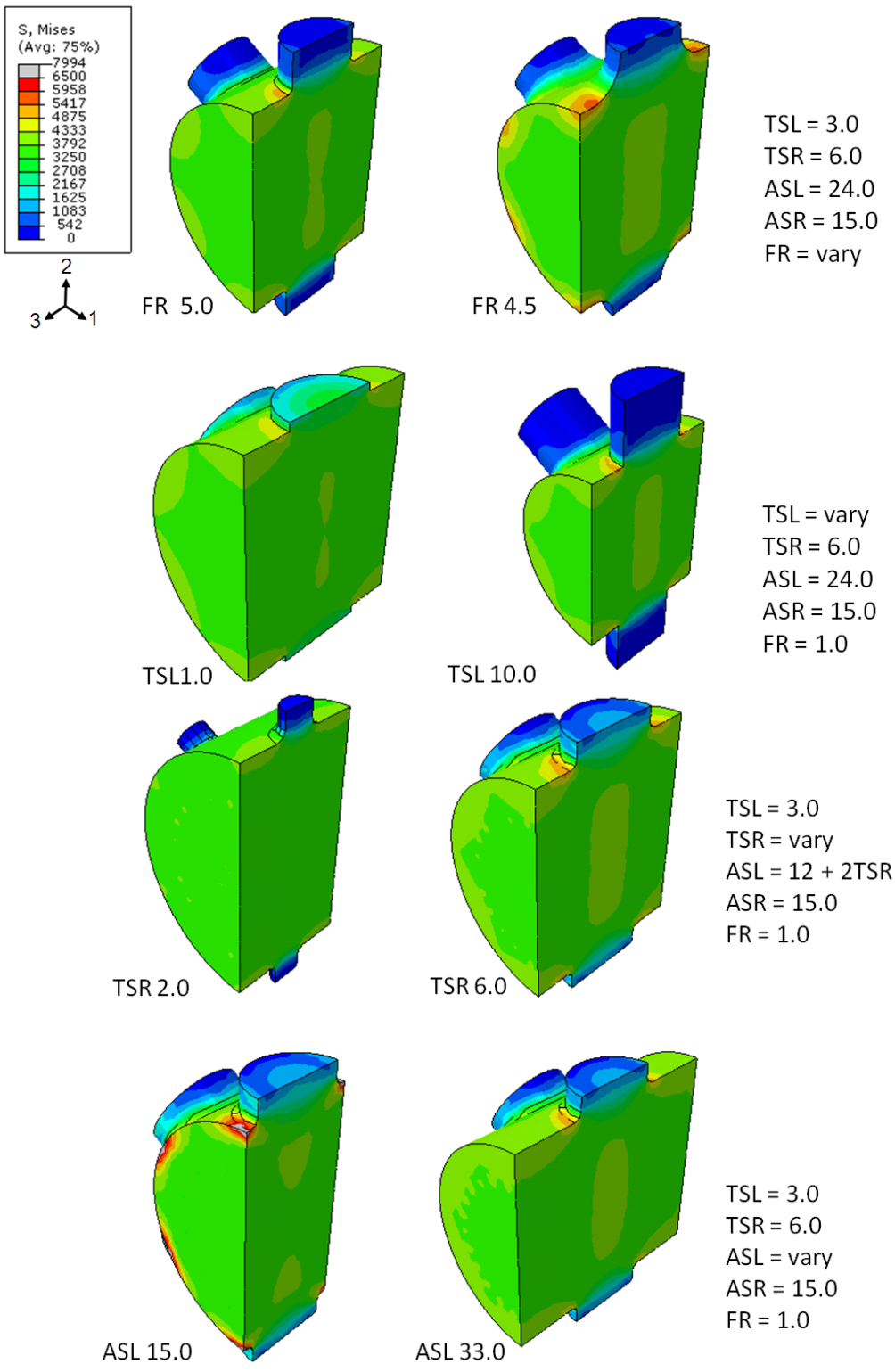


Figure 4-11: Mises contours (with a cross-sectional cut view) resulting from compressive loading in the 3-direction to a strain of 0.05, comparing the extremes in the variation of each of four parameters in the RVEs (fillet radius (FR), transversal strut half-length (TSL), transversal strut radius (TSR), and axial strut length (ASL)).

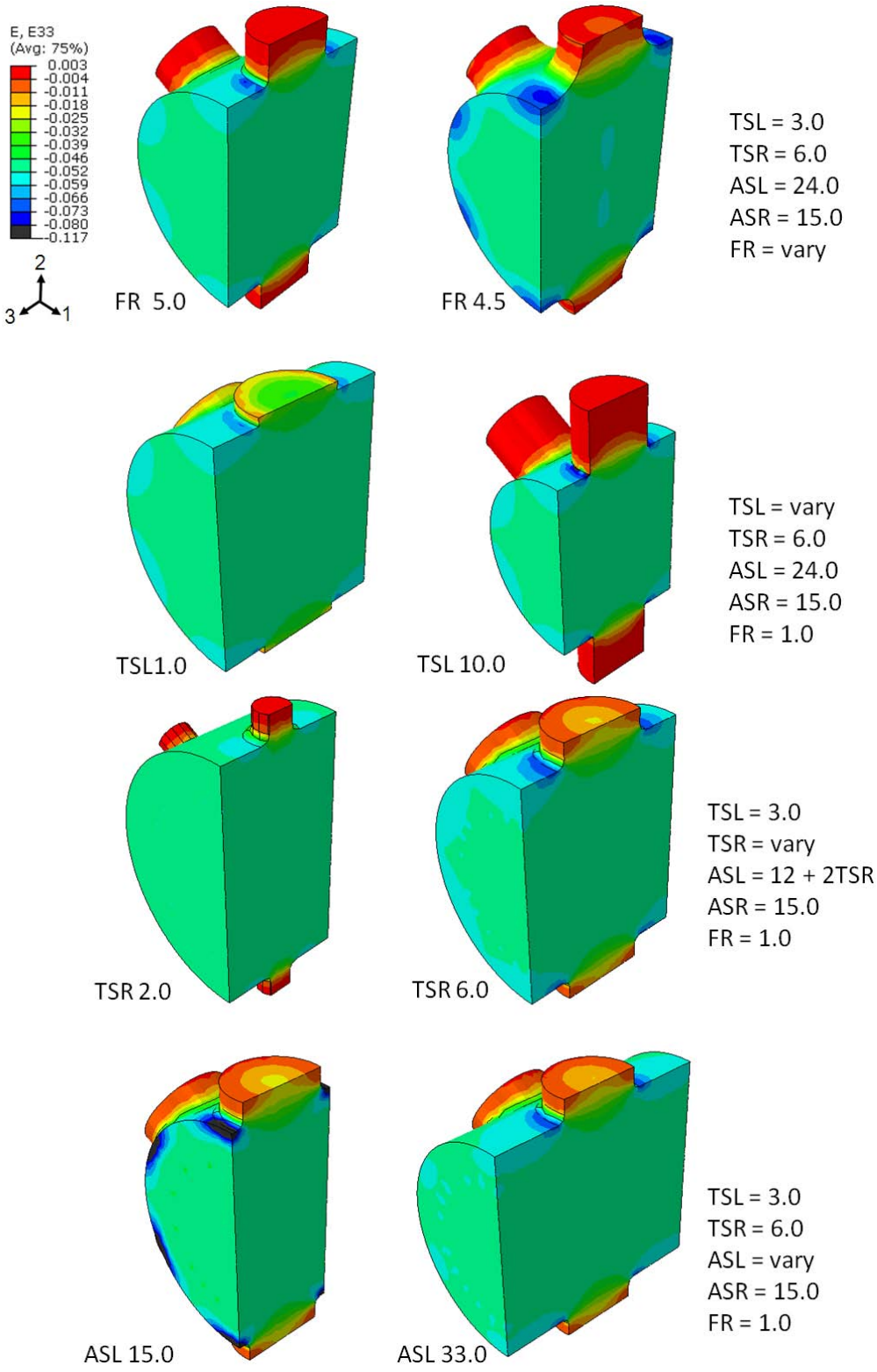


Figure 4-12: Axial strain, $\varepsilon_{33}$, contours (with a cross-sectional cut view) resulting from compressive loading in the 3-direction to a strain of 0.05, comparing the extremes in the variation of each of four parameters in the RVEs, same RVEs as Figure 4-9.

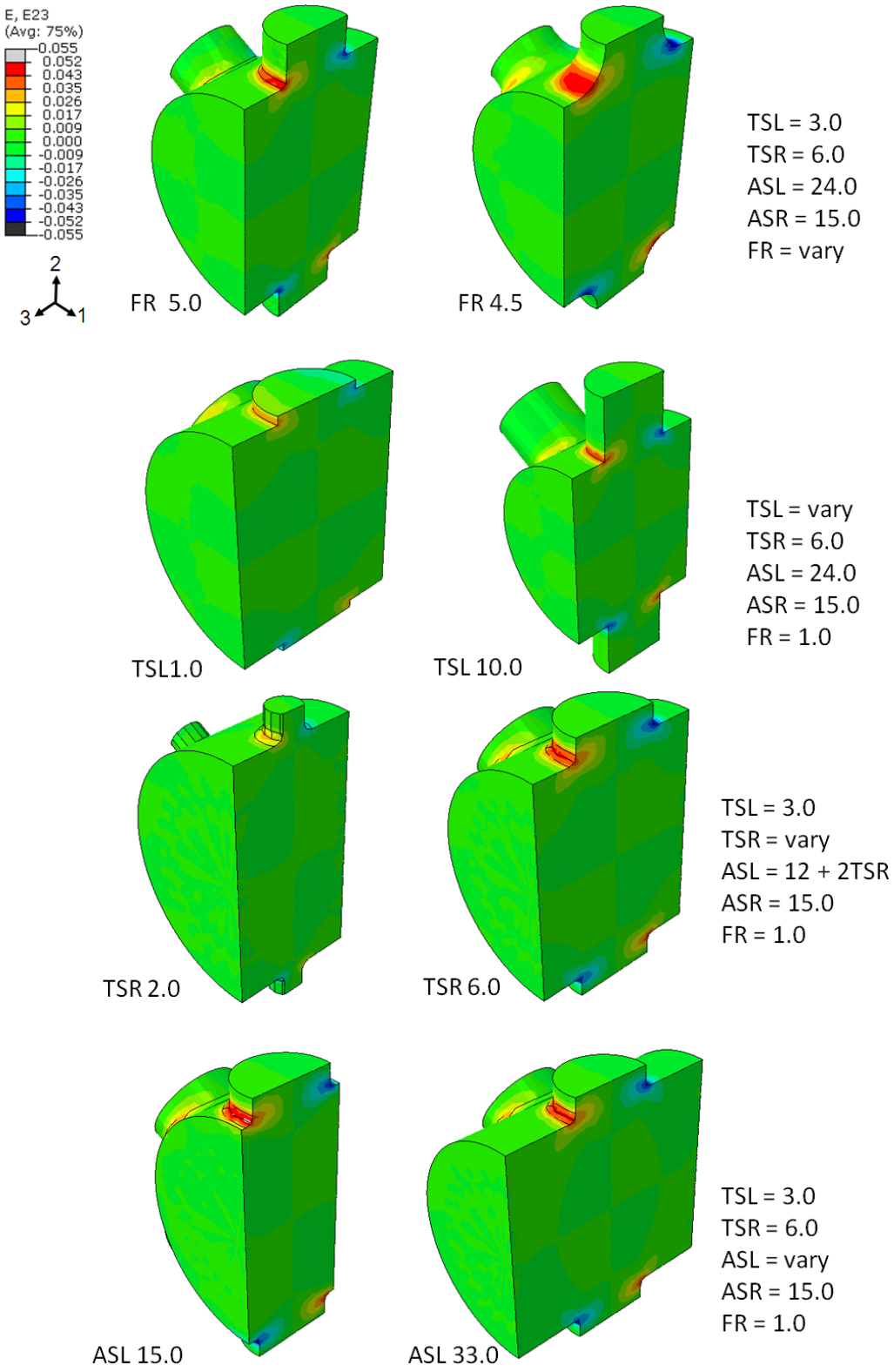


Figure 4-13: Shear strain, $\varepsilon_{23}$, contours (with a cross-sectional cut view) resulting from compressive loading in the 3-direction to a strain of 0.05, comparing the extremes in the variation of each of four parameters in the RVEs, same RVEs as Figure 4-9.

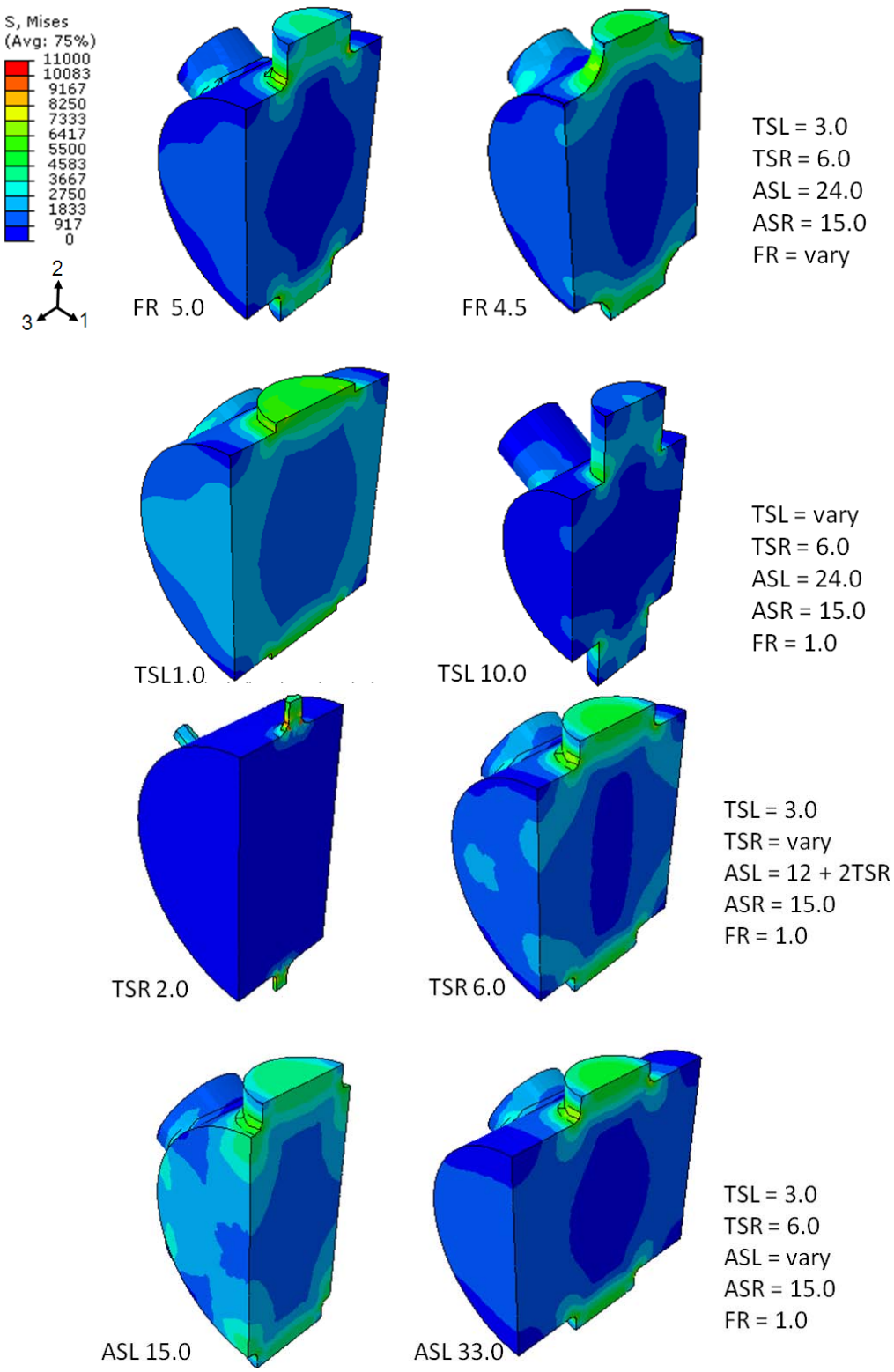


Figure 4-14: With the same RVEs as Figure 4-9, Mises contours (with a cross-sectional cut view) resulting from 2-3 directional shear loading to a strain of 0.05. (fillet radius (FR), transversal strut half-length (TSL), transversal strut radius (TSR), and axial strut length (ASL)).

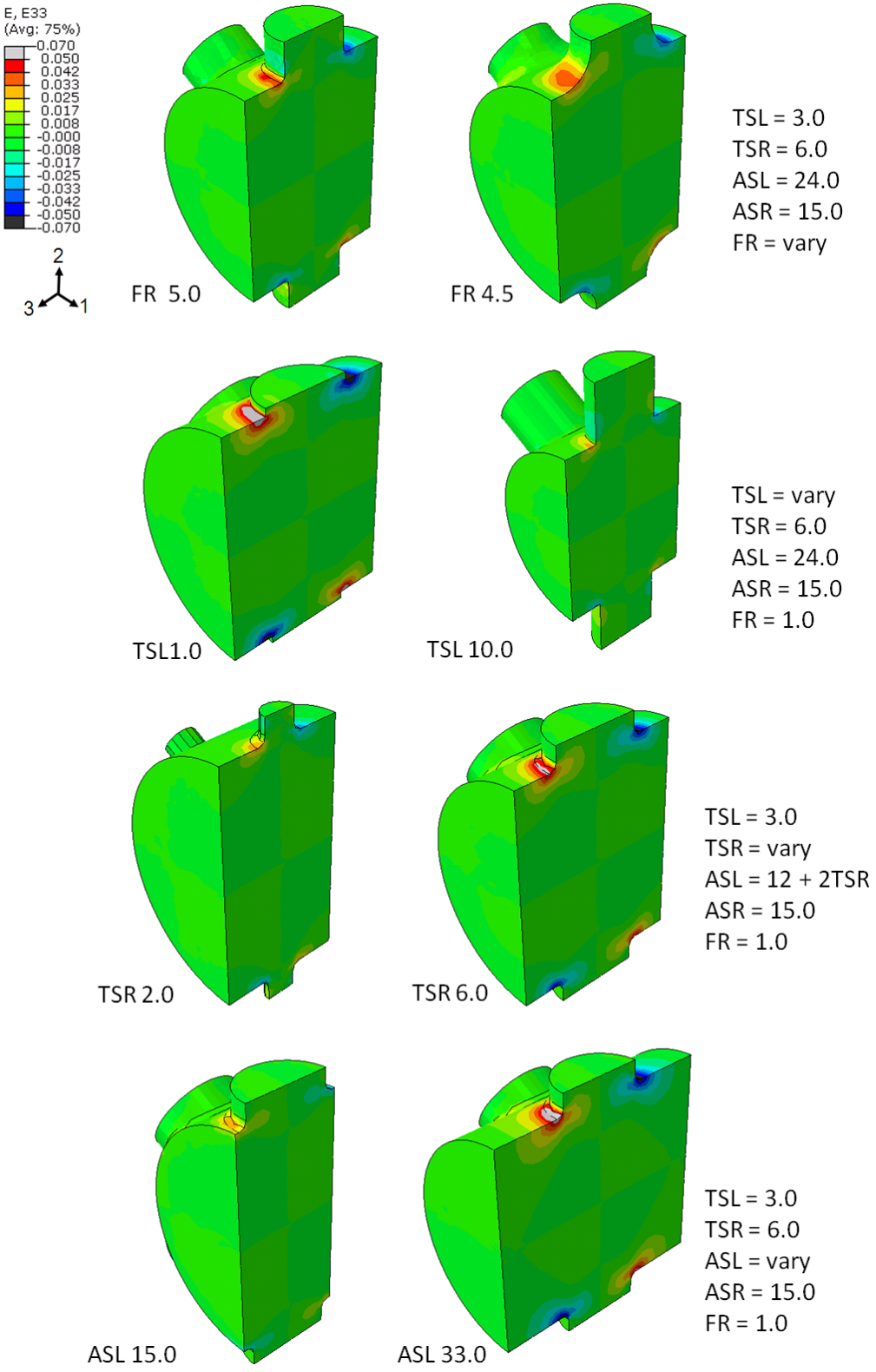


Figure 4-15: Axial strain, $\varepsilon_{33}$, contours (with a cross-sectional cut view) resulting from 2-3 directional shear loading to a strain of 0.05., comparing the extremes in the variation of each of four parameters in the RVEs, same RVEs as Figure 4-9.

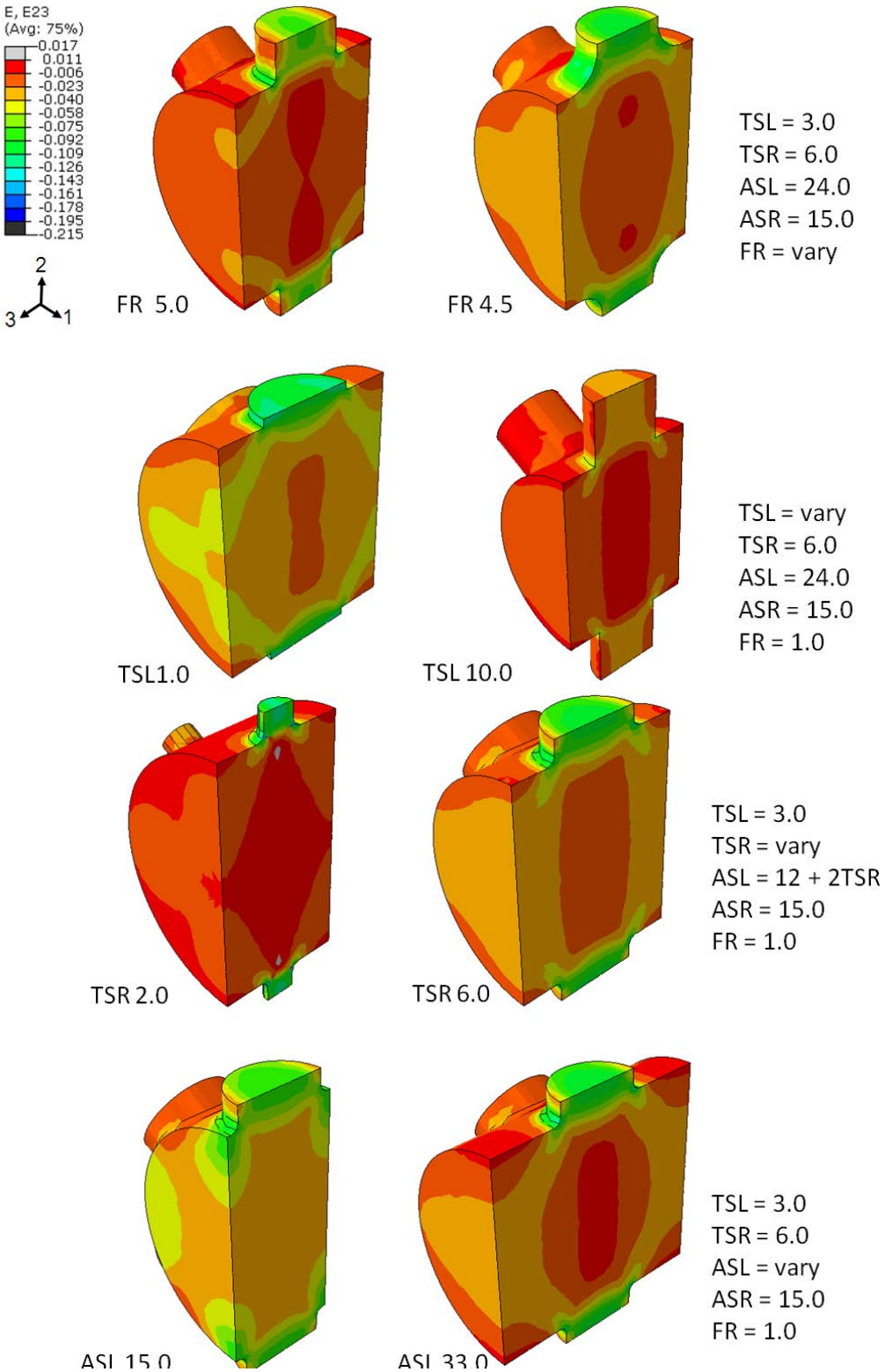


Figure 4-16: Shear strain, $\varepsilon_{23}$, contours (with a cross-sectional cut view) resulting from 2-3 directional shear loading to a strain of 0.05., comparing the extremes in the variation of each of four parameters in the RVEs, same RVEs as Figure 4-9.

Among the four variations in RVE geometry, the stress and strain contours reveal that the axial strut does carry a large portion of the compressive load when the structure is compressed axially, in the 3-direction, but the highest stress and strains are at the base of the transversal struts, which carries the shear strains. When loading in shear in the 2-3 direction, the base of the transversal struts carry most of the axial strain while the shear strains are distributed from the transversal strut to the axial struts. Consequently, when the connection between the transversal struts and the axial strut is larger (TSR) and stiffer (filleted), the shear strains imposed on the structure can be transferred to the axial strut from the smaller, transversal struts, and make the overall structure stiffer. If the shear stress and strains are isolated at the region around transversal struts, the structure will be more compliant.

With the four independent parameters of the representative volume, in addition to the fillet parameter, large differences in the compliance tensors can result for the same volume fraction due to the detail in the geometry of the RVE. The difference in the type of stresses carried by the transversal struts versus the axial struts causes this significant sensitivity to the relative geometries of the two types of struts in terms of radius, length and distances. The cumulative results from the four sets of simulations are plotted below (Figures 4-17 to 4-19).

In summary, the RVE is, as expected, a transversely isotropic structure, with the in-plane direction in the 1-2 plane. The elastic modulus E3 is most affected by volume porosity controlled by the transversal strut half-length (TSL). The moduli in the in-plane directions (E1 and E2) are more significantly affected by the transversal strut radius (TSR) and axial strut length (ASL). Both of these parameters, TSR and ASL, most significantly affect the shear moduli as well. Lastly, the axial strut radius (ASR) has a lesser effect on the moduli compared to the variation in the transversal strut.

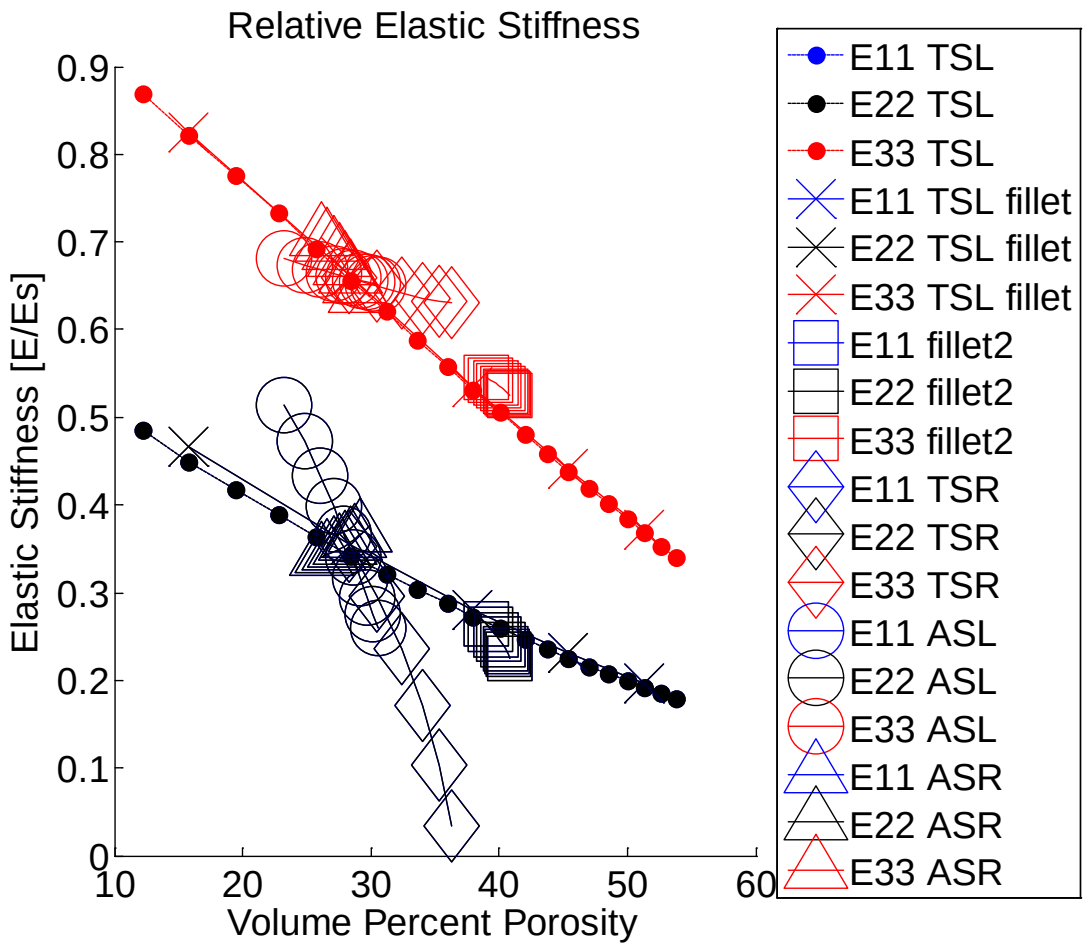


Figure 4-17: Effect of parameter variation on relative axial moduli.

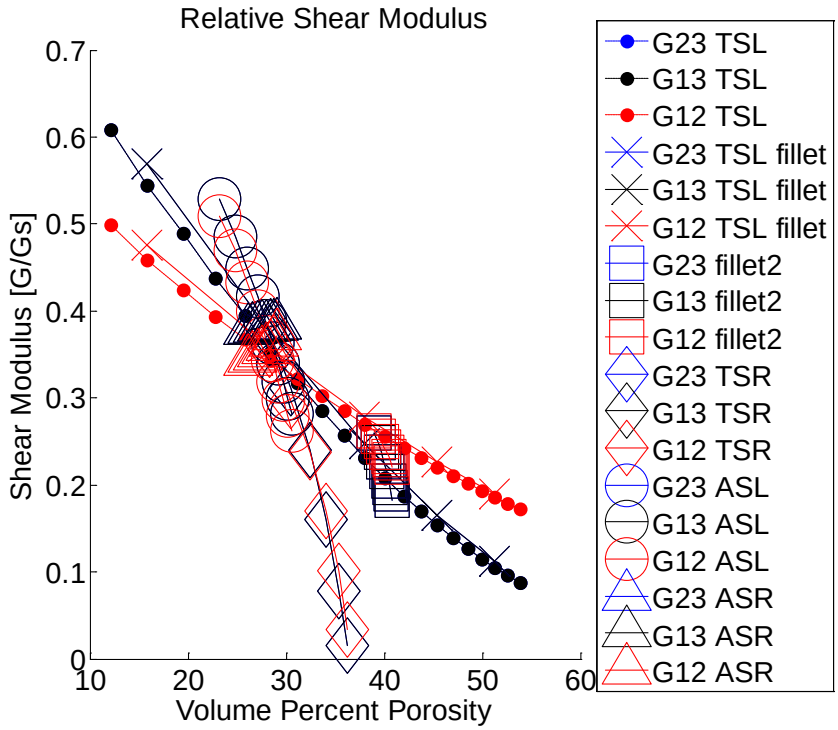


Figure 4-18: Effect of parameter variation on shear moduli.

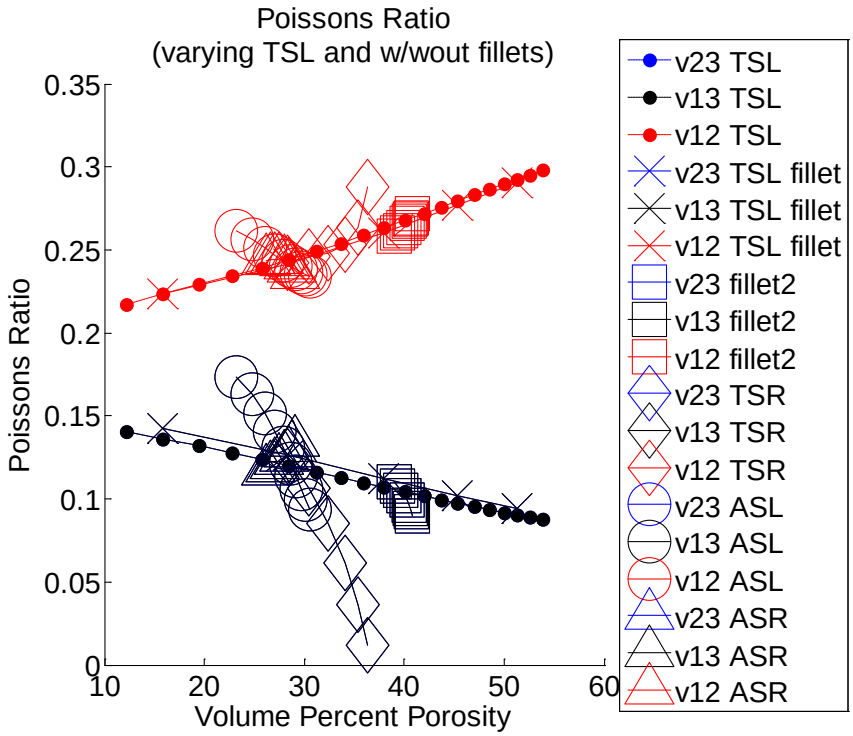


Figure 4-19: Effect of parameter variation on Poisson's ratio.

## 4.4 Identification of specific RVEs within aboral spine microstructure

The parameterization results in the previous section provides an understanding of how certain features control the anisotropy and load bearing response of the structure through a range of extreme feature aspect ratios, but only a fraction of the simulated RVEs were observed in the actual microstructure of the aboral spine. With the knowledge of the specific feature sizes and their corresponding axial distance from the socket of the aboral spine from microCT measurements (discussed in chapter 3), it is possible to isolate specific RVEs that represent the microstructure in a particular region along the longitudinal axis of the aboral spine (Figure 4-20 and Table 4-2). Although the representative volume element is transversely isotropic because the radii of the transversal struts in the RVE are generated from the average value of the transversal struts in the particular region, the actual repeating unit is not. In reality, the six transversal struts surrounding the axial strut are not identical and so some may be larger than others. Also, in the actual microstructure, some regions have intersecting transversal struts, such that two transversal struts come from same or overlapping base on the axial strut. Although not exact, these representative volumes are close approximations to the microstructure in the specified region and can predict the elastic mechanical properties in that region of the aboral spine. By interpolating between these instances, it is possible to generate a continuous gradient of porosity as well as mechanical stiffnesses within the aboral spine. With a gradient of RVE parameters, a continuum model can be created with a gradient of spatially varying anisotropic stiffnesses to simulate an entire aboral spine. This will be discussed in detail in the following chapter.

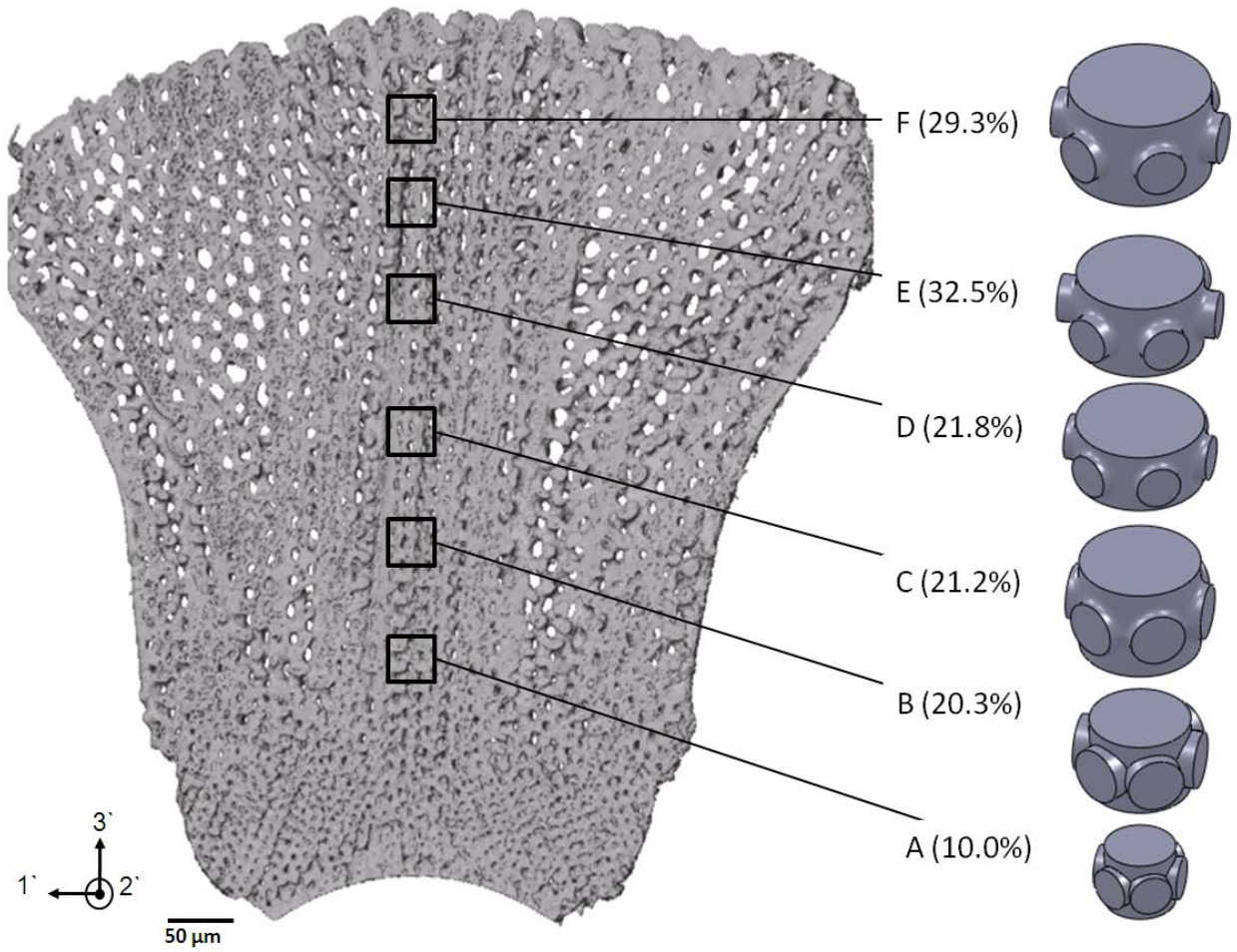


Figure 4-20: Six examples of idealized representative volume element using feature parameters found in specific regions of sample "b1s2" (Chapter 3) with volume porosities indicated.

Table 4-2: Parameters, volume fraction and porosity of the six RVE shown in Figure 4-20

| Label | Distance From Socket [µm] | TSR [µm] | ASR [µm] | ASL [µm] | 2 x TSL [µm] | Volume Fraction | Volume Porosity |
|---|---|---|---|---|---|---|---|
| A | 178.3 | 6 | 10 | 18 | 4 | 0.90 | 10.0% |
| B | 256.8 | 8 | 14.2 | 22.3 | 6.4 | 0.80 | 20.3% |
| C | 325.48 | 7.8 | 17 | 27.5 | 5 | 0.79 | 21.2% |
| D | 421.7 | 6.5 | 18 | 18 | 5 | 0.78 | 21.8% |
| E | 496.03 | 6.6 | 17.8 | 23 | 9.3 | 0.68 | 32.5% |
| F | 563.1 | 7 | 20 | 27 | 8 | 0.71 | 29.3% |

Table 4-3: Stiffness properties of the six representative volume elements derived from regions along the longitudinal axis of sample "b1s2" (See Figure 4-20 and Table 4-2).

| RVE Label | $E_1$ | $E_2$ | $E_3$ | $G_{23}$ | $G_{13}$ | $G_{12}$ | $\nu_{23}$ | $\nu_{13}$ | $\nu_{12}$ | Porosity |
|---|---|---|---|---|---|---|---|---|---|---|
| A | 39.03 | 38.86 | 51.82 | 16.17 | 16.20 | 16.14 | 0.18 | 0.18 | 0.20 | 10% |
| B | 40.04 | 39.63 | 49.46 | 15.60 | 15.68 | 16.25 | 0.18 | 0.18 | 0.22 | 20.3% |
| C | 33.16 | 33.16 | 53.49 | 14.34 | 14.34 | 13.42 | 0.15 | 0.15 | 0.23 | 21.2% |
| D | 36.06 | 36.06 | 53.82 | 15.36 | 15.36 | 14.35 | 0.16 | 0.16 | 0.26 | 21.8% |
| E | 24.25 | 24.25 | 43.57 | 8.94 | 8.94 | 9.59 | 0.12 | 0.12 | 0.26 | 32.5% |
| F | 24.00 | 23.99 | 47.76 | 9.66 | 9.66 | 9.57 | 0.11 | 0.11 | 0.25 | 29.3% |

# CHAPTER 5 Hierarchical Mechanical Modeling of Macroscale Aboral Spine

Utilizing the results from the previous chapter, an additional level of analysis could be performed by simulating a macro-scale study of the urchin's aboral armor spines. From the investigations in chapter 3 using SEM and microCT, the microstructure of each aboral spine of the *C. atratus* is not a homogenous distribution of the same repeating microstructural unit. There is an organized distribution of the material orientation within the macro-geometry of the aboral spine and a gradient in the porosity of the microstructure. With a reconstructed mesh of the actual geometry of the aboral spine and stiffness tensors for the range of porosities representative of the microstructure at different regions within the aboral spine, an approximation of the entire aboral spine, along with its microstructure could be simulated.

## 5.1 Aboral Spine Geometry

Due to the organized tiling of the aboral spines over the dome of the aboral side, each aboral spine has similar overall geometry with slightly different features. The aboral spines all possess a circular socket surface and begin with a profile just large enough to cover the diameter of the tubercle. Away from the tubercle, the profile then expands outward and preferentially to one side, until it reaches the adjacent aboral spine (Figure 3-8).

Because of the limit in the number of mesh faces in a finite element simulation, to determine the contribution of the microstructure to the geometric mechanical integrity of the aboral spines, the small variations and feature details of the geometry needed to be ignored in order to complete a finite element analysis in a reasonable time period. An idealized geometry

for an aboral spine, which captures the essential features of the unique shape, will adequately describes the aboral spines. For finite element simulation of the overall spine, the approximate geometry of the mushroom-shaped aboral spine was obtained by simplifying the exact morphology of a three-dimensional mesh created by a low resolution microCT scan of an aboral spine. The smoothed geometry was created by lofting the contours extracted from the raw mesh, with a contour spacing of 0.05 mm. The lofted surface was then imported into ABAQUS and converted to a solid tetrahedral mesh for finite element analysis. The processed mesh captures the overall geometry, the socket, the oblong shape, and some of the texture in the geometry, while ignoring the smaller details of the bumps on the surfaces (Figure 5-1).

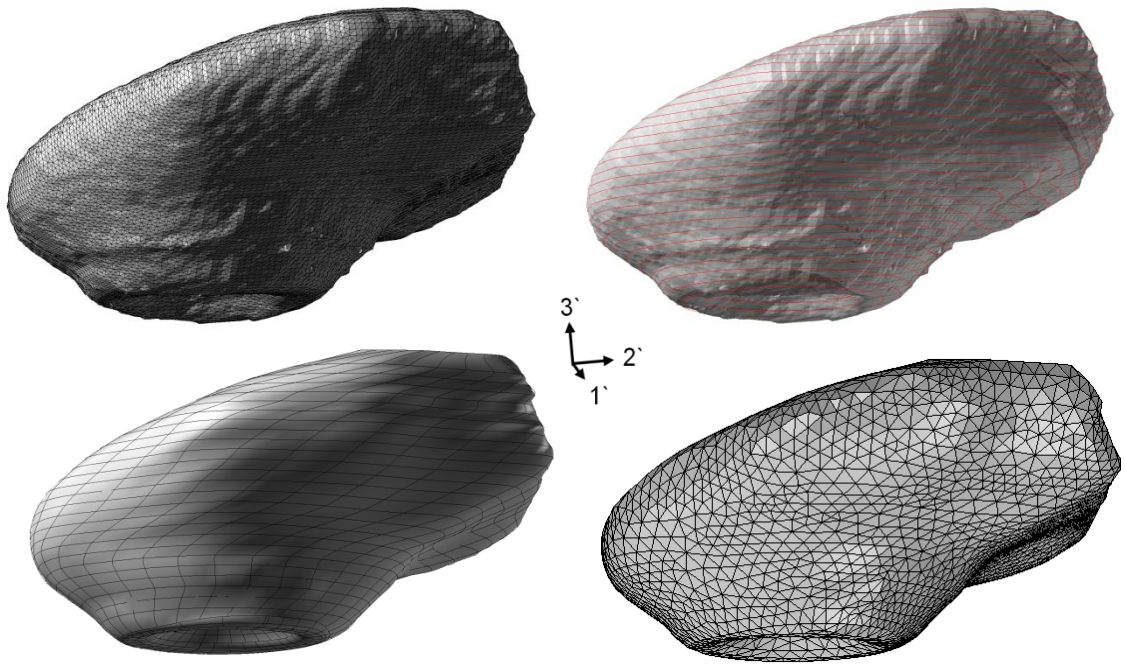


Figure 5-1: Remeshing of raw mesh from microCT 3D reconstruction: (a) Raw Mesh from MIMICS, (b) Contour in Rhinoceros with 0.05mm spacing, (c) Loft surface from contour lines, (d) ABAQUS tetrahedral mesh.

## 5.2 Heat simulation vector field and material orientation

From the SEM images and the microCT scans, it was apparent that the lines of the galleries stem from the socket and expand out, radially towards the surface of the aboral spine, ending perpendicular to the aboral spine surface. To mimic this organization in microstructure, a heat simulation using the aboral spine geometry was performed in ABAQUS using DC2D3 elements. Because only the heat flux vectors were extracted from this simulation, arbitrary material properties were used to ensure heat flux throughout the geometry (Table 5-1).

Table 5-1: Material properties for heat transfer simulation

| Property | Value |
|---|---|
| Conductivity | 6e7 σ |
| Density | 2.71 g/cm$^2$ |
| Specific Heat | 0.203 |

To obtain the radially outward distribution of vectors throughout the aboral spine, the socket surface was held at a temperature of 1000 while the aboral spine outer surface was held at a temperature of 0 (Figure 5-2). The heat flux vectors calculated at the centroid of each element was extracted and processed in MATLAB.

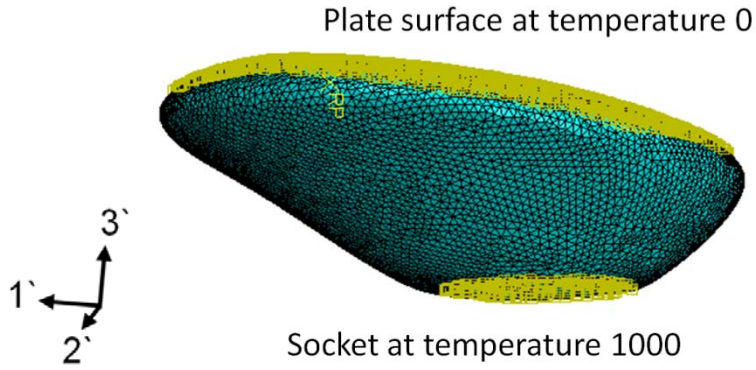


Figure 5-2: Boundary conditions for heat transfer simulation

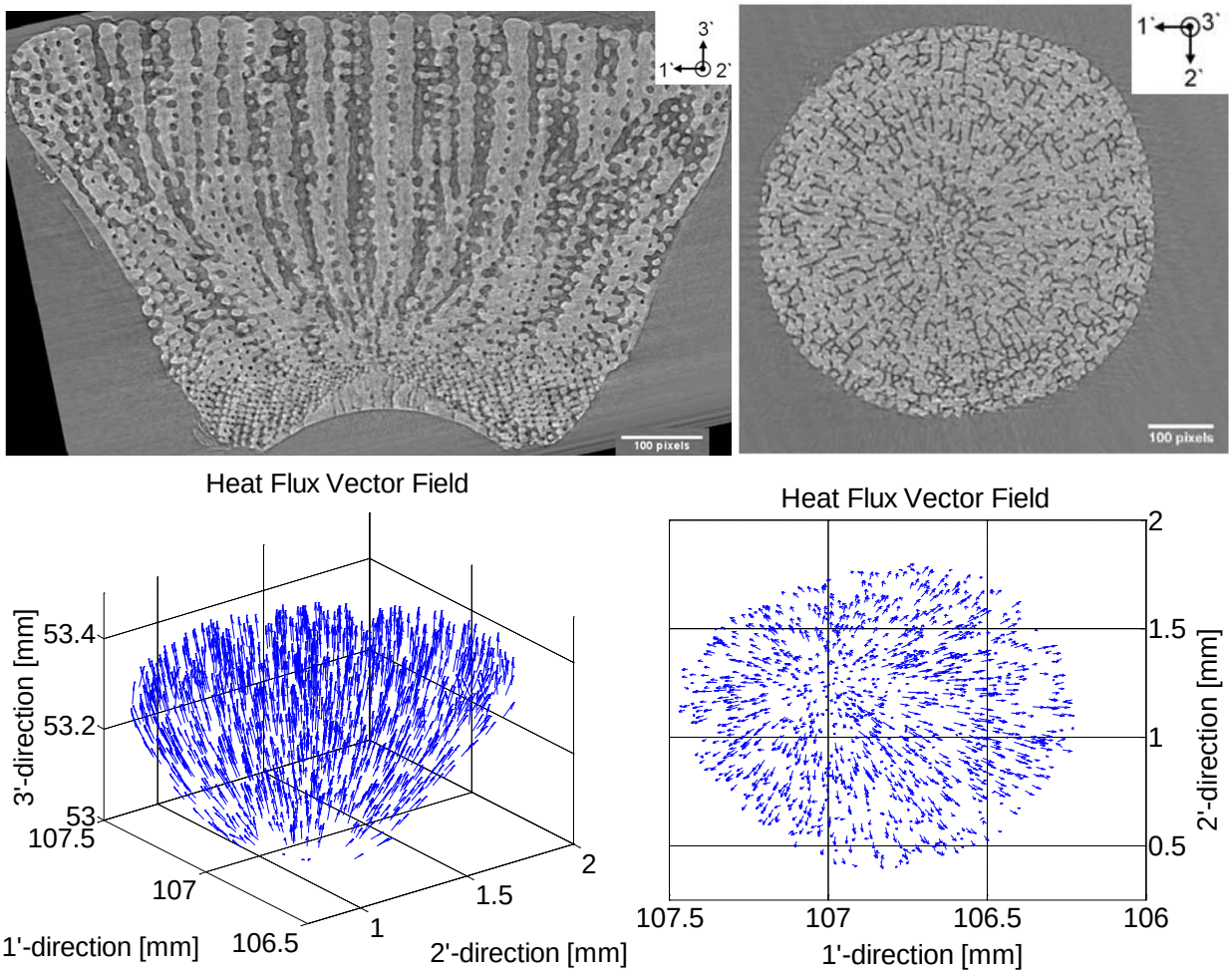


Figure 5-3: Longitudinal and transverse slices of aboral spine sample "b1s2" from X-ray microCT scans (APS 2BM, voxel size = 1.4μm) compared to the longitudinal and transverse view of the vector field obtained from the heat transfer simulation, plotted with MATLAB.

The resulting heat flux vectors are always orthogonal to the direction of heat flow, which mimic the suggested direction of growth of the urchin's aboral spine from observed the growth rings from cross-sectional micrographs (Figure 5-3). Comparing the heat flux vectors obtained from the heat simulation with cross-sectional slices of the aboral spine from uCT scans, the vector field of the heat flux vectors shows similar trends in orientations to the actual microstructural directional field. This method provides a good approximation of the

microstructural organization and distribution within the aboral spine. By preserving the mesh while changing the element type from DC2D3 to CPS3, the heat flux vectors were easily utilized to act as local material axis directions for each element in the mesh using *DISTRIBUTION and *ORIENTATION in the ABAQUS input file.

### 5.3 Porosity Gradient

In addition to the material orientation of each element, the porosity gradient within the aboral spine needs to be accounted for. From the parametric RVE model described in the previous chapter, the porosity gradient could be achieved by varying the stiffness properties of each element within the macroscopic aboral spine mesh to a specific RVE result in order to reflect a different porosity of the microstructure. The variation in properties was achieved using two different methods.

The first method uses the porosity distribution results found in chapter 3, of a roughly linear distribution of volume porosity as a function of distance from the socket (Figure 3-21). For the elements within the macroscopic aboral spine mesh, a linear interpolation between the porosity extremes at the socket (10% porosity) and the top aboral spine surface (50% porosity) based on distance from the socket and a specific variation in only one of the RVE feature parameter, the transversal strut half-length (TSL) is used to achieve a linear gradient in porosity. The parameters and elastic response were simulated and the results plotted in Figure 4-8.

Table 5-2: Relative stiffness properties of the six of the 20 representative volume elements simulated from variation in the transversal strut half-length from 0.5 to 10 microns with an increment of 0.5 microns (see Figure 4-8). Recall that $E_s$=73.5 GPa and $G_s$ = 29.4 GPa.

| RVE Label | $E_1/E_s$ | $E_2/E_s$ | $E_3/E_s$ | $G_{23}/G_s$ | $G_{13}/G_s$ | $G_{12}/G_s$ | $\nu_{23}$ | $\nu_{13}$ | $\nu_{12}$ | Porosity |
|---|---|---|---|---|---|---|---|---|---|---|
| TSL= 0.5 | 0.49 | 0.49 | 0.87 | 0.61 | 0.61 | 0.5 | 0.14 | 0.14 | 0.22 | 12.2% |
| TSL = 2.0 | 0.39 | 0.39 | 0.73 | 0.44 | 0.44 | 0.39 | 0.13 | 0.13 | 0.23 | 22.7% |
| TSL = 4.0 | 0.30 | 0.30 | 0.59 | 0.29 | 0.29 | 0.30 | 0.11 | 0.11 | 0.25 | 33.6% |
| TSL = 6.0 | 0.25 | 0.25 | 0.48 | 0.19 | 0.19 | 0.24 | 0.10 | 0.10 | 0.27 | 42% |
| TSL = 8.0 | 0.21 | 0.21 | 0.40 | 0.13 | 0.13 | 0.20 | 0.09 | 0.09 | 0.29 | 48.5% |
| TSL = 10 | 0.18 | 0.18 | 0.34 | 0.09 | 0.09 | 0.17 | 0.09 | 0.09 | 0.30 | 53.8% |

In the second method, an attempt to more closely mimic the microstructural variations within the aboral spine, the microstructural dimensions along the axial length of the aboral spine measured from the microCT analysis was used by linear interpolating between specific regions of the aboral spine of known microstructural RVE geometry, from sample “b1s2” (Figure 4-20 and Table 4-2). After stiffness tensor for each of the six representative volumes were calculated by the method described in chapter 4, a range of porosities and stiffness tensors were generated by interpolating within the porosity range between these six RVEs as well as interpolating the elastic constants between these six volumes (Table 5-3 and Figure 5-4).

Table 5-3: Relative stiffness properties of the six representative volume elements derived from regions along the longitudinal axis of sample “b1s2” (See Figure 4-20 and Table 4-2). $E_s$=73.5 GPa and $G_s$ = 29.4 GPa.

| RVE Label | $E_1/E_s$ | $E_2/E_s$ | $E_3/E_s$ | $G_{23}/G_s$ | $G_{13}/G_s$ | $G_{12}/G_s$ | $\nu_{23}$ | $\nu_{13}$ | $\nu_{12}$ | Porosity |
|---|---|---|---|---|---|---|---|---|---|---|
| A | 0.53 | 0.53 | 0.71 | 0.55 | 0.55 | 0.55 | 0.18 | 0.18 | 0.20 | 10% |
| B | 0.54 | 0.54 | 0.67 | 0.53 | 0.53 | 0.55 | 0.18 | 0.18 | 0.22 | 20.3% |
| C | 0.45 | 0.45 | 0.73 | 0.49 | 0.49 | 0.46 | 0.15 | 0.15 | 0.23 | 21.2% |
| D | 0.49 | 0.49 | 0.73 | 0.52 | 0.52 | 0.49 | 0.16 | 0.16 | 0.26 | 21.8% |
| E | 0.33 | 0.33 | 0.59 | 0.30 | 0.30 | 0.33 | 0.12 | 0.12 | 0.26 | 32.5% |
| F | 0.33 | 0.33 | 0.65 | 0.33 | 0.33 | 0.33 | 0.11 | 0.11 | 0.25 | 29.3% |

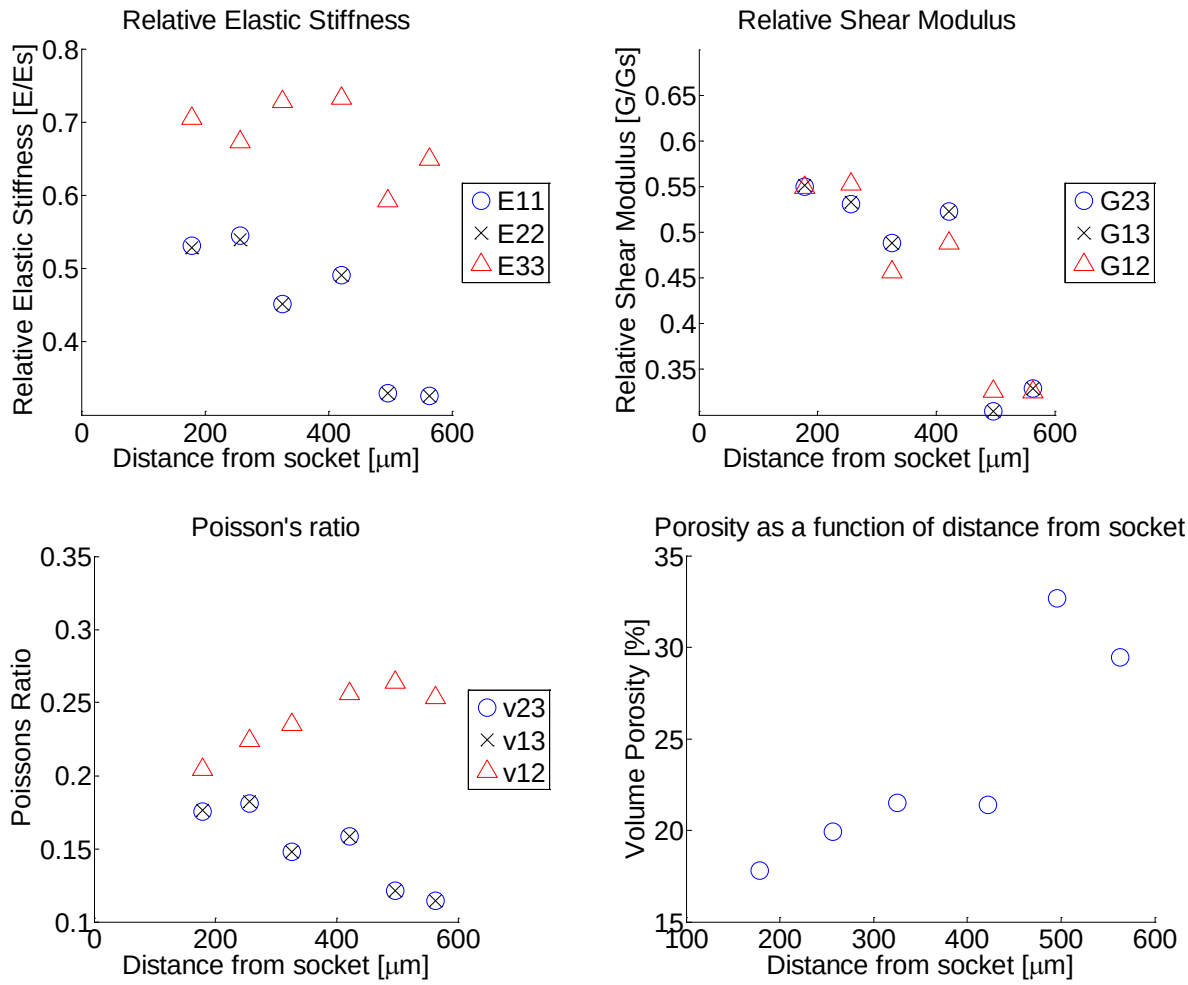


Figure 5-4: The relative Young's and shear moduli (with respect to the solid moduli used: 73.5GPa and 29.4GPa) and Poisson's ratio of RVE derived from specific, isolated regions in the aboral spine sample "b1s2" (shown in Figure 4-20 and Table 4-2). Gradient in volume porosity as a function of distance from the socket is also plotted.

The result is a gradient in material properties incorporating the six found in the regions specified along the aboral spine, sample "b1s2". The resulting effect of the two methods of approximating the porosity gradient within the aboral spine is discussed in the next section.

## 5.4 Aboral spine loading conditions

With a full multiscale model and elastic material properties, five comparative simulations on the macroscale aboral spine were performed for the case of a conical indenter and a flat plate indenter at the same location on the top surface of the aboral spine. For the indentation, the aboral spine is fixed at the socket surface and the indenter tip is lowered in the 3` direction to a depth of 0.1mm beneath the surface of the aboral spine and then unloaded. The five simulation conditions are as follows:

First, for an upper bound on the material response, the aboral spine is modeled as an isotropic, solid calcite with no porosity. Second, the linear increase in porosity as a function of distance from the socket region is mimicked by using a feature variation of the microstructure along the axis of the aboral spine, the transversal strut half-length (TSL), (Table 5-2). Each element in the aboral spine is assigned an anisotropic elastic stiffness tensor based on its position from the socket region of the aboral spine. The porosity gradient is assumed to be linear with the distance from the middle of the socket surface. In the third simulation, all of the elements in the mesh are anisotropic but identical, with the values from the lowest porosity RVE, and oriented with respect to the orientation vector field. The fourth and fifth simulations are similar except with the anisotropic values of the average porosity RVE and highest porosity RVE. In the last simulation, the microstructural variations are more closely mimicked by interpolating between the resulting elastic constants (Table 5-3) of the six RVE's described in Figure 4-20 and Table 4-2, which represent the microstructural characteristics of certain spatial positions along the 3` direction of the aboral spine. The six types of material composition for the aboral spine are summarized below in Table 5-4.

Table 5-4: Parameters used for each of the cases loading of the aboral spine

| Loading Case | Anisotropy of Material Elements | Gradient | Volume Porosity |
|---|---|---|---|
| Isotropic solid calcite | Isotropic | Uniform | 0% |
| Anisotropic uniform low porosity | Anisotropic | Uniform | 10% |
| Anisotropic uniform average porosity | Anisotropic | Uniform | 30% |
| Anisotropic uniform high porosity | Anisotropic | Uniform | 50% |
| Anisotropic graded porosity | Anisotropic | Graded | Linear gradient of porosity with distance from socket surface: 10% to 50%, achieved by varying TSL (Table 5-2) |
| Anisotropic interpolated graded porosity | Anisotropic | Graded | Linear interpolation between 6 known regions of RVE (Table 5-3 and Figure 4-20) |

## 5.5 Aboral spine loading results

Comparing the five types of materials used in the indentation simulations, for both the flat plate and conical (end-tip radius of 0.1 mm) indenters, the force displacement curves show the solid, isotropic calcite as the stiffest material with the greatest reaction force directly under the indenter (Figures 5-5 and 5-12). When an anisotropic porosity gradient was incorporated into the material specifications of each element, the stiffness is lower than if the aboral spine had been composed of an RVE with the lowest porosity and higher than if the entire aboral spine had been composed of the highest porosity RVE, as one would expect. Although the two types of anisotropic porosity gradients are slightly different and span different ranges in porosity, the result for both is similar. The aboral spine with an anisotropic porosity gradient was slightly stiffer than if the aboral spine were composed of RVE with the average porosity of 30%.

Comparing the Mises stress distribution in the six cases, for the conical and flat plate indentation, the axial stress contours of the deformed aboral spine reveals a higher of stress state for the isotropic aboral spine, due to the stiffer isotropic solid material (Figure 5-6 and Figure 5-13). As expected, the highest compressive stresses occur at the edge of the fixed socket region and the region under the indenter. This high compressive stress as well as the high tensile stress region (from the position of the indent and the cantilevered geometry of the plate) is shown in the axial stress distribution (Figure 5-7 and 5-14). Again, the isotropic material is stiffest, with the highest stress state, while the anisotropic gradient cases have axial strains closer to the average uniform porosity case. This is mirrored in the contours of the axial strain in Figure 5-10 and 5-17, where there is a compressive axial strain region at the socket and a tensile strain at the surface to the right of the indenter. In the anisotropic gradient case, the compressive axial strains at the socket are much smaller than those in the average and high porosity case. The shear stress distribution in the transverse direction, 1`-3` direction, reveals a smaller transverse shear strain at the indentation surface in the two anisotropic graded porosity cases compared to the average porosity and high porosity case (Figure 5-8 and 5-15). The shear strains in this transverse direction for the anisotropic graded cases exhibit larger strains directly under the indenter than the high porosity case, but a smaller shear strain in the other regions of the spine compared to the average and high uniform porosity cases (Figure 5-11 and 5-18).

Since the aboral spine can be thought of as a unit for absorbing energy from loads subjected to the exterior surface of the aboral spine, the indentation depth of equal energy absorption (equal to the energy absorbed for the graded porosity case at highest indentation depth simulated) for the isotropic solid calcite and low porosity case were plotted as well (Figure 5-5 and 5-12). For the flat plate indenter, the energy absorbed of the anisotropic graded porosity case at a depth

of 0.176 mm was calculated from area under the indentation curve to be a value of 8.228e-6 J. This corresponded to roughly the same energy absorbed in the isotropic solid case at depth of 0.132 mm and the anisotropic, low uniform porosity case at a depth of 0.156 mm. For the conical indentation, the energy absorbed for the anisotropic graded porosity case at a depth of 0.096 mm was 1.797e-6 J, which corresponds to a depth of 0.068 mm and 0.084 mm for the isotropic solid case and the anisotropic, low uniform porosity case, respectively. Because of the stiffer response of the solid isotropic calcite case and the low porosity case, for the same energy absorbed, the indenter penetrates deeper into the aboral spine with the graded porosity. Comparing the Mises stress of the isotropic solid case and the anisotropic graded case at the state of the same energy absorption (different indentation depths), the isotropic case has higher stresses directly under the indenter (Figure 5-19). The graded porosity case shows higher strains near the surface of the aboral spine, but smaller strains at the socket.

The similarities in all of the contours reveal that regardless of indenter type, compared to the isotropic solid and the anisotropic uniform low porosity case, because of the more compliant surface, the anisotropic graded case exhibit a lower stress state at the same depth and at the same amount of energy absorbed. Both the axial and shear stress in the graded anisotropic case are thus higher than the isotropic solid and low porosity anisotropic case at the surface. Yet, at the socket region, the stresses are lower. The both the axial and transverse strains are thus higher at the surface of the aboral spines in the graded case, but there are also smaller axial and shear strains at the socket region in the graded case compared to the isotropic solid and nearly solid anisotropic cases. Compared to the anisotropic, high porosity case, although the stress state is lower in the high porosity case, it exhibits higher strains than the graded case. Basically, the exterior surface of the aboral spine deforms more significantly in the graded porosity case, which

in turn prevents higher strains near the socket region of the aboral spine from developing and obtains a similar stress state of a higher porosity material without the lower overall stiffness response at the socket.

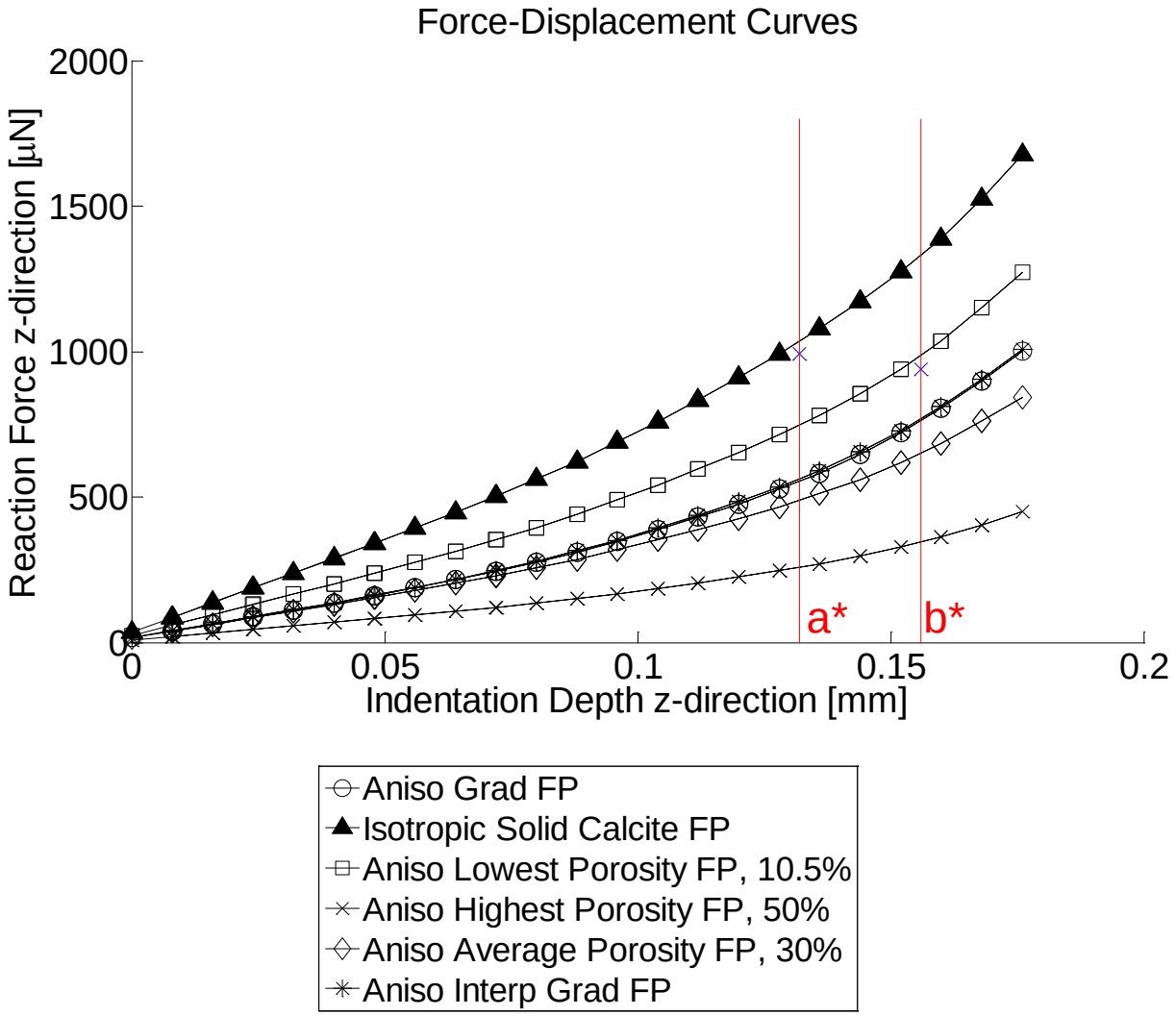


Figure 5-5: Force-Depth curves for indentation with a rigid flat plate using various elastic material property gradients within aboral spine described in the previous section. The two vertical lines indicate the equivalent depth of indentation for each case, a* (for the isotropic solid calcite case) and b* (for the anisotropic lowest uniform porosity case), where the energy absorbed is the same as the energy absorbed in the anisotropic interpolated gradient case at the final depth of indentation, 0.176 mm. The indentation depth at a* is 0.132 mm and at b* is 0.156 mm.

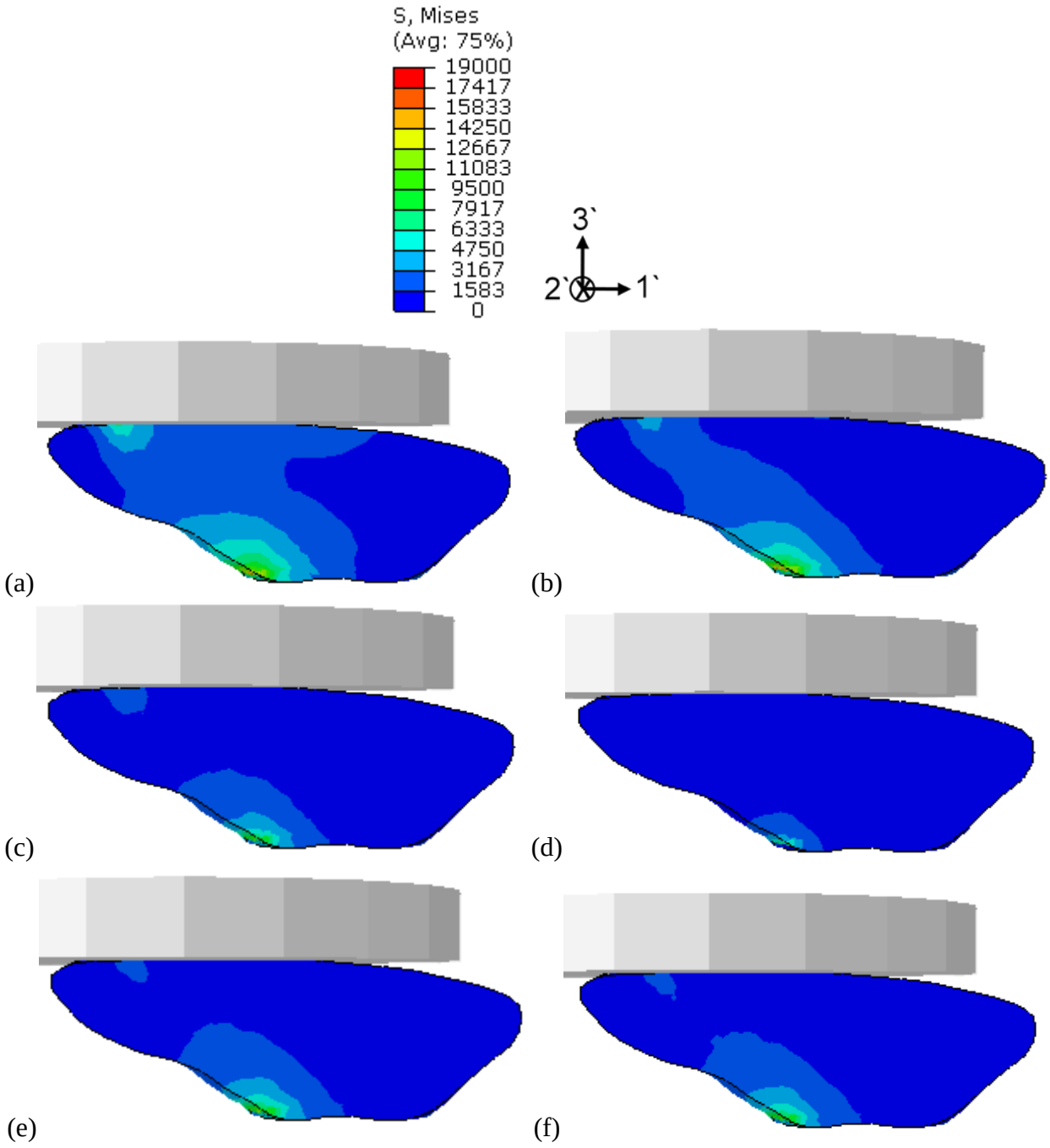


Figure 5-6: Comparing the Mises stress distribution of isotropic solid aboral spine under flat plate loading to a depth 0.1mm with the Mises stress distribution of several cases of anisotropic aboral spines, with material orientation specified, under flat plate loading to a depth 0.1mm. (a) isotropic solid calcite, (b) anisotropic low uniform porosity 10% (c) anisotropic average uniform porosity 30% (d) anisotropic high uniform porosity 50% (e) anisotropic graded porosity 10% to 50% (f) anisotropic graded porosity interpolated RVEs.

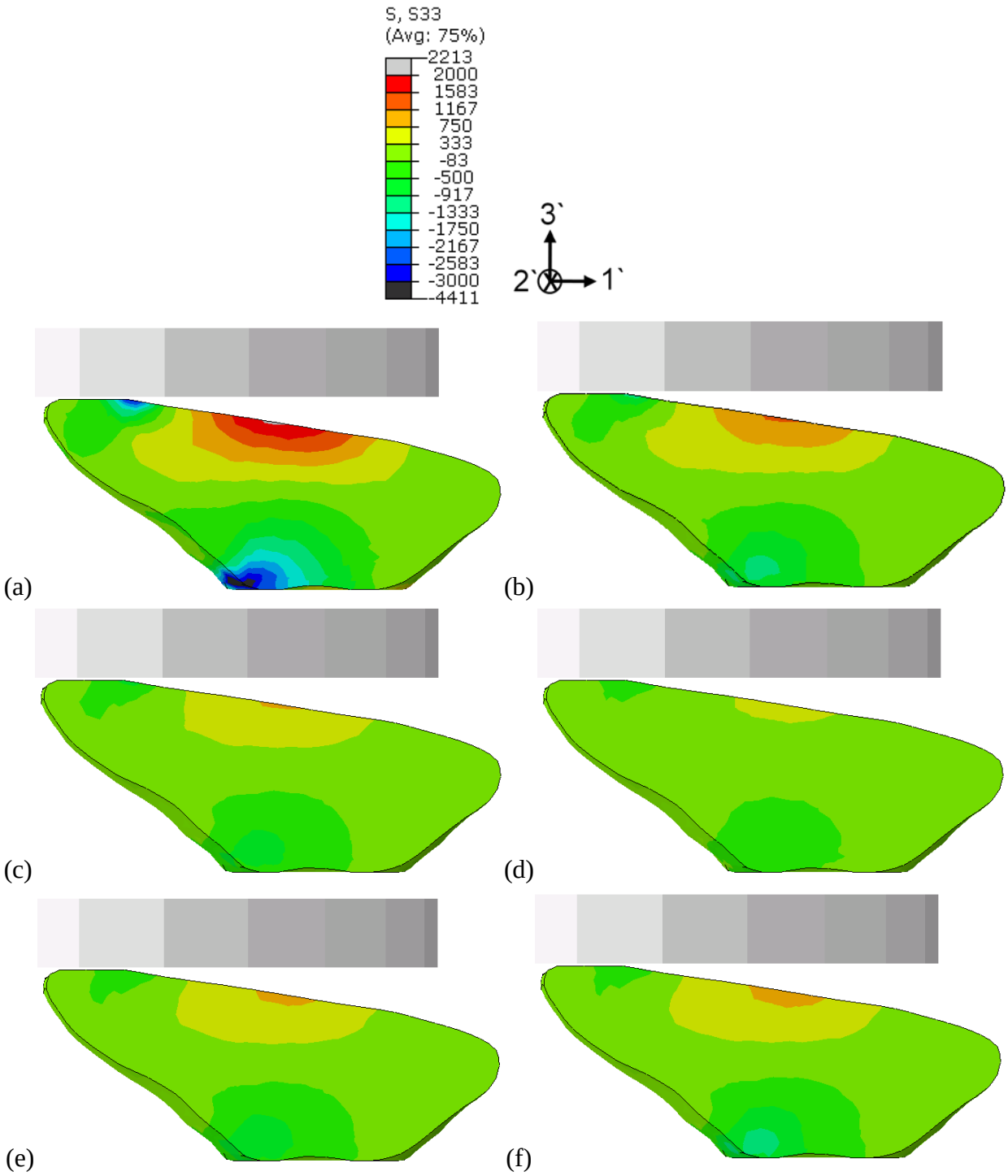


Figure 5-7: Comparing specifically the axial stress, $\sigma_{3'3'}$, distribution of isotropic solid aboral spine under flat plate loading to a depth 0.1mm with the axial stress distribution of several cases of anisotropic aboral spines, with material orientation specified, under flat plate loading to a depth 0.1mm. Labels **a-f** refers to the same loading cases as Figure 5-6.

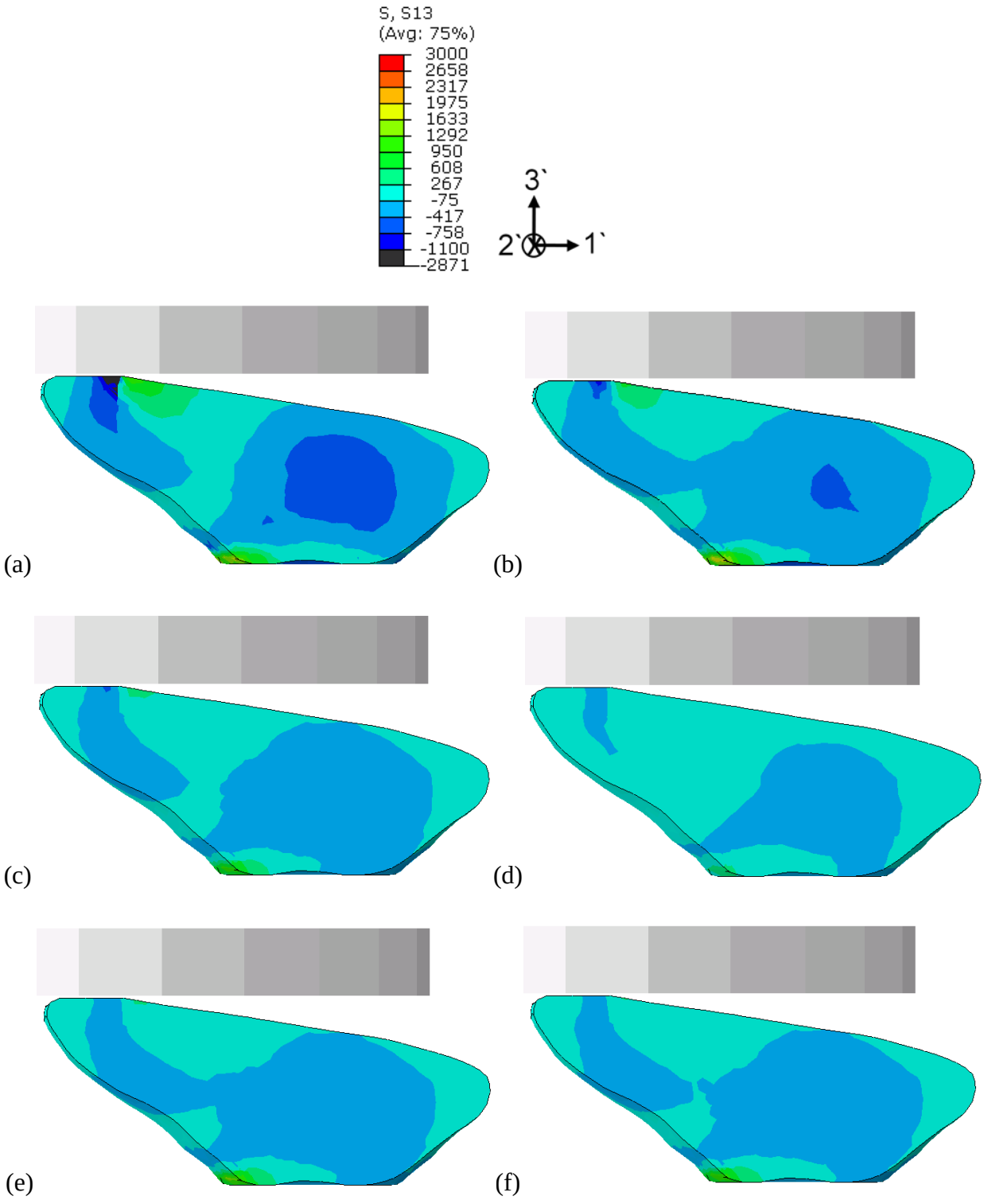


Figure 5-8: The shear stress, $\sigma_{1'3'}$, distribution of isotropic solid aboral spine under flat plate loading to a depth 0.1mm with the shear stress distribution of several cases of anisotropic aboral spines, with material orientation specified, under flat plate loading to a depth 0.1mm. Labels **a-f** refers to the same loading cases as Figure 5-6.

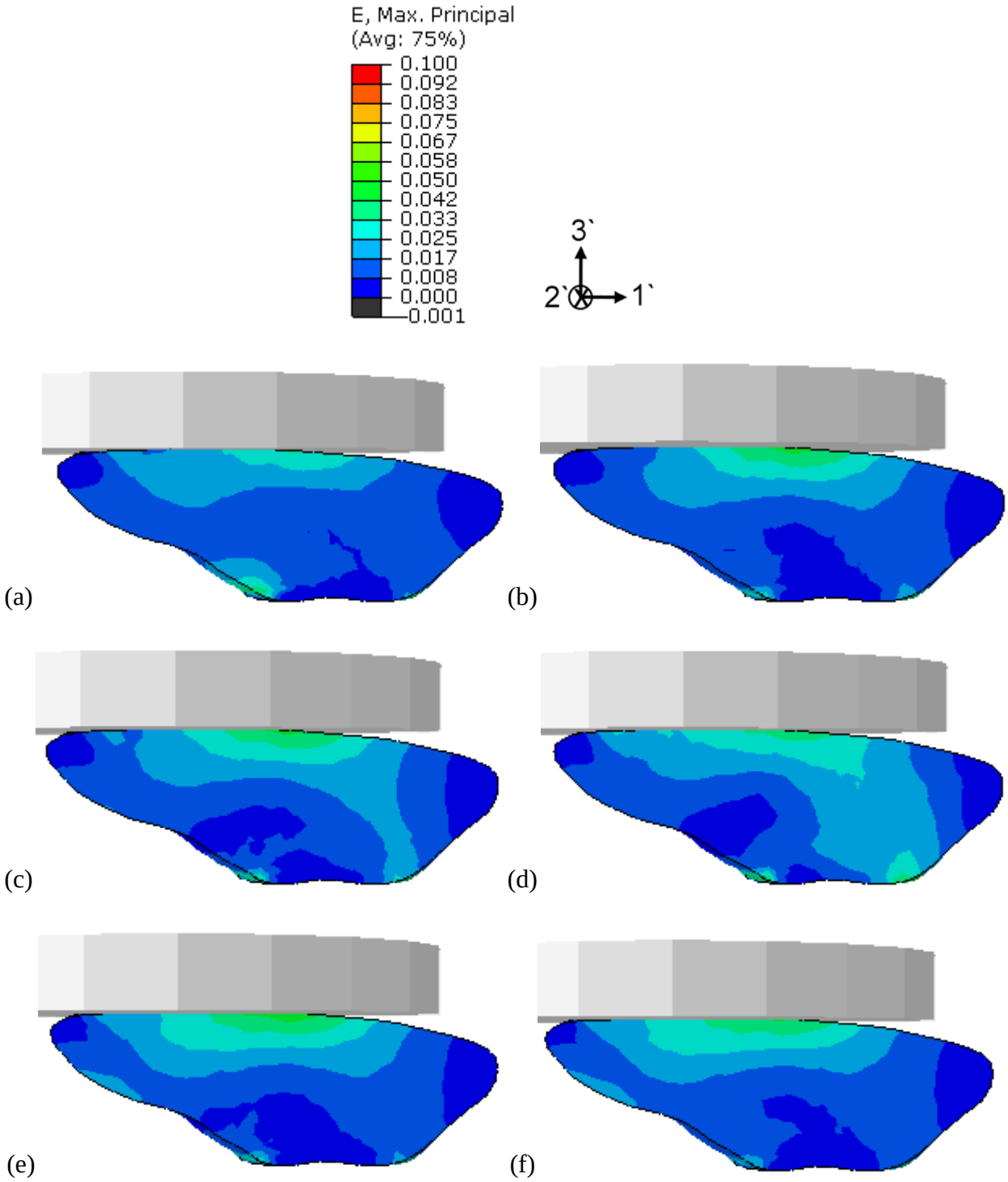


Figure 5-9: Comparing the maximum principal strain distribution of isotropic solid aboral spine under flat plate loading to a depth 0.1mm with the maximum principal strain distribution of several cases of anisotropic aboral spines, with material orientation specified, under flat plate loading to a depth 0.1mm. Labels **a-f** refers to the same loading cases as Figure 5-6.

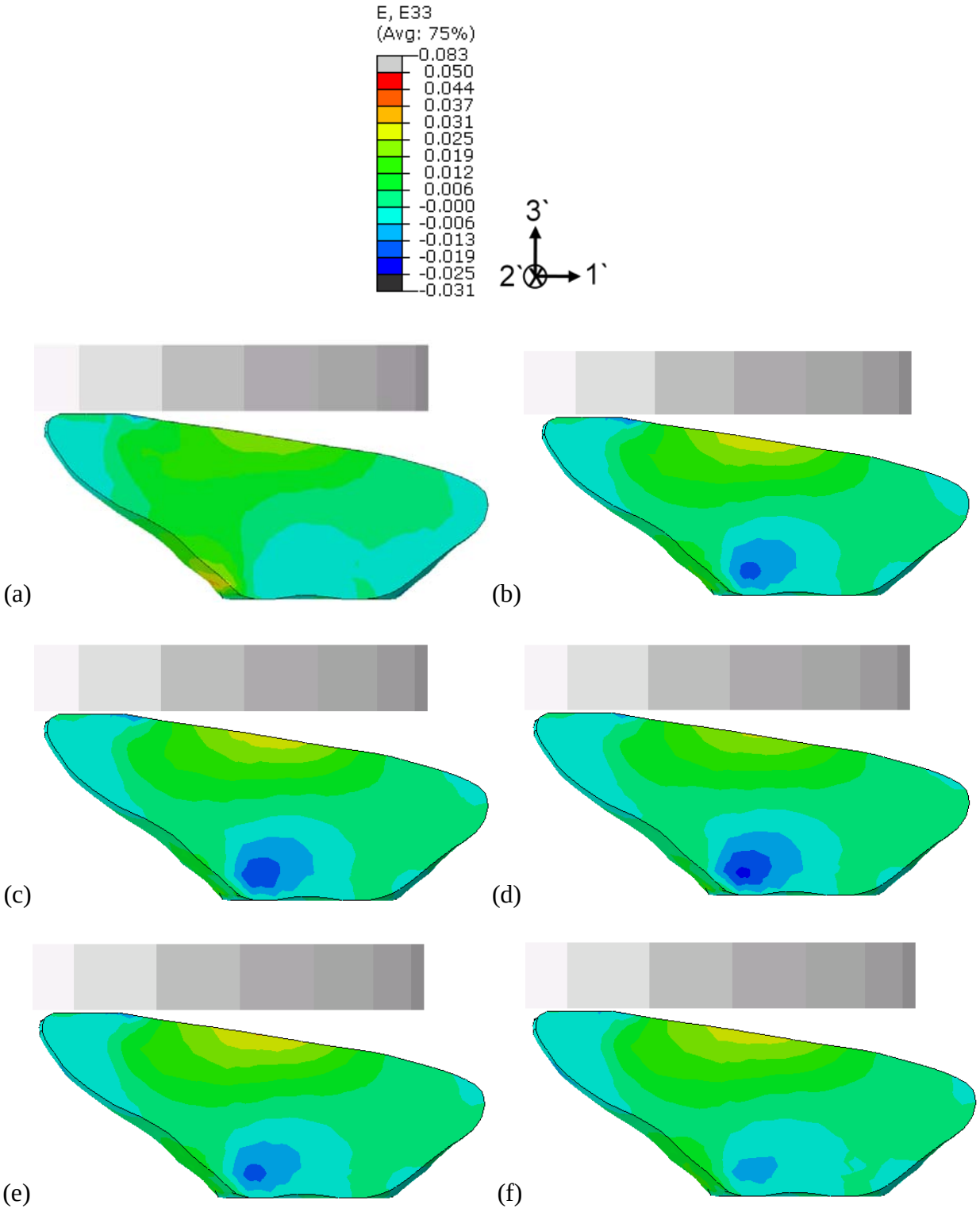


Figure 5-10: The axial strain, $\varepsilon_{3'3'}$, distribution of isotropic solid aboral spine under flat plate loading to a depth 0.1mm with the axial strain distribution of several cases of anisotropic aboral spines, with material orientation specified, under flat plate loading to a depth 0.1mm. Labels **a-f** refers to the same loading cases as Figure 5-6.

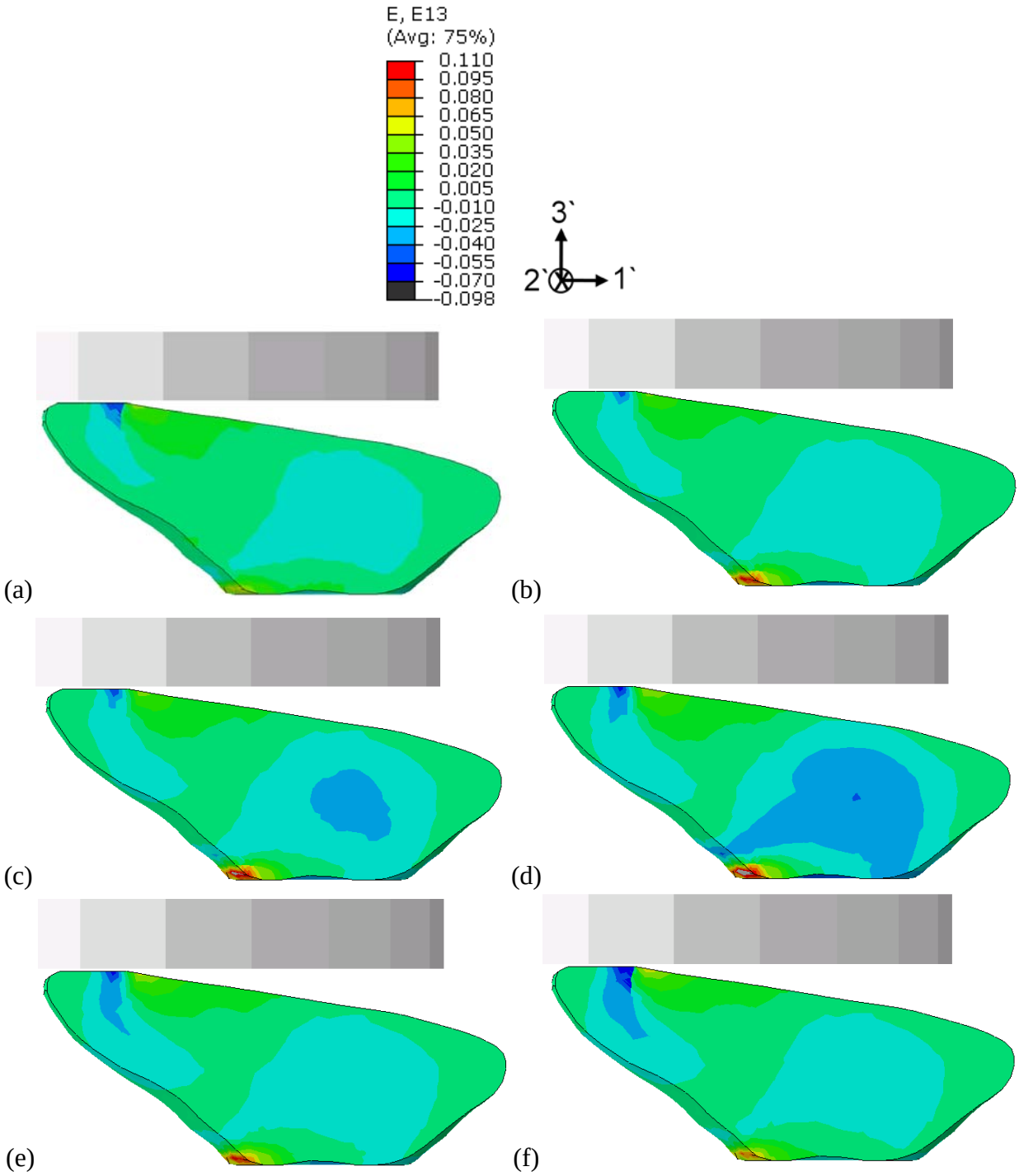


Figure 5-11: Comparing the shear strain, $\varepsilon_{1'3'}$, distribution of isotropic solid aboral spine under flat plate loading to a depth 0.1mm with the shear strain distribution of several cases of anisotropic aboral spines, with material orientation specified, under flat plate loading to a depth 0.1mm. Labels **a-f** refers to the same loading cases as Figure 5-6.

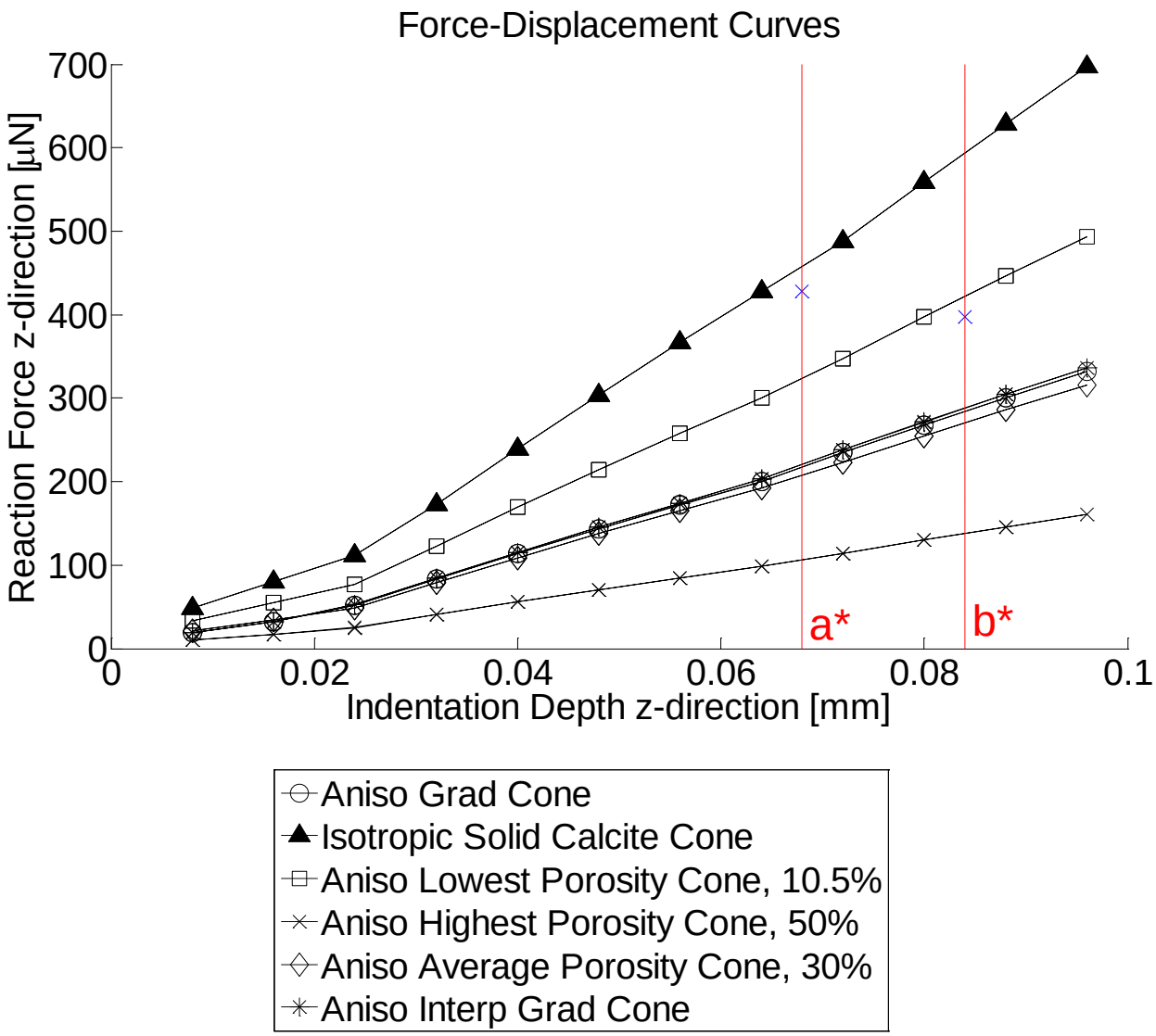


Figure 5-12: Force-Depth curves for indentation with a rigid conical indenter with the same set of material gradients as Figure 5-5. Similar to the flat plate case, the two vertical lines indicate the equivalent depth of indentation for each case, a* (for the isotropic solid calcite case) and b* (for the anisotropic lowest uniform porosity case), where the energy absorbed is the same as the energy absorbed in the anisotropic interpolated gradient case at the final depth of indentation, 0.096 mm. The indentation depth at a* is 0.068 mm and at b* is 0.084 mm.

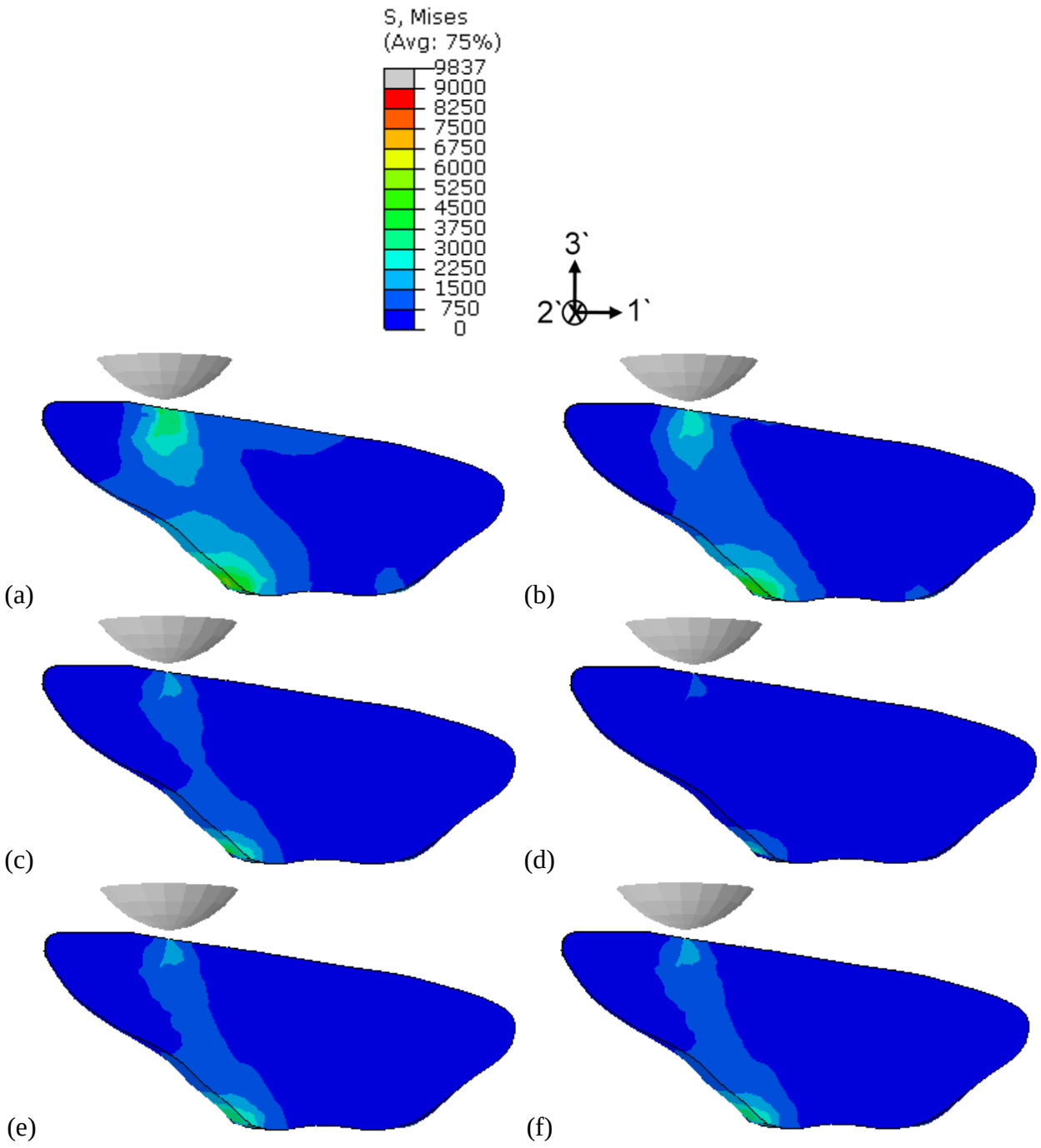


Figure 5-13: Comparing the Mises stress distribution of isotropic solid aboral spine under conical indenter loading to a depth 0.1mm with the Mises stress distribution of several cases of anisotropic aboral spines, with material orientation specified, under conical indenter loading to a depth 0.1mm. Similar to Figure 5-6, (a) isotropic solid calcite, (b) anisotropic low uniform porosity 10% (c) anisotropic average uniform porosity 30% (d) anisotropic high uniform porosity 50% (e) anisotropic graded porosity 10% to 50% (f) anisotropic graded porosity interpolated RVEs.

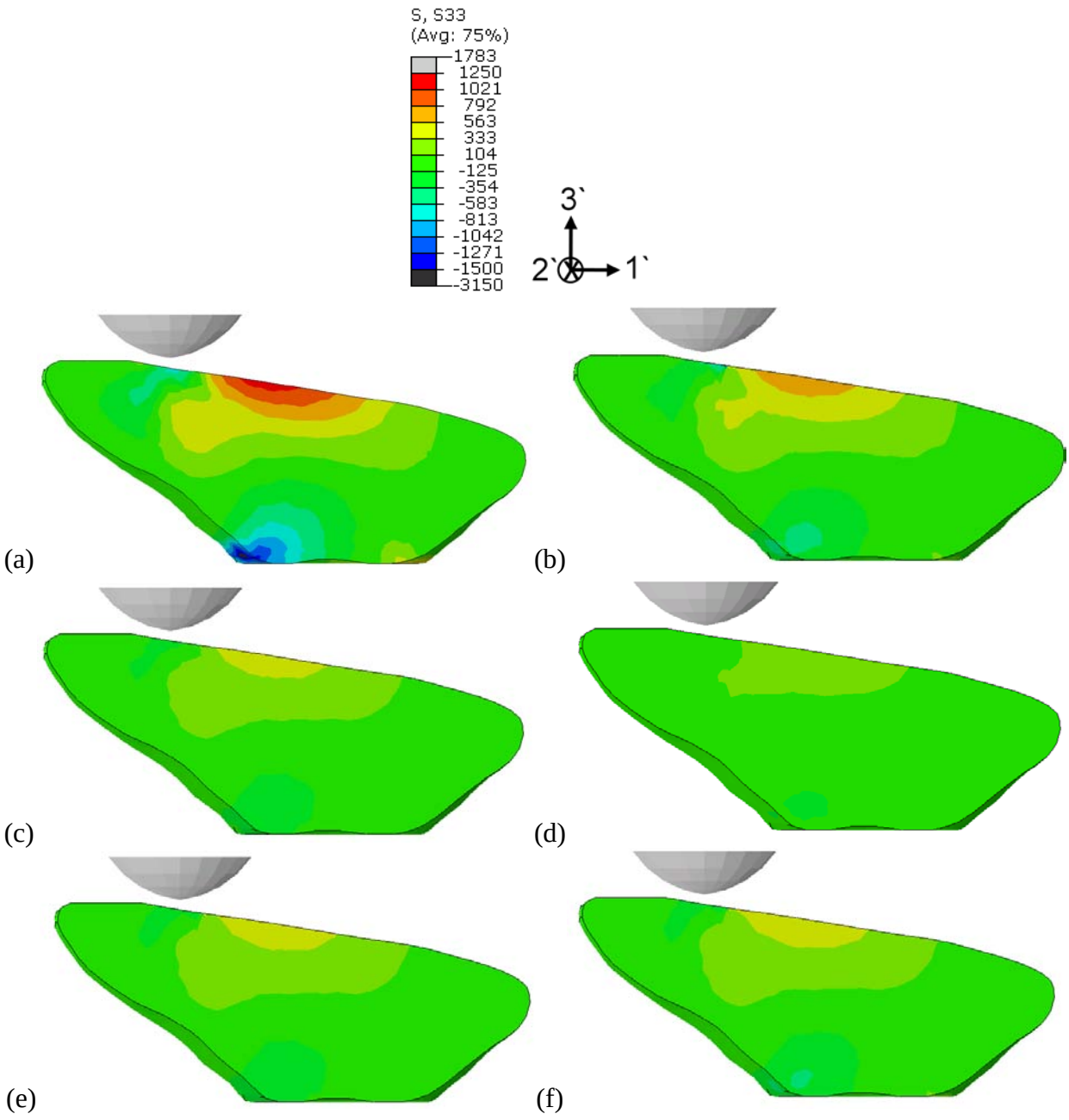


Figure 5-14: Comparing specifically the axial stress, $\sigma_{3'3'}$, distribution of isotropic solid aboral spine under conical indenter loading to a depth 0.1mm with the axial stress distribution of several cases of anisotropic aboral spines, with material orientation specified, under conical indenter loading to a depth 0.1mm. Labels **a-f** refers to the same loading cases as Figure 5-13.

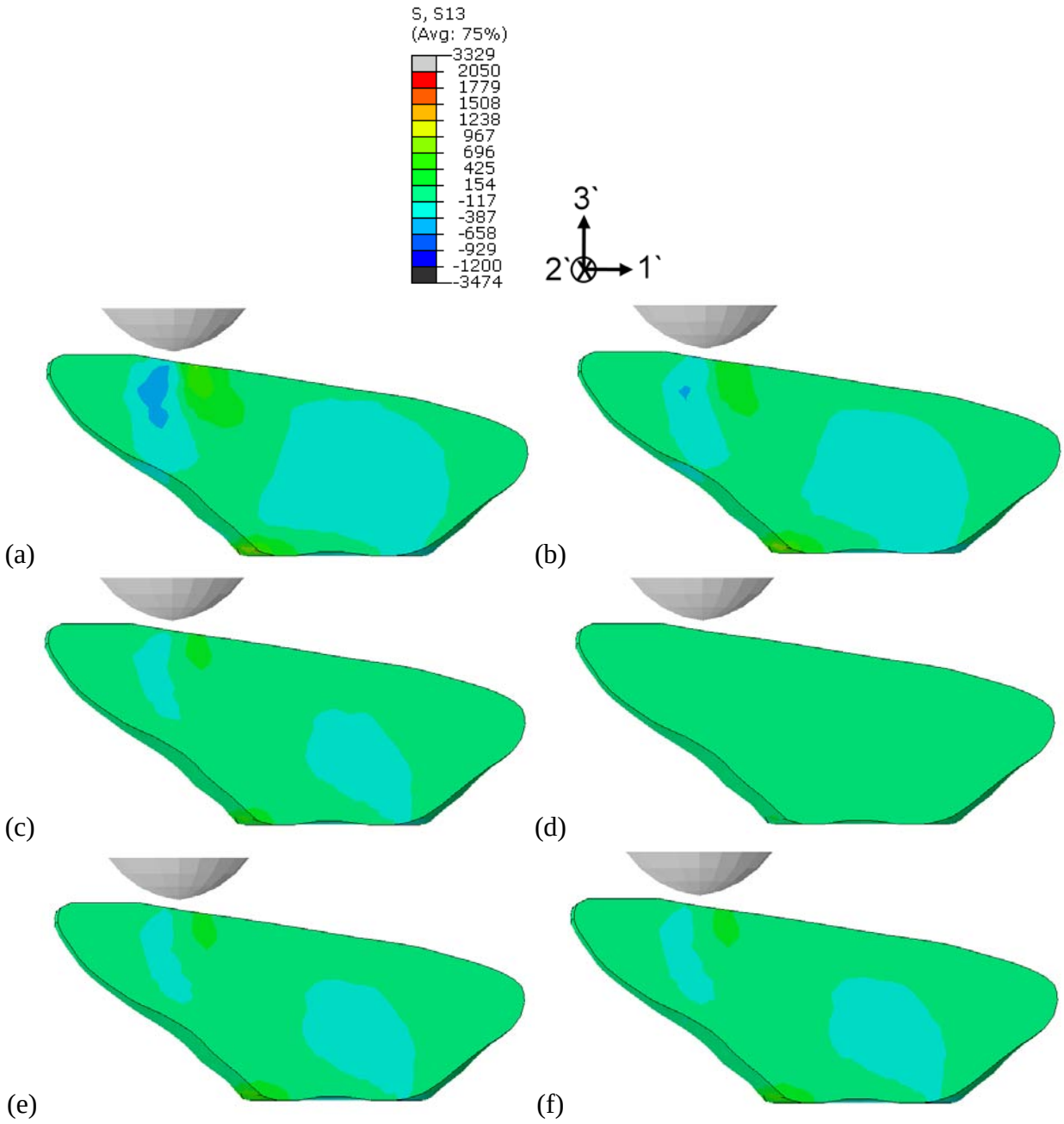


Figure 5-15: The shear stress, $\sigma_{1'3'}$, distribution of isotropic solid aboral spine under conical indenter loading to a depth 0.1mm with the shear stress distribution of several cases of anisotropic aboral spines, with material orientation specified, under conical indenter loading to a depth 0.1mm. Labels **a-f** refers to the same loading cases as Figure 5-13.

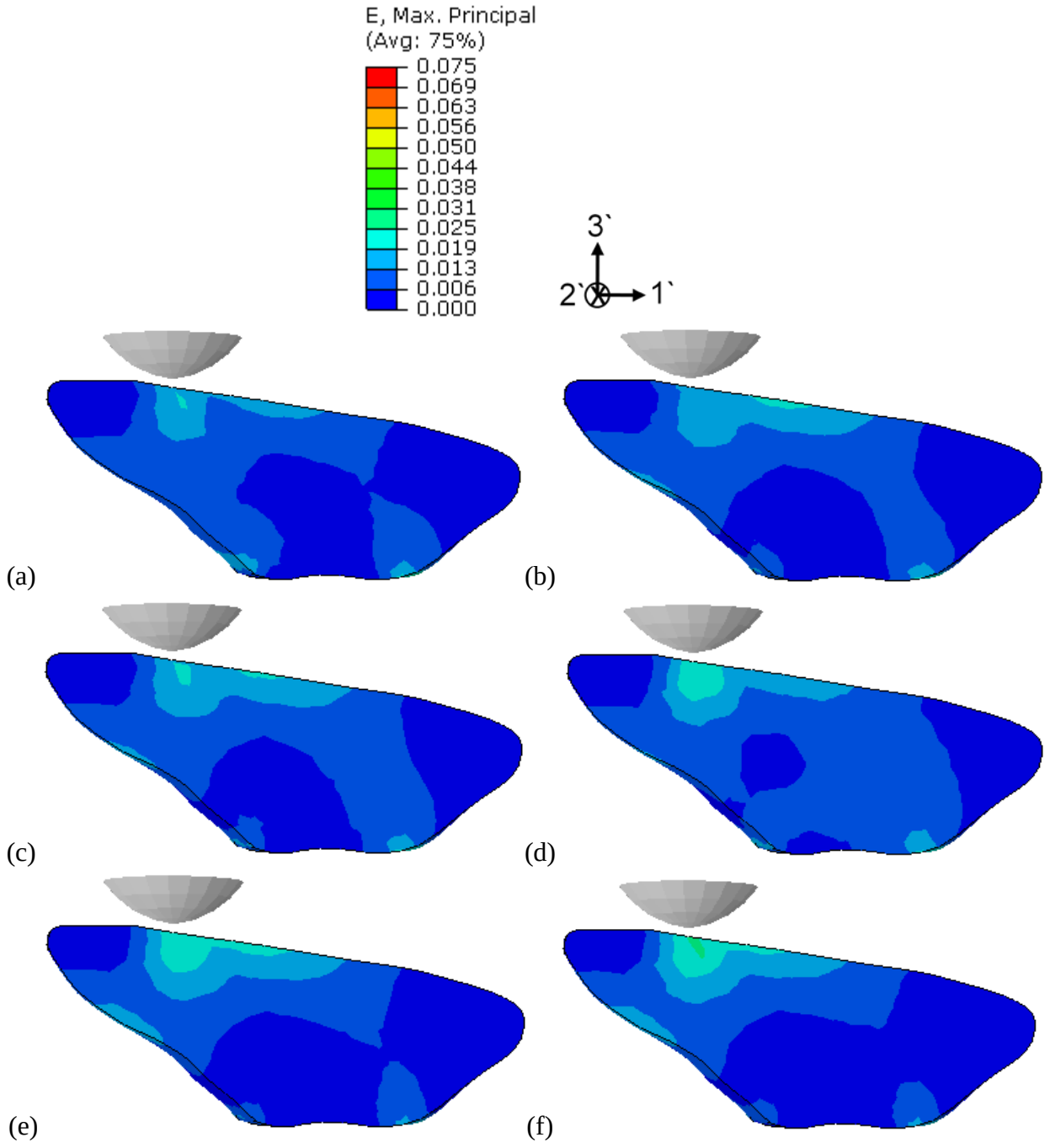


Figure 5-16: Comparing the maximum principal strain distribution of isotropic solid aboral spine under conical indenter loading to a depth 0.1mm with the maximum principal strain distribution of several cases of anisotropic aboral spines, with material orientation specified, under conical indenter loading to a depth 0.1mm. Labels **a-f** refers to the same loading cases as Figure 5-13.

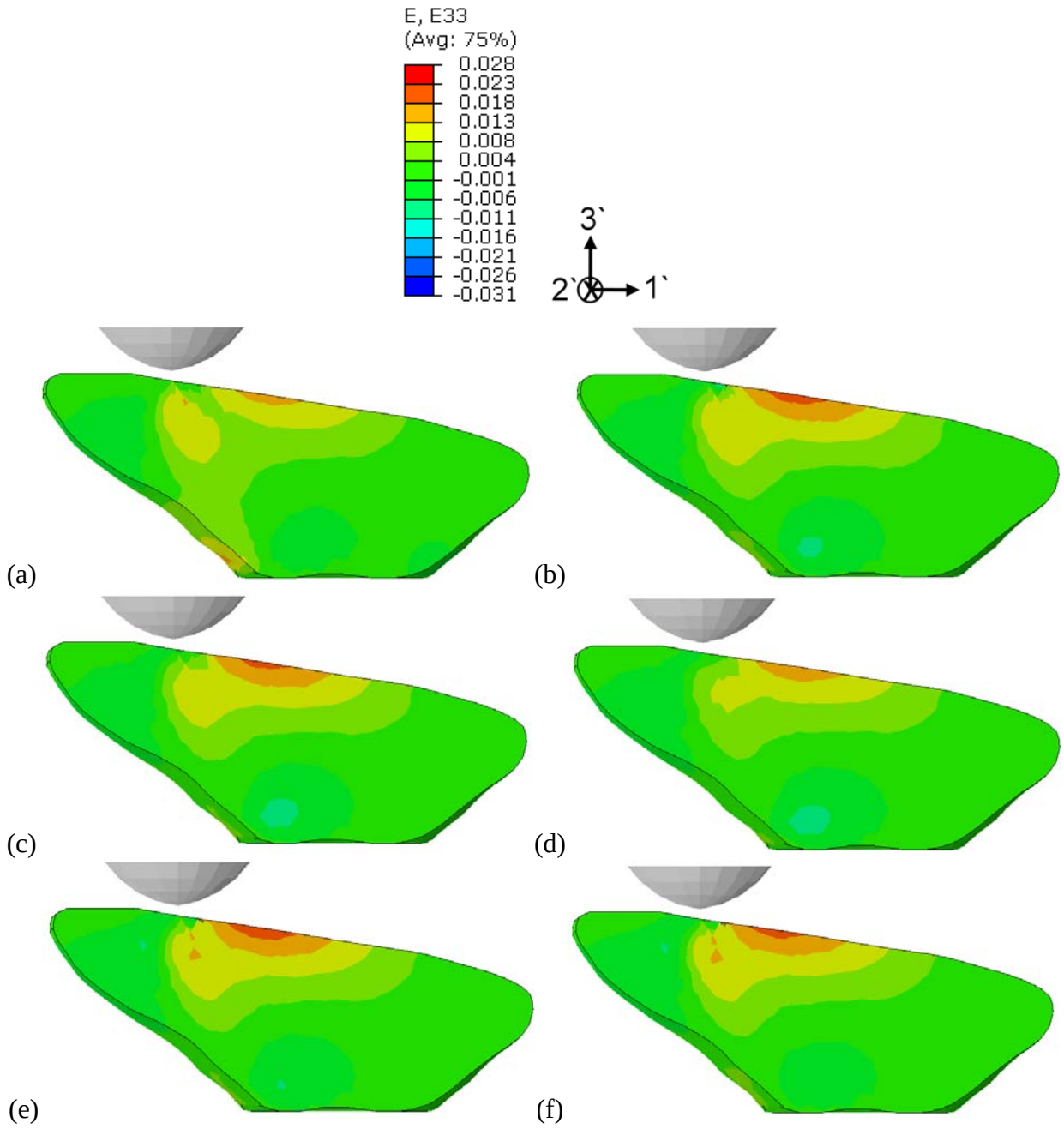


Figure 5-17: The axial strain, $\varepsilon_{3'3'}$, distribution of isotropic solid aboral spine under conical indenter loading to a depth 0.1mm with the axial strain distribution of several cases of anisotropic aboral spines, with material orientation specified, under conical indenter loading to a depth 0.1mm. Labels **a-f** refers to the same loading cases as Figure 5-13.

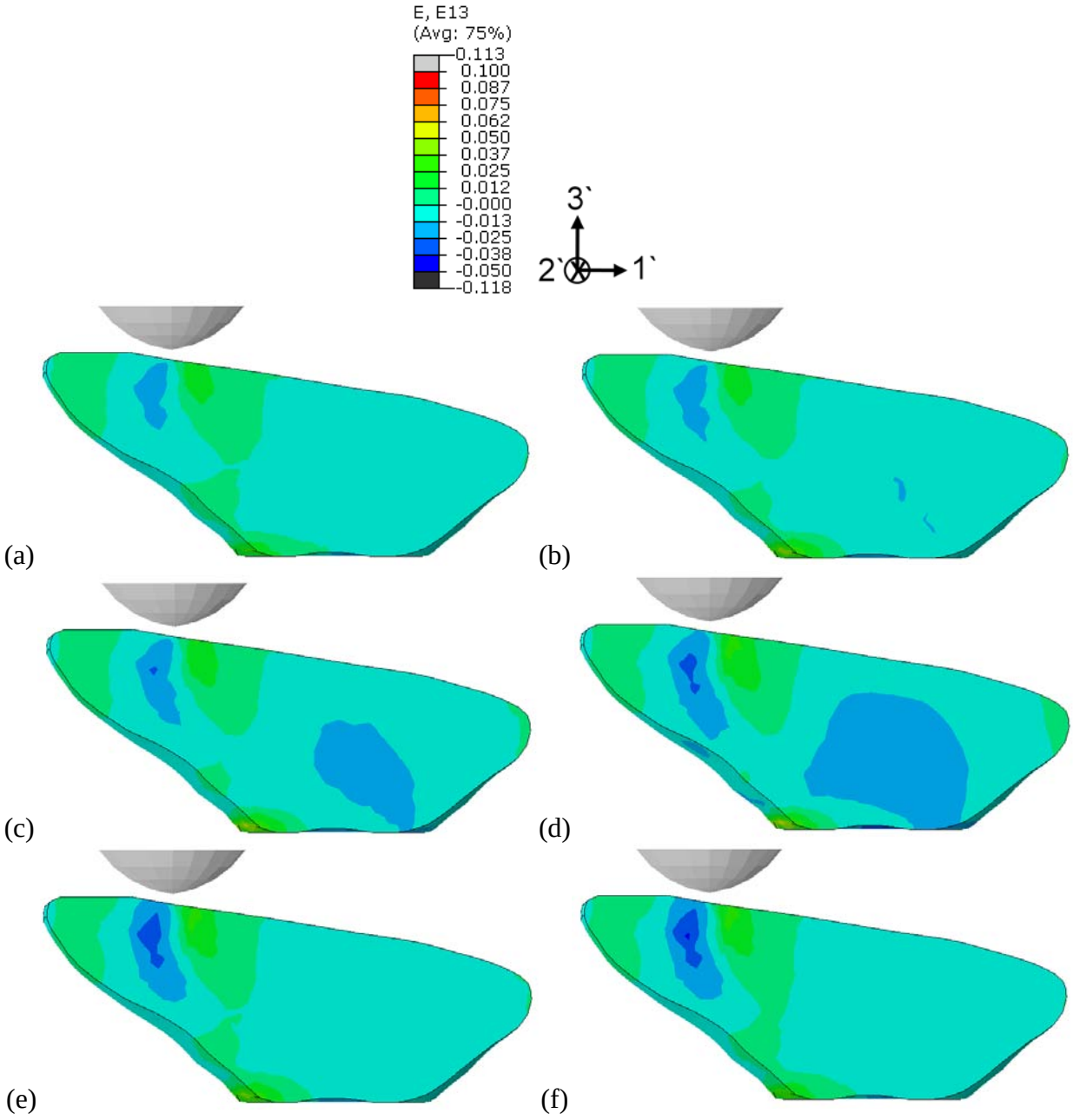


Figure 5-18: Comparing the shear strain, $\varepsilon_{1'3'}$, distribution of isotropic solid aboral spine under conical indenter loading to a depth 0.1mm with the shear strain distribution of several cases of anisotropic aboral spines, with material orientation specified, under conical indenter loading to a depth 0.1mm. Labels **a-f** refers to the same loading cases as Figure 5-13.

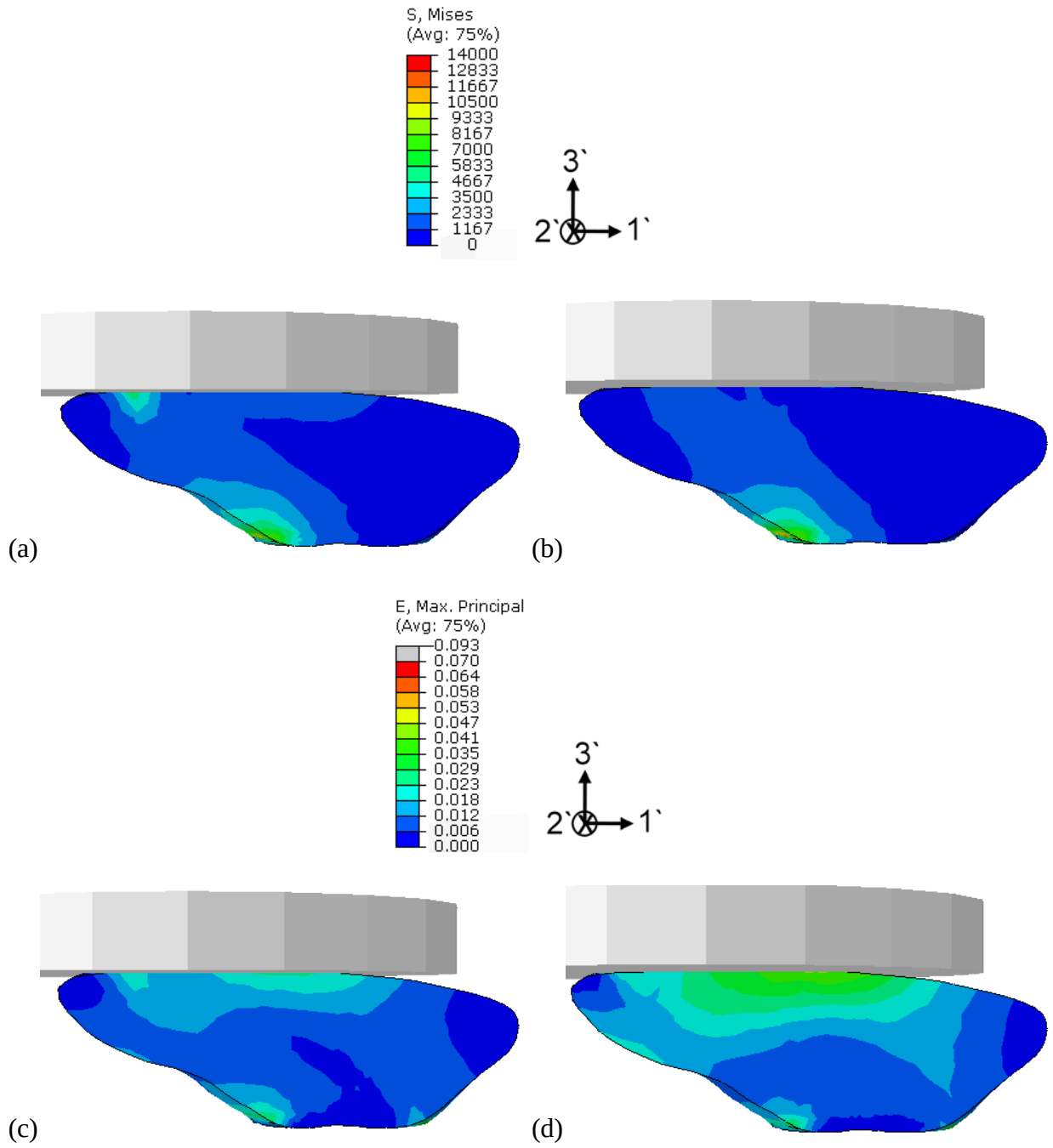


Figure 5-19: Mises and maximum principal strain contours of isotropic solid calcite case (**a** and **c**) compared to the anisotropic graded porosity case (**b** and **d**). Plots **a** and **c** are at an indentation depth of 0.13 mm while plots **b** and **d** are at a depth of 0.18 mm, with the same energy of 8.228e-6 J absorbed by the aboral spine.

# CHAPTER 6 Conclusions

With the quantitative analysis of high resolution scans to the multiscale mechanical modeling derived from three-dimensional imaging and reconstruction, this thorough approach to modeling from the microscale to the macroscale structure of a specimen provided a means of an accurate and fully parametric analysis of key features and details observed in nature. The microstructure of the sea urchin *Colobocentrotus atratus* was documented through SEM and microCT imaging and reconstruction. From imaging, the microstructure of the aboral spines of the *C. atratus* was fully characterized, in terms of gradients in volume porosity as well as three-dimensional microstructural features, variations, and material orientation. The porosity distribution was found to be a linear increase in porosity from the base to the top surface of the aboral spine while the orientation of the anisotropic porous microstructure was found to radiate outward from the socket joint.

With the microCT data of the aboral spines, it was possible to isolate the microstructural repeating unit with the porous network and extract four key parameters of its geometry. With the variation in the four parameters quantified along the axis of the aboral spine, a parametric finite element model of the repeating unit was created as a representative volume element with periodic boundary conditions. The geometric effects on the elastic stiffness of the four key features were investigated and the governing feature for each elastic stiffness property (E11, E22, G12, etc) was determined. The radii of transversal struts and the axial strut length was found to most significantly affect the elastic stiffness of the RVE, especially the shear moduli. The length of the transversal strut most strongly affected the porosity of the RVE and was also a significant factor in the moduli.

With geometry, microstructural network and material properties all incorporated into a single finite element model, the generalized elastic response of the aboral spine as a whole to two different loading conditions were explored. While the axial and shear stress with the anisotropic graded porosity material was similar to a spine with average uniform porosity, the effect of having a graded porosity with the highest porosity near the surface was found to increase the axial and shear strains near the indentation surface to be greater than the high porosity cases, while maintaining lower strains near the socket. This results in higher deformation at the surface of the plate because of the lower stiffness of the high porosity to reduce the effect near the socket where the density is greater and the material stiffer. This also lowered the strains near the socket joint by having most of the strains near the surface of the aboral spine. This gradient serves to absorb the load by deforming near the surface of the aboral spine, where the load is applied, thus minimizing the load transferred to the socket joint.

# CHAPTER 7 Future Work

From the data obtained by X-ray microcomputed tomography, further analysis of the entire scan can reveal the actual three-dimensional vector field of the microstructural orientation as well as the microstructural variations throughout the aboral spine. For this thesis, only the microstructure of the axial region of the aboral spines was analyzed from the microCT data. Further analysis can be done on the entire aboral spine, such that a spatial mapping of the microstructural features can be created. From the lower resolution scans, three-dimensional reconstruction of the exoskeleton can be done to create a mesh of entire portions of the urchin.

In addition to the two loading cases presented in the thesis, different variations of the loading conditions and microstructural orientation may reveal the advantages and tradeoffs of the porous organization. The indentations or other types of loading could also be done at varying points and depths on the aboral spine. In reality, the socket is not fixed, but rotates with the catch apparatus. Simulation of more realistic boundary conditions of the aboral spine may provide additional insight into the microstructural organization. Additionally, further expansion and analysis of the finite element model should incorporate the anisotropic properties of the solid, organic calcite which makes up the microstructure, as well as plasticity. Experimental methods to more specifically probe the solid properties of the organic calcite will improve the model's accuracy in predicting more realistic moduli of the parametric RVE. The same finite element analysis could also be performed on the underlying test plate on which the aboral spines articulate.

To verify the simulations and models, experimental analysis can be performed to test the actual aboral spine under several loading conditions, either attached to the urchin's body or

isolated. With the three-dimensional mesh of the actual microstructural network, a three-dimensional physical print of a region of the urchin's spine could be created and tested to observe the microstructure's deformation mechanisms and failure modes.

Because of the complete coverage of the aboral spines over the dome structure, while still allowing a degree of flexibility in the armor, the tiling of the aboral spines are also of interest. It can be looked at in several ways. A similarity to Voronoi tessellations may possibly indicate a minimum in the number of aboral spines in order to cover the dome while still maintaining coverage along the five main radial directions of the tiling characteristic of the echinoderms. Otherwise, the Voronoi pattern may just be a simple way to populate a surface with an aggregation of starting points. The flexibility of the aboral armor mainly stems from the tilting of the aboral spines about the ball-and-socket joints. During maneuvers, where the urchin must navigate a crevice, the aboral spines seem to tilt away or towards a radial line of direction (the five radial directions of echinoderms), these five lines may be where the underlying test can slightly give way.

# References

[1] Agassiz, A. (1908). Echini: The Genus Colobocentrotus. Cambridge, Memoirs of the Museum of Comparative Biology at Harvard College.

[2] Beniash, E., J. Aizenberg, et al. (1997). "Amorphous calcium carbonate transforms into calcite during sea urchin larval spicule growth." Proceedings of the Royal Society of London. Series B: Biological Sciences 264(1380): 461.

[3] Berman, A., L. Addadi, et al. (1990). "Intercalation of sea urchin proteins in calcite: study of a crystalline composite material." Science 250(4981): 664.

[4] Blake, D. F., D. R. Peacor, et al. (1984). "Ultrastructural and microanalytical results from echinoderm calcite: Implications for biomineralization and diagenesis of skeletal material." Micron and microscopica acta 15(2): 85-90.

[5] Clark, A. H. (1954). "Records of Indo-Pacific echinoderms."

[6] Currey, J. D. and D. Nichols (1967). "Absence of organic phase in echinoderm calcite."

[7] Danielsson, M., D. M. Parks, et al. (2002). "Three-dimensional micromechanical modeling of voided polymeric materials." Journal of the Mechanics and Physics of Solids 50(2): 351-379.

[8] Denny, M. and B. Gaylord (1996). "Why the urchin lost its spines: hydrodynamic forces and survivorship in three echinoids." Journal of experimental biology 199(3): 717.

[9] Donnay, G. and D. L. Pawson (1969). "X-ray diffraction studies of echinoderm plates." Science 166(3909): 1147.

[10] Ellers, O., A. S. Johnson, et al. (1998). "Structural strengthening of urchin skeletons by collagenous sutural ligaments." The Biological Bulletin 195(2): 136.

[11] Emlet, R. B. (1982). "Echinoderm calcite: a mechanical analysis from larval spicules." The Biological Bulletin 163(2): 264.

[12] Gaylord, B. (2000). "Biological implications of surf-zone flow complexity." Limnology and Oceanography 45(1): 174-188.

[13] James, D. B. (1982). "Ecology of intertidal echinoderms of the Indian seas." Journal of the Marine Biological Association of India 24(1&2): 124-129.

[14] Klein, L. R. and J. D. Currey (1970). "Echinoid skeleton: absence of a collagenous matrix." Science 169(3951): 1209.

[15] Kobayashi, S. and J. Taki (1969). "Calcification in sea urchins." Calcified Tissue International 4(1): 210-223.

[16] Ma, Y., S. R. Cohen, et al. (2008). "Sea Urchin Tooth Design: An “All Calcite” Polycrystalline Reinforced Fiber Composite for Grinding Rocks." Advanced Materials 20(8): 1555-1559.

[17] Magdans, U. and H. Gies (2004). "Single crystal structure analysis of sea urchin spine calcites: Systematic investigations of the Ca/Mg distribution as a function of habitat of the sea urchin and the sample location in the spine." European journal of mineralogy 16(2): 261.

[18] Mortensen, T. (1943). A monograph of the Echinoidea. Vol. III (3). Camarodonta. 2. Echinidae, Strongylocentrotidae, Parasaleniidae, Echinometridae, CA Reitzel, Copenhagen.

[19] O'Neill, P. L. (1981). "Polycrystalline echinoderm calcite and its fracture mechanics." Science 213(4508): 646.

[20] Oaki, Y., A. Kotachi, et al. (2006). "Bridged nanocrystals in biominerals and their biomimetics: classical yet modern crystal growth on the nanoscale." Advanced Functional Materials 16(12): 1633-1639.

[21] Paquette, J. and R. J. Reeder (1990). "Single-crystal X-ray structure refinements of two biogenic magnesian calcite crystals." American Mineralogist 75(9-10): 1151.

[22] Pérez-Huerta, A., M. Cusack, et al. (2007). "Material properties of brachiopod shell ultrastructure by nanoindentation." Journal of the Royal Society Interface 4(12): 33.

[23] Peters, B. H. (1985). "The innervation of spines in the sea-urchin Echinus esculentus L." Cell and tissue research 239(1): 219-228.

[24] Philippi, U. and W. Nachtigall (1996). "Functional morphology of regular echinoid tests (Echinodermata, Echinoida): a finite element study." Zoomorphology 116(1): 35-50.

[25] Politi, Y., T. Arad, et al. (2004). "Sea urchin spine calcite forms via a transient amorphous calcium carbonate phase." Science 306(5699): 1161.

[26] Presser, V., S. Schulthei, et al. (2009). "Sea Urchin Spines as a Model-System for Permeable, Light-Weight Ceramics with Graceful Failure Behavior. Part I. Mechanical Behavior of Sea Urchin Spines under Compression." Journal of Bionic Engineering 6(3): 203-213.

[27] Raup, D. M. (1959). "Crystallography of echinoid calcite." The Journal of Geology 67(6): 661-674.

[28] Santos, R. and P. Flammang (2008). "Estimation of the attachment strength of the shingle sea urchin, Colobocentrotus atratus, and comparison with three sympatric echinoids." Marine Biology 154(1): 37-49.

[29] Smith, A. B. and A. Palaeontological (1980). Stereom microstructure of the echinoid test, Palaeontological Association.

[30] Strathmann, R. R. (1981). "The role of spines in preventing structural damage to echinoid tests." Paleobiology 7(3): 400-406.

[31] Su, X., S. Kamat, et al. (2000). "The structure of sea urchin spines, large biogenic single crystals of calcite." Journal of materials science 35(22): 5545-5551.

[32] Takemae, N. and T. Motokawa (2005). "Mechanical properties of the isolated catch apparatus of the sea urchin spine joint: muscle fibers do not contribute to passive stiffness changes." The Biological Bulletin 208(1): 29.

[33] Telford, M. (1985). "Domes, arches and urchins: the skeletal architecture of echinoids (Echinodermata)." Zoomorphology 105(2): 114-124.

[34] Towe, K. M. (1967). "Echinoderm calcite: single crystal or polycrystalline aggregate." Science 157(3792): 1048.

[35] TsrpunsrY, S. J. and P. R. Busncr (1993). "Structure of magnesian calcite from sea urchins." American Mineralogist 78: 775-781.

[36] Weber, J., R. Greer, et al. (1969). "Unusual strength properties of echinoderm calcite related to structure1." Journal of ultrastructure research 26(5-6): 355-366.

[37] Weber, J. N. (1969). "The incorporation of magnesium into the skeletal calcites of echinoderms." American Journal of Science 267(5): 537.

[38] Weber, J. N., E. W. White, et al. (1971). "New porous biomaterials by replication of echinoderm skeletal microstructures."

[39] Wilkie, I. C. (2005). "Mutable collagenous tissue: overview and biotechnological perspective." Echinodermata: 221-250.

[40] Vincent, J. F. V. (2001). "Ceramics from invertebrate animals." Handbook of Elastic Properties of Solids, Liquids and Gases, edited by Levy, Bass and Stern 3.